

Electron Correlation Effects in Lateral Quantum Dots

Von der Fakultät für Mathematik und Physik
der Gottfried Wilhelm Leibniz Universität Hannover
zur Erlangung des Grades
Doktor der Naturwissenschaften

”Dr. rer. nat.”

genehmigte Dissertation

von

Dipl.-Phys. Daniel Tutuc
geboren am 20. April 1981 in Slatina, Rumänien

2011

Referent: Prof. Dr. Rolf J. Haug
Korreferent: Prof. Dr. Gertrud Zwicknagl

Tag der Promotion: 05.07.2011

Abstract

In this thesis we study correlation effects between spins confined in quantum dots and delocalized electrons in tunnel-coupled leads, as well as electron mediated indirect spin-spin exchange interactions in double quantum dots, via electronic transport spectroscopy.

The measurements are performed on single and double quantum dots coupled via an open conducting region. The samples are based on GaAs/AlGaAs heterostructures containing a shallow two-dimensional electron gas underneath the surface. The quantum dot structures have been patterned using optical lithography and local anodic oxidation with an atomic force microscope.

The quantum dots are characterized by Coulomb blockade measurements in the high tunnel coupling regime. In a few electron quantum dot the inelastic cotunneling thresholds corresponding to the first and second excited states are observed. Using non-linear transport spectroscopy, the ground state properties and the cotunneling energy gap are investigated in the presence of a perpendicular magnetic field.

The Kondo effect is explored in several single quantum dots. At zero-magnetic field the zero-bias anomaly is investigated by temperature and bias dependent measurements. Different methods for estimating the Kondo energy scale are used and compared, with the values from fitting the resonance width yielding the smallest errors. In parallel magnetic field the Zeeman splitting of the Kondo resonance is observed, allowing an estimation of the effective electron g^* factor. A flux-quantum modulation of the Kondo effect gives rise to the so-called

Kondo chessboard in perpendicular magnetic field. Temperature dependent measurements yield a linear decrease of the Kondo temperature with increasing magnetic field, in good agreement with the behavior of Landau level 0 energy states in the Fock-Darwin spectrum.

In a system consisting of two lateral quantum dots coupled via an open conducting reservoir, tuned in the Kondo regime, we study the tuning mechanisms of Ruderman-Kittel-Kasuya-Yosida (RKKY) exchange interaction. At zero magnetic field we observe the expected splitting of the Kondo resonance and estimate the non-local coupling strength as a function of the asymmetry between the two Kondo temperatures. Parallel magnetic field measurements reveal the anti-ferromagnetic character of the RKKY exchange interaction. At finite perpendicular magnetic fields a chiral coupling between the quantum dots is observed in the Kondo chessboard and we probe the presence of the exchange interaction by analyzing the Kondo temperature in magnetic field.

Keywords: quantum dots, Kondo effect, RKKY interaction

Kurzzusammenfassung

In dieser Arbeit werden Korrelationseffekte mittels elektronischer Transportspektroskopie zwischen in Quantenpunkten eingeschlossenen Spins und delokalisierten Elektronen in tunnelgekoppelten Zuleitungen untersucht. Des Weiteren werden Korrelationseffekte zwischen eingeschlossenen Spins in Doppelquantenpunkten durch Elektronen vermittelte, indirekte Spin-Spin-Austauschwechselwirkungen analysiert.

Die Messungen werden an Einzel- und Doppelquantenpunkten, die über eine offene, leitfähige Region gekoppelt sind, durchgeführt. Die Proben basieren auf GaAs/AlGaAs-Heterostrukturen, die ein flaches zweidimensionales Elektronengas unter der Oberfläche enthalten. Die Quantenpunktstrukturen wurden durch optische Lithographie und lokale anodische Oxidation mit einem Rasterkraftmikroskop hergestellt.

Die Quantenpunkte werden durch Coulomb-Blockade-Messungen im Regime hoher Tunnelkopplung charakterisiert. In einem mit wenigen Elektronen besetzten Quantenpunkt werden die Schwellen für inelastisches Kottunneln bezüglich der ersten und zweiten angeregten Zustände beobachtet. Mit Hilfe nichtlinearer Transportspektroskopie werden die Grundzustandseigenschaften und die Kottunnel-Energie-lücke im magnetischen Feld untersucht.

In verschiedenen Einzelquantenpunkten wird der Kondo-Effekt erforscht. Die Zero-Bias-Anomalie wird ohne angelegtes Magnetfeld abhängig von Temperatur und Vorspannung untersucht. Verschiedene Methoden zur Abschätzung der Größenordnung der Kondo-Energie werden angewandt und verglichen, wobei mit den Werten aus dem An-

fitten der Resonanzbreite die kleinsten Fehler erreicht werden. Im parallelen magnetischen Feld wird die Zeeman-Aufspaltung der Kondo-Resonanz beobachtet, was eine Abschätzung des effektiven Landé g^* -Faktors erlaubt. Eine Flussquanten-Modulation des Kondo-Effekts im senkrechten magnetischen Feld führt zu dem so genannten *Kondo-Schachbrett*. Temperaturabhängige Messungen ergeben in guter Übereinstimmung mit dem Verhalten von Landau-Niveau Null Energiezuständen des Fock-Darwin Spektrums ein lineares Abnehmen der Kondo-Temperatur mit zunehmendem Magnetfeld.

In einem System mit zwei lateralen Quantenpunkten, die über ein offenes, leitfähiges Reservoir gekoppelt und ins Kondo-Regime geregelt sind, werden die Regelungsmechanismen der Ruderman-Kittel-Kasuya-Yosida (RKKY) Austauschwechselwirkung studiert. Ohne magnetisches Feld wird das erwartete Aufspalten der Kondo-Resonanz beobachtet und die nichtlokale Koppelstärke als Funktion der Asymmetrie zwischen den Kondo-Temperaturen abgeschätzt. Messungen im parallelen Magnetfeld lassen den anti-ferromagnetischen Charakter der RKKY Austauschwechselwirkung erkennen. Bei endlichen senkrechten Magnetfeldern wird eine chirale Kopplung zwischen den Quantenpunkten im Kondo-Schachbrett beobachtet, und durch Analysieren der Kondo-Temperatur im Magnetfeld wird die Präsenz der Austauschwechselwirkung überprüft.

Schlagworte: Quantenpunkte, Kondo-Effekt, RKKY Wechselwirkung

Contents

1. Introduction	21
2. Theoretical background	25
2.1. The electron gas in low-dimensions	26
2.1.1. The 2D electron gas in magnetic field	30
2.1.2. Electron tunneling through a barrier	36
2.2. Quantum dots	38
2.2.1. Electrostatic capacitance model	38
2.2.2. Constant interaction model	41
2.2.3. Quantum dots in magnetic field	41
2.2.4. Quantum dots in transport	47
2.3. Kondo effect	55
2.3.1. Introduction	55
2.3.2. Kondo effect in quantum dots	58
2.3.3. Transport characteristics in the Kondo regime	61
3. Experimental techniques	69
3.1. Sample preparation	70
3.1.1. Heterostructures	70
3.1.2. Optical lithography	74
3.1.3. Scanning probe nanolithography	77
3.1.4. Samples	82
3.2. Measurement setup	84
3.2.1. The dilution refrigerator	84

Contents

3.2.2. Electrical setup	86
4. Inelastic Cotunneling Spectroscopy	89
4.1. Inelastic cotunneling at zero-magnetic field	90
4.2. Inelastic cotunneling in perpendicular magnetic field	93
4.3. Summary	99
5. Kondo effect in Single Quantum Dots	101
5.1. Kondo effect in a single quantum dot	102
5.1.1. Kondo effect at zero magnetic field	103
5.1.2. Kondo effect in parallel magnetic field	108
5.1.3. Kondo effect in perpendicular magnetic field	111
5.2. Summary	117
6. Kondo effect in RKKY-coupled Double Quantum Dots	119
6.1. Introduction to the Rudermann-Kittel-Kasuya-Yosida interaction	120
6.1.1. The exchange interaction in quantum dots .	123
6.2. The RKKY interaction at zero magnetic field	126
6.2.1. Asymmetric Kondo coupling	127
6.2.2. Symmetric Kondo coupling	133
6.3. Exchange interaction in parallel magnetic field	140
6.4. The RKKY interaction in perpendicular magnetic field	145
6.4.1. Temperature dependence	148
6.4.2. Bias dependence	155
6.5. Summary	157
7. Summary and conclusions	159
A. Additional data on sample C021227B	163
B. Additional data on sample D080330A	167

C. Additional data on sample D040330A	169
D. Signal and grounding electrical setup	173
Bibliography	177

List of Figures

2.1. Crystal sphere in momentum space	27
2.2. Density of states in 3, 2, 1 and 0 dimensions	29
2.3. 2D density of states in magnetic field	31
2.4. Schematic of the edge state formation	33
2.5. Edge channel transport in a Hall bar	34
2.6. Schematic representation of a tunnel barrier	36
2.7. Schematic representation of a quantum dot	39
2.8. The Fock-Darwin spectrum of a quantum dot	42
2.9. Quantum dot Landau levels	44
2.10. The quantum dot chemical potential at intermediate magnetic fields	45
2.11. Schematic of the quantum dot charge density in high magnetic fields	46
2.12. Linear measurements through a quantum dot	48
2.13. Charge stability diagram of a quantum dot as a func- tion of gate voltages	50
2.14. Charge stability diagram as function of bias and gate voltage	52
2.15. Excitation spectroscopy schematic	53
2.16. Schematic temperature dependence of the resistance of metals	56
2.17. Anderson model for a single level quantum dot	58
2.18. Density of states in the Kondo regime	59

List of Figures

2.19. Linear and non-linear Kondo conductance	62
2.20. Temperature dependence of the Kondo conductance	63
2.21. Temperature dependence as function of detuning in the Kondo valley	65
2.22. Kondo conductance in an external magnetic field . .	66
2.23. Temperature dependence of the zero-bias Kondo con- ductance in an external magnetic field	67
3.1. Conductance band minimum across the GaAs/AlGaAs interface	71
3.2. Layer sequence for wafer C021227B	72
3.3. Layer sequence for wafer D040330A	72
3.4. Layer sequence for wafer D080220A	73
3.5. Optical lithography processing steps - schematic diagram	75
3.6. The sample during optical lithography	76
3.7. Scanning Probe Nanolithography	78
3.8. The AFM setup for Local Anodic Oxidation	80
3.9. C021227B structure	82
3.10. D080220A structure	82
3.11. D040330A structure	82
3.12. Kelvinox 300 dilution refrigerator	85
3.13. Setup for samples C021227B and D08022A	86
3.14. Setup for sample D040330A	88
4.1. Onset of cotunneling peaks in a Coulomb diamond measurement	90
4.2. Schematic of a Coulomb diamond with two cotunnel- ing peaks visible	92
4.3. Measurement of the cotunneling peaks as a function of perpendicular magnetic field	94
4.4. Cotunneling energy gap as a function of magnetic field	96

4.5. Non-linear measurements of the cotunneling peaks at different magnetic fields	97
4.6. Measurement of the charge stability diagram in magnetic field	98
4.7. Fock-Darwin spectrum with the 13th and 14th electron peaks marked	99
5.1. Non-linear measurement of the Kondo resonance . . .	102
5.2. Lorenz fit of the Kondo resonance versus bias	104
5.3. Temperature dependence of the Kondo resonance . . .	105
5.4. Tuning the Kondo temperature using an in-plane gate	107
5.5. Conductance plot showing the Kondo ZBA in parallel magnetic field	108
5.6. Kondo ZBA splitting in parallel magnetic field	109
5.7. Kondo resonance with a Lorenz fit	110
5.8. The Kondo chessboard in perpendicular magnetic field	111
5.9. Temperature dependence in the Kondo chessboard . . .	114
5.10. Temperature dependence in the Kondo chessboard w/o background	115
5.11. Kondo temperature and the shape parameter in the Kondo chessboard	116
6.1. Two spins coupled via RKKY interaction	121
6.2. Schematic of two quantum dots coupled via RKKY interaction	123
6.3. AFM image of sample D040330A	126
6.4. Asymmetric Kondo resonances in QD1 and QD2	128
6.5. Transport in the presence of exchange interaction . . .	129
6.6. QD2 Kondo resonance in the presence of the RKKY interaction	131

List of Figures

6.7. Coupling dependence of the Kondo resonances in the presence of exchange interaction	132
6.8. Symmetric Kondo resonances in QD1 and QD2 . .	134
6.9. QD1 Kondo resonance as a function of QD2 plunger gate	136
6.10. QD3 Kondo resonance as a function of QD1 plunger gate	137
6.11. Kondo resonance width and temperature dependence	138
6.12. Magnetic field dependence of the split Kondo resonance	140
6.13. Kondo resonances in parallel magnetic field	142
6.14. Kondo zero-bias conductance in parallel magnetic field	143
6.15. Chiral coupling in the Kondo chessboard	146
6.16. Temperature dependence of QD1 in perpendicular magnetic field	149
6.17. Temperature dependence of QD2 in perpendicular magnetic field	151
6.18. Temperature dependence of the total conductance in perpendicular magnetic field	153
6.19. Bias dependence in perpendicular magnetic field . . .	156
A.1. Additional measurements on sample C021227B . . .	165
A.2. Additional measurements on sample C021227B . . .	166
B.1. Background subtraction for sample D080220A in the Kondo chessboard	168
C.1. Additional measurements on sample D040330A . . .	170
C.2. Additional measurements on sample D040330A . . .	171
C.3. Background subtraction for sample D040330A in the Kondo chessboard	172
D.1. Grounding diagram of the measurement setup	174

D.2. AC-DC adder and divider 175

Symbols and Abbreviations

Symbols

\vec{A}	Vector potential
A	Area
a_{GaAs}	Lattice constant of e.g. GaAs
Al	Aluminium
As	Arsenide
\vec{B}	Magnetic field
B	Absolute value of the Magnetic field
C	Capacitance
c	Specific heat
χ	Susceptibility
$D(E)$	Density of states
ΔX	Variation of parameter X
e	Elementary charge ($1.60217733 \cdot 10^{-19}$ C)
E	Energy
E_F	Fermi energy
E_C	Charging energy
E_N	Addition energy
E_Z	Zeeman energy
ϵ_0	Dielectric constant
ϵ	Relative dielectric constant
ϵ_n	Eigen values
ϵ_i	Single particle energy

$\Delta\varepsilon$	Single particle energy spacing
Δ_{Cot}	Cotunneling onset energy gap
F	Fermi function $F(E)$
ϕ	The magnetic flux quantum ($2.067 \cdot 10^{-15}$ Wb)
g^*	Effective Lande factor
G	Linear conductance
Ga	Gallium
Γ	Rate, i.e. Tunnel rate
h	Plank's constant
\hbar	$h/2\pi$
H	Hamiltonian operator
He	Helium - known isotopes ^4He or ^3He
I	Current
J_K	Kondo exchange coupling with the leads
J_{RKKY}	RKKY exchange coupling
$\vec{k}_x, \vec{k}_y, \vec{k}_z$	Wavevector in x, y, z -direction
k	Absolute value of the wavevector
k_B	Boltzmann constant ($8.617 \cdot 10^{-5} eVK^{-1}$)
k_F	Fermi wavevector
L	Length
l_B	Magnetic length
m_e	Free electron mass ($9,1095 \cdot 10^{-31}$ kg)
m^*	Electron effective mass
μ	Chemical potential, with Index e.g. μ_N
μ_B	Bohr magneton ($\frac{e\hbar}{2m_e} = 5.788 \cdot 10^{-5} eVT^{-1}$)
μ_e	Electron mobility
$\mu_{4.2K}$	Electron mobility at 4.2 K
n	Quantum number
N	A total number
n_e	Electron density

$n_{4.2K}$	Electron density at 4.2 K
n_L	Degeneracy degree of a Landau level
ν	Filling factor
$\langle N \rangle$	Average charge
p_x, p_y, p_z	Momentum in x, y, z -direction
π	Circle constant $\pi = 3,14159\dots$
R	Resistance
R_H	Hall-resistance
R_K	von Klitzing-constant ($\approx 25812, 807 \Omega$)
R_W	Wilson ratio
r	Radius
r_n	Classic cyclotron radius
Si	Silicon
S	Spin quantum number
σ	Differential conductance
T	Temperature
t	Time
Θ	Heaviside function
v_F	Fermi velocity
V	Voltage
V_{G1}, V_{G2}, \dots	Gate voltage on Gate G1, G2,...
V_{SD}	Voltage drop between Source and Drain
ω_c	Cyclotron frequency
w	Wilson's number
ω_x, ω_y	Angular frequency x, y -direction

Abbreviations

0D	zero-Dimensional
1D	one-Dimensional
2D	two-Dimensional
2DEG	2 Dimensional Electron Gas
2IK	Two Impurity Kondo model
Fig.	Figure
AC	Alternative current / -voltage
AFM	Atomic Force Microscope
DAC	Digital-to-Analog-Converter
DC	Direct current / -voltage
DMM	Digital MultiMeter
<i>et al.</i>	and Co-authors (et alii)
<i>e.g.</i>	For example (exempli gratia)
Gate	Control electrode
G1, G2, G3, ...	Gate Number 1,2,3...
<i>i.e.</i>	that is / in other words (id est)
FWHM	Full Width at Half Maximum
HWHM	Half Width at Half Maximum
LAO	Local Anodic Oxidation
QD	Quantum Dot
QHE	Quantum-Hall-Effect
QPC	Quantum Point Contact
MBE	Molecular Beam Epitaxy
RKKY	Rudermann-Kittel- Kasuya-Yosida
SMU	Source Measure Unit
ZBA	Zero-Bias Anomaly

1

Chapter 1.

Introduction

Quantum mechanics has fascinated mankind since its introduction in the beginning of the 20th century, allowing a fundamental understanding of the behavior of matter at a sub-atomic scale. For the past 20 years, man-made structures containing a small number of electrons, called *quantum dots*, have proven to be a fertile ground for the study of basic quantum mechanical effects like discrete energy spectrum, charge quantization, electron-electron interactions or interference phenomena [1–4]. Their high versatility and tunability have also made quantum dots suitable for technological applications: the electron spin confined in a quantum dot being proposed for the realization of a quantum bit [5], single electron pumping in quantum dots will most probably define the current standard in the near future [6], and quantum dots as single photon sources could be used for applications in quantum information technology [7].

One of the major breakthroughs in quantum dot physics was the realization of an artificial Kondo system [8–10]. Kondo effect is a electron correlation interaction in a many-particle system which arises from

1. Introduction

the screening of a localized magnetic impurity by delocalized electrons in the surrounding Fermi sea, at very low temperatures [11]. A quantum dot containing an odd number of electrons has necessarily a non-zero total spin, which makes it behave as a magnetic impurity [12]. The electrons in the leads will therefore screen the spin of the dot, forming a new singlet ground state, the so-called *Kondo state*. Although the electrons on the dot are confined by the surrounding potential, the quantum mechanical uncertainty allows the localized spin to leave the dot, and the other spin in the singlet to take its place, thus flipping the effective spin of the dot and increasing the zero-bias conductance. This leads to the formation of a peak in the density of states at the impurity site due to the successive spin-flips at temperatures below T_K , the so-called *Kondo temperature*, which is essentially the energy scale describing the binding energy of the spin singlet formed between the localized, unpaired electron and delocalized electrons in the leads.

Magnetic impurities interact also with one another via carrier mediated spin-spin interactions, like the Ruderman-Kittel-Kasuya-Yosida (RKKY) interaction [13–15]. However, whereas the Kondo screening continuously flips the spin of the impurity, the RKKY exchange interaction tends to freeze it, competing with the Kondo effect. The competition between the two interactions gives rise to non-trivial behaviors [16] and in the simplest case, with two impurities in a Fermi sea, is described by the *two-impurity Kondo* (2IK) model [17, 18]. Because the RKKY interaction is a long-range carrier mediated process, the entanglement of two spins beyond the nearest neighbor restraint is possible, with promising applications in quantum information technology. Only recently such a system has been experimentally realized [19], as two quantum dots coupled via an open conducting region. By adjusting various experimental ”knobs” the electron number contained in the two quantum dots can be tuned individually, which determines the spin, and in turn the presence of Kondo effect. In such a system con-

taining two localized spins, the competition between the Kondo effect and spin-spin exchange interactions leads to a second order quantum phase transition [20], or a crossover if there is a finite tunnel coupling to the quantum dots [21, 22]. However, even if the observation of the RKKY-Kondo competition in artificial systems has been previously claimed [19, 23] a conclusive understanding is missing [22, 24–26], and more experimental investigations are required.

The purpose of this thesis is the realization and investigation of a two-impurity-Kondo system consisting of two quantum dots placed in close proximity of one another, in order to explore the competition between Kondo effect and the RKKY interaction predicted by the two-impurity Anderson model. Interaction effects between localized spins embedded in lateral quantum dots and delocalized spins of electron in the Fermi sea, which give rise to the Kondo effect in a solid state system, are also explored. The thesis is organized as follows:

Chapter 2 starts with a brief description of low-dimensional electron systems and their properties in magnetic field. The second part of the chapter introduces quantum dots and the theoretical models used in their description, with emphasis on their properties in magnetic field. The last part of the chapter focuses on the Kondo effect in quantum dots. The electronic transport characteristics of a quantum dot in the Kondo regime are then discussed in the frame of the Anderson impurity model.

Chapter 3 presents the fabrication and preparation procedures used for producing the quantum dot structures, as well as a detailed description of the electronic and cryogenic measurement setup.

Inelastic cotunneling phenomena in a few electron quantum dot are presented and discussed in Chapter 4. A finite bias gives access to the inelastic cotunneling thresholds corresponding to the first excited states and we study the role played by orbital effects induced by a magnetic field applied perpendicular to the quantum dot.

1. Introduction

Chapter 5 is entirely devoted to the experimental investigations of Kondo effect in multi-electron quantum dots. We start with the occurrence of the so-called *zero-bias anomaly* (ZBA) at zero magnetic field and the estimation of the Kondo energy scale from the resonance width and temperature dependence. Finally, we probe the splitting of the Kondo resonance in a parallel magnetic field and describe the Kondo modulation in perpendicular magnetic field, giving rise to the striking Kondo chessboard pattern.

In Chapter 6 we explore the interplay between the Kondo effect and the RKKY non-local exchange interaction in a sample with two quantum dots connected via an open reservoir, as a realization of the two-impurity Kondo system. The RKKY interaction strength is studied as a function of the Kondo energy scale of each quantum dot. Non-linear measurements in parallel magnetic field allow probing the anti-ferromagnetic nature of the exchange interaction. In perpendicular magnetic field we investigate the role of the edge states and chiral transport in the coupling between the spins of the quantum dots.

Finally, in Chapter 7 a summary of the results and conclusions is given.



Chapter 2.

Theoretical background

In this chapter the basic physics of low-dimensional systems is reviewed. We begin by deriving the expressions for the electron density of states in 0, 1 and 2 dimensions. Then the properties of a 2-dimensional electron gas in perpendicular magnetic field are discussed, along with the origin of quantum hall effect (QHE). The second part contains the main properties of quantum dots, described in the frame of the so-called Constant Interaction model. We look at the energy quantization in magnetic field, and describe the charge density picture of a quantum dot, as well as electronic transport properties. In the third part of the chapter we discuss the physics of Kondo effect, in the frame of the Anderson impurity model applied to quantum dots.

2. Theoretical background

2.1. The electron gas in low-dimensions

In this section we consider the properties of the two-dimensional electron gas (2DEG). This is only a part of a large number of 2-dimensional systems that have been intensively studied in recent years. By two-dimensional electron system we mean that the electron is free to move in two directions, but their motion is confined in the third [27].

The motion of electrons in a solid state system can be described by a standing-wave oscillations. That means that in a bulk material the electron wavelength λ can be related to the length of the system by $L = n_x \lambda$, where n_x is a positive integer representing the number of modes in the x direction. The wavelength is related to the momentum through the *de Broglie* formula $\lambda = h/p_x$, where h is Planck's constant and p_x is the electron momentum. In a three-dimensional system for a unity increase in n , this gives [28]:

$$L^3 p_x p_y p_z = h^3 \quad (2.1)$$

where $p_x p_y p_z$ is the volume in momentum space. Each incremental change in n generates another set (n_x, n_y, n_z) , corresponding to an allowed energy state. Thus the volume of an energy state in momentum space is h^3 . If we consider an interval $(p, p + dp)$, in momentum space, it corresponds to two concentric spheres with a volume $4\pi \vec{p}^2 d\vec{p}$ (Fig. 2.1), and the number of energy states in this volume is therefore $2(4\pi \vec{p}^2 d\vec{p})/h^3$, where the prefactor 2 accounts for the spin degeneracy. Taking into account that electron energy is given by $E = p^2/2m^*$, the number of energy states per unit volume can be re-written as:

$$D_{3D}(E) = \frac{(2m^*)^{3/2}}{2\pi^2 \hbar^3} \sqrt{E} \quad (2.2)$$

where $D(E)$ is the so-called *density of states* - the allowed energy states per unit volume (Fig. 2.2 (a)). In Eq.2.2 we use $\hbar = h/2\pi$.

2.1. The electron gas in low-dimensions

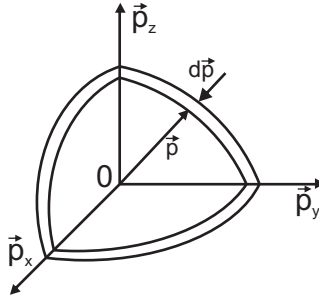


Figure 2.1.:
Crystal sphere in momentum space

The 3D electron energy can be written as:

$$E = \frac{\vec{p}^2}{2m^*} = \frac{\hbar^2 \vec{k}^2}{2m^*} = \frac{\hbar^2 \vec{k}_x^2}{2m_x^*} + \frac{\hbar^2 \vec{k}_y^2}{2m_y^*} + \frac{\hbar^2 \vec{k}_z^2}{2m_z^*} \quad (2.3)$$

where \vec{k} is the electron wavevector with the x,y and z components given by $k_i = 2\pi/\lambda_i = p_i/\hbar$, and λ_i is the wavelength, with $i = x, y, z$. The electron effective mass m^* takes into account the crystal energy bands and usually has a form of a tensor. In GaAs the effective mass can be considered with good approximation as having the same value in all directions. At $T \simeq 1.5$ K the effective mass in GaAs is $m_{GaAs}^* \simeq 0.067m_0$, where m_0 is the free electron mass.

Applying a confinement potential in the z-direction of a crystal leads to the quantization of the energy in the same direction [27]:

$$E(\vec{k}_x, \vec{k}_y, n_z) = \frac{\hbar^2 \vec{k}_x^2}{2m_x^*} + \frac{\hbar^2 \vec{k}_y^2}{2m_y^*} + E_z(n_z), \quad (2.4)$$

with $n = 1, 2, 3, \dots$ the number of occupied energy states. Thus the electron can move freely only in the x and y directions, creating a two

2. Theoretical background

dimensional electron system. The experimental realization of a two-dimensional electron system is later described in Chapter 3.1.

The 2D density of states for one occupied subband is given by $D_{2D}(E) = m^*/(\pi\hbar^2)$, while for several occupied subband is the sum of the Heaviside function Θ (see also Fig. 2.2(b)):

$$D_{2D}(E) = \frac{m^*}{\pi\hbar^2} \sum_{n_z} \Theta(E - E_z(n_z)) \quad (2.5)$$

With another confinement applied, i.e. in y-direction, the electron motion is restricted to just one direction, on the x-axis, with the energy quantized in z and y-directions:

$$E(\vec{k}_x, n_y, n_z) = \frac{\hbar^2 \vec{k}_x^2}{2m_x^*} + E_y(n_y) + E_z(n_z) \quad (2.6)$$

with a 1D density of states given by (Fig. 2.2(c)):

$$D_{1D}(E) = \frac{\sqrt{2m^*}}{\pi\hbar} \frac{1}{\sqrt{E}} \quad (2.7)$$

The main difference with respect to 2D, where the subband energy is constant, is that the 1D yields a $1/\sqrt{E}$ dependence. An example of a 1D system is the so-called *quantum wire* (QW) [29] or *quantum point contact* (QPC) [30, 31].

If the electron motion is further confined also in the x-direction, the system becomes zero-dimensional, with the particle energy quantized in all directions:

$$E(n_x, n_y, n_z) = E_x(n_x) + E_y(n_y) + E_z(n_z) \quad (2.8)$$

Considering that the external confinement is parabolic, the energy can

2.1. The electron gas in low-dimensions

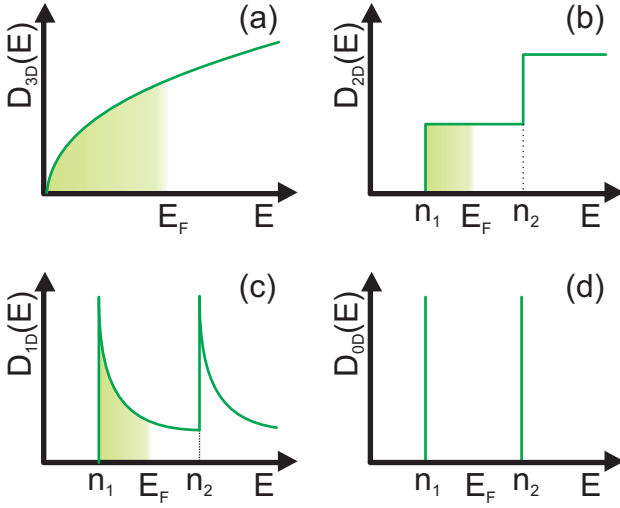


Figure 2.2.:

Density of states in 3, 2, 1 and 0 dimensions. In the figure the first two quantized states n_1 and n_2 are represented, with respect to the position of the Fermi energy E_F .

be written as

$$E(n_x, n_y, n_z) = \hbar\omega_x \left(n_x + \frac{1}{2} \right) + \hbar\omega_y \left(n_y + \frac{1}{2} \right) + \hbar\omega_z \left(n_z + \frac{1}{2} \right) \quad (2.9)$$

with $\hbar\omega_i$ the harmonic oscillator energy and $n_i=0,1,2,\dots$ the number of occupied energy states in each direction, with $i = x, y, z$. The density of states of such a system is given by a sum over Dirac δ -functions (Fig. 2.2(d)):

$$D_{0D}(E) = 2 \sum_{n_x, n_y, n_z} \delta(E - E(n_x, n_y, n_z)), \quad (2.10)$$

2. Theoretical background

where the factor 2 takes into account the level spin degeneracy. Because the density of states exhibits quantization in all directions, such a 0D system is usually called a *Quantum Dot* or an *artificial atom* [1–3], and we will further discuss the properties of such a system in Sec. 2.2.

2.1.1. The 2D electron gas in magnetic field

Landau levels

If we consider the motion of a free electron in a magnetic field B applied along the z-direction, electrons are forced into circular orbits. Their motion is described by the following Hamiltonian:

$$H = \frac{1}{2m^*}(p - eA)^2, \quad (2.11)$$

where \vec{A} is the vector potential and is related to the magnetic field by $\vec{B} = \nabla \times \vec{A}$. The eigenvalues obtained by solving Schrödinger's equation have the form [32]:

$$\varepsilon_n = \hbar\omega_c \left(n + \frac{1}{2} \right), \quad n = 1, 2, 3, \dots \quad (2.12)$$

where n is level quantum number and ω_c the cyclotron frequency, given by:

$$\omega_c = \frac{eB}{m^*} \quad (2.13)$$

These energy levels are called *Landau levels* and are equally spaced by $\hbar\omega_c$ increments (see Fig. 2.3 (a)). At temperatures lower than the inter-level spacing ($k_B T \ll \hbar\omega_c$) we find single occupied or partially occupied Landau levels. If we take the electron spin into account, the eigenenergies expression becomes:

$$\varepsilon_n = \hbar\omega_c \left(n + \frac{1}{2} \right) + g^* \mu_B B S_z, \quad (2.14)$$

2.1. The electron gas in low-dimensions

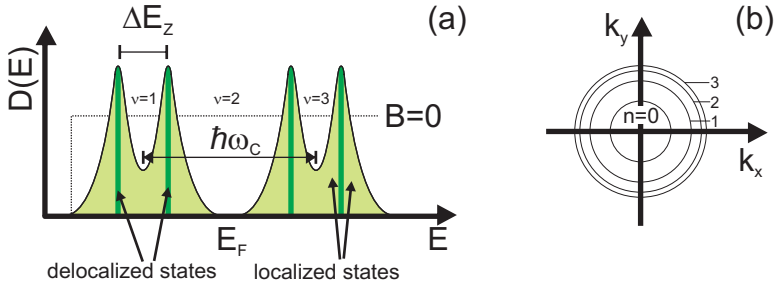


Figure 2.3.:

(a) 2D density of states in magnetic field for the first subband. Dotted line marks the step function DOS for $B=0$. (b) Landau level representation in k -space

where g^* is the electron Landé factor, μ_B the Bohr magneton and $S_z = \pm 1/2$ the spin quantum number. The last term account for the two spin orientations. For a fixed n , the degeneracy of each Landau level is given by:

$$n_L = \frac{eB}{h} \quad (2.15)$$

In this regime a useful quantity is the magnetic length:

$$l_B = \sqrt{\frac{\hbar}{eB}} \quad (2.16)$$

which provides information on the extent of the electron wave function and enters the expression of the cyclotron radius $r_n = \sqrt{(2n+1)}l_B$ that describes the radius of the electron circular path in magnetic field.

Localized and delocalized states

A change in magnetic field will change the energy splitting $\hbar\omega_c$ of the Landau levels, so with increasing magnetic field the energy states are

2. Theoretical background

moving higher in energy. As they cross over the Fermi energy, the Landau levels are emptied, and the electrons pushed to the next lower level. So the degeneracy degree of a Landau level is increased by magnetic field. This can be described by defining the filling factor of a Landau level:

$$\nu = \frac{n_e}{n_L} = \frac{hn_e}{eB}, \quad (2.17)$$

where n_e is the electron density in the system. The filling factor represents the degree of Landau level filling, that is the number of fully or partially filled energy states.

The Landau level are energetically broadened by scattering on impurities, phonons or crystal defects present in real samples [33]. As a consequence, near the delocalized states at the center of the peaks, are found localized energy states (see Fig. 2.3 (a) for a schematic representation). Because they are not extended over the whole sample, the localized states do not carry any current [34].

Quantum Hall effect and the formation of edge states

The Landau level quantization in magnetic field is the origin of Quantum Hall Effect in two-dimensional systems [34, 35]. This effect has become one of the most important investigation tools for semiconductors. In 1980 Klaus von Klitzing measured the voltage drop perpendicular to a current, or the Hall resistance, of a 2DEG embedded in a silicon metal-oxide-semiconductor field-effect transistor. Instead of the classical linear behavior, the resistance exhibited plateaus whenever a Landau level was crossing the Fermi energy, with values given by the following relation:

$$R_H = \frac{h}{e^2} \frac{1}{\nu}, \quad \nu = 0, 1, 2, 3, \dots \quad (2.18)$$

2.1. The electron gas in low-dimensions

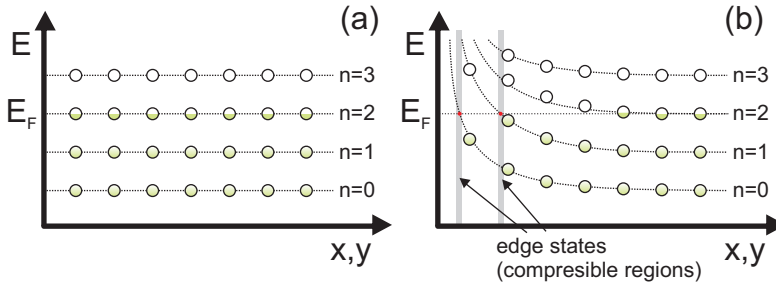


Figure 2.4.:

Schematic of the edge state formation - (a) Landau level energies for an infinite (a) and finite (b) 2DEG.

A simultaneous measurement of the longitudinal resistance - given by the voltage drop parallel to the current - yields a series of peaks each time the Hall resistance jumps from one plateau to the next.

As the magnetic field is increased (or carrier density decreased) the localized states in the Landau levels are gradually emptied without any change in the occupation of the delocalized states. In this case the Hall resistance is in a plateau, while the longitudinal resistance vanishes. Only when the Fermi energy lies at the core of the delocalized states there is a change in the longitudinal resistance, and the Hall resistance makes a transition to the next plateau.

While the longitudinal resistance oscillations are understood due to the formation of Landau levels [36], the Hall plateau quantization in units of e^2/h is easier to explain in terms of edge states. The finite dimensions of a sample result in an increased confinement near the edges due to screening, and the Landau level energies are enhanced, crossing eventually the Fermi level (see Fig. 2.4 (b)). Normally a Landau level that is below the Fermi energy, being fully filled with electrons, is not conducting, however because the energy bending at the bound-

2. Theoretical background

aries of the sample that leads to the edge state formation, these too can contribute to the conductance of the sample. The energy states at the point where the Landau level crosses the Fermi level are forming one-dimensional channels along the edges of the sample, the so-called *edge channels*. So to each Landau level below the Fermi level it corresponds an edge channel.

By taking into consideration electron exchange interactions, it was shown that at the edges the potential increase of the Landau level is not smooth, but step-wise, and every Landau level has a region of flat potential at the Fermi energy [37]. These regions have a variable charge density, usually termed as *compressible* stripes, and are the ones responsible for the carrier transport. The regions between the edge channels never contain states at the Fermi level - thus called *incompressible* - and do not contribute to transport.

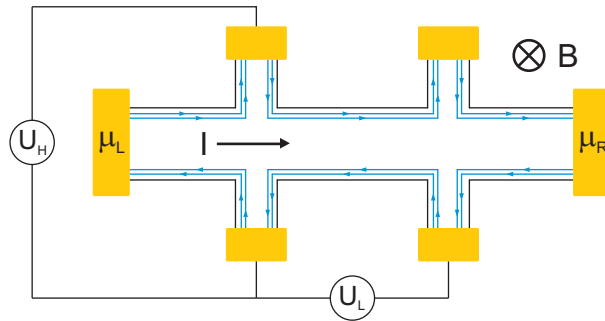


Figure 2.5.:

Edge channel transport in a Hall bar. Black line marks the edge of the sample, in yellow are the contacts, while the edge states are depicted in blue. Creating a potential difference between the left (μ_L) and right (μ_R) contacts will drive a current I through the sample. The Hall voltage drop U_H is measured between two opposite contacts, while the longitudinal voltage drop U_L is measured between nearby contacts.

2.1. The electron gas in low-dimensions

In Figure 2.5 we consider the transport through the first two edge states in a sample with a Hall bar geometry. If the temperature is well below the Landau level separation, i.e. $k_B T \ll \hbar\omega_c$, the edge states are electrically isolated from each other. Furthermore, as the electron scattering at the edge boundary is elastic, transport through the edge states is quasi-ballistic, even in samples containing impurities [38]. That means that the electrons within one edge state are at the same potential, so electrons flowing "right" along the upper edge (see. Fig. 2.5) have the potential of the left contact μ_L , while the electrons flowing "left" along the lower edge, have the potential of the right contact μ_R . The electro-chemical potential difference is given by the applied voltage times the electron charge, or

$$\mu_L - \mu_R = eV \quad (2.19)$$

The total current can be calculated from the difference between the current flowing into the left and right contacts. Only the Landau levels that cross the Fermi level as edge states have a contribution to the current (e.g. Landau levels with indexes 0,1 and 2 in Fig. 2.4). This can be written as [32]:

$$I = \sum_{n=1}^{n_c} \int_{\mu_R}^{\mu_L} e D_{1D}^n(E) v_n(E) dE, \quad (2.20)$$

where n_c is the maximum Landau level index crossing the Fermi level, $D_{1D}(E)$ is the 1D density of states (see Eq. 2.7) and v_n is the electron velocity in the n -th channel. The contribution of the n -th channel to the current is:

$$I = \frac{e}{h} (\mu_L - \mu_R) = \frac{e^2}{h} V \quad (2.21)$$

2. Theoretical background

That means that each channel contributes with a quantum of e^2/h to the total conductance, or h/e^2 to the Hall resistance, which are exactly the increments between the Hall plateaus.

2.1.2. Electron tunneling through a barrier

A potential barrier, represented schematically in Fig. 2.6 (a), can be described by a potential height Φ_0 and a finite width w . In a classical picture if a particle encounters a potential barrier with an energy higher than its kinetic energy, then the particle is reflected. However, in quantum mechanics a particle with a wavelength much smaller than the barrier width $\lambda \ll w$ has finite transmission coefficient, given by [39]:

$$T(E) \cong \exp\left(-4\sqrt{2m^*(\Phi_0 - E)}\frac{w}{\hbar}\right) \quad (2.22)$$

At zero bias voltage V_{SD} the electro-chemical potentials of the Source and Drain, μ_S and μ_D , are at the same level, while at finite bias $V_{SD} = (\mu_S - \mu_D)/e$, because there are empty states on the other side of the barrier, a current is generated through the barrier, by so-called

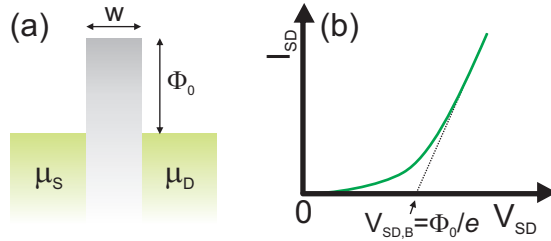


Figure 2.6.:

(a) Schematic representation of a tunnel barrier with a width w and a height Φ_0 . (b) I-V characteristic of an ideal tunnel barrier.

2.1. The electron gas in low-dimensions

first order tunneling events. When the bias exceeds the barrier height $V_{SD,B} \geq \Phi_0/e$ the kinetic energy of the electrons is high enough to breakthrough, so the barrier is reduced to an Ohmic resistor, and the current increases linearly. An example of an I-V characteristic of a tunnel barrier is depicted in Fig. 2.6 (b), where the tunneling region is marked up to $V_{SD,B}$, and the resistive region for higher bias. Estimating the barrier height can be straightforwardly extracted by extending the high bias linear region to $I_{SD} = 0$ (dashed line in Fig. 2.6 (b)), with the obtained bias value $V_{SD,B}$ proportional to the barrier potential height: $\Phi_0 = \alpha e V_{SD,B}$.

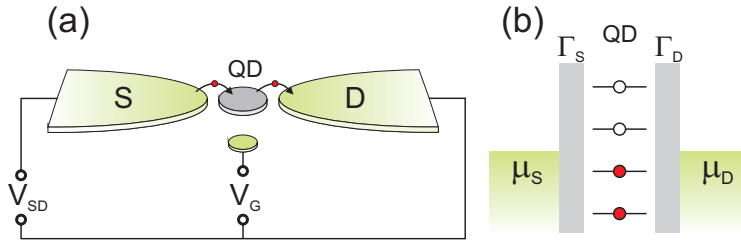
2. Theoretical background

2.2. Quantum dots

Quantum dots (QDs) are small electron islands confined within an insulating environment (Fig. 2.7 (a)). If the dimensions of the potential well created by the surrounding confinement are of the order of the Fermi wavelength, such an electron island is a quasi-0D system, with well defined energy levels (Fig. 2.7 (b)). As we have seen in section 2.1 the density of states of a zero-dimensional system has a discrete energy spectrum. For this reason quantum dots are also called *artificial atoms* (see Ref. [1–3] and references within). The advantage over real atoms, is that quantum dots can be electrically probed through transport spectroscopy. Contact leads can be attached, acting as electron reservoirs and are connected to the QD via tunnel barriers. A third lead called a *Gate* can be added, coupled capacitively to the QD. An applied voltage on the gate will shift the position of the energy levels on the dot with respect to the electro-chemical potential of the leads. In a static situation (e.g. Fig. 2.7 (b)) all the levels on the QD with an energy lower than the chemical potential in the leads ($\mu_i \leq \mu_S, \mu_D$) will be filled with electrons, while all levels above the electro-chemical potential of the leads will be empty.

2.2.1. Electrostatic capacitance model

One of the basic characteristics that can be observed in transport is the quantization of charge on the quantum dot. This means that in a situation when the coupling to the leads is negligible, there is an integer number of electrons N on the dot, with a total charge $Q = Ne$. When tunneling takes place the charge on the island changes by one. The quantum dot can be viewed as a capacitor, with a total capacitance C , and whenever a charge is added the Coulomb energy changes. The amount of energy required to place an extra electron on the dot is the


Figure 2.7.:

Schematic representation of a quantum dot. (a) A small electron island defined between a Source and a Drain lead in a two-dimensional electron gas. A third lead acting as plunger gate is capacitively coupled to the island. (b) Discrete energy spectrum of a quantum dot with tunnel couplings Γ_S to the Source, respectively Γ_D to the Drain.

so-called *charging energy* - $E_C = e^2/C$. This energy scale becomes relevant only when it's larger with respect to the temperature, $E_C \gg k_B T$. Another relevant parameter is the dot isolation from the leads, which can be parameterized by the tunnel resistance R_t or by the time scale on which a tunneling event on and off the dot takes place $\Delta t = R_t C$. In order to observe single charging events in transport from the Heisenberg relation $\Delta E \Delta t = E_C R_t C > h$ we must draw the conclusion that the tunnel resistance must be larger than the resistance quantum, or $R_t \gg h/e^2$ [2].

The shape of a dot created by patterning a two-dimensional electron gas (a process discussed in the next chapter) can be approximated with a disc of radius r , therefore the associated capacitance is that of a single plate capacitor with respect to infinity, $C = 8\epsilon_r \epsilon_0 r$, with ϵ_r the relative dielectric constant and ϵ_0 the dielectric constant of vacuum. If we consider the quantum dot and the surrounding leads as a network of capacitors, and the potential of the gates and leads are known, the

2. Theoretical background

dot potential V_0 can be computed using:

$$V_0 = \frac{Q}{C} + \sum_{i=1}^n \frac{C_i}{C} V_i, \quad (2.23)$$

where C_i and V_i is the capacitance, respectively the potential, of lead i . The total capacitance C is the capacitance of the electron island to its nearby surrounding environment, and it is given by the sum over the lead capacitances C_i : $C = \sum_i C_i$. The capacitance C_i actually defines the dependence of the QD charge as a function of the voltage V_i applied to lead i . From Eq. 2.23 we can obtain the energy of the quantum dot for a given number of electrons N :

$$E_N = \int_0^{Ne} V_0(q) dq = Ne \underbrace{\sum_{i=1}^n \frac{C_i}{C} V_i}_{1st} + \underbrace{\frac{(Ne)^2}{2C}}_{2nd} \quad (2.24)$$

In Eq. 2.24 the first term represents the potential of the electron island with N electrons, while the second term is the energy necessary to load the dot with N electrons. From this relation the chemical potential of the dot can be derived:

$$\mu_N = \frac{\partial E_N}{\partial N} = e \sum_{i=1}^n \frac{C_i}{C} V_i + N \frac{e^2}{C} \quad (2.25)$$

The difference between the chemical potential of two successive energy states gives the charging energy necessary to load one electron on the dot:

$$E_C = \mu_{(N+1)} - \mu_N = \frac{e^2}{C} \quad (2.26)$$

The electrostatic capacitance model can describe qualitatively the Coulomb blockade phenomena that is observed in transport through quantum dots, however it completely neglects their internal structure.

2.2.2. Constant interaction model

A more accurate description of transport through quantum dots is given by the so-called *constant interaction* model, which in addition takes into account the internal electronic level structure. This model is very useful in analyzing the addition spectra of a quantum dot.

A finite area A can be associated to a quantum dot defined in a 2DEG. From the two-dimensional density of states $D_{2D}(E) = m^*/\pi\hbar^2$ one can estimate the single level energy spacing $\Delta\varepsilon_i$ [40]:

$$\Delta\varepsilon_i = \varepsilon_{i+1} - \varepsilon_i = \frac{\pi\hbar^2}{m^*A} \quad (2.27)$$

In the simplest case, assuming a harmonic confinement potential, the spacing between energy levels is considered constant, that is $\Delta\varepsilon_i = \Delta\varepsilon$, however for other confinement potentials this may not be a valid assumption anymore.

Thus, considering a system containing N electrons, the addition energy is given by the energy E_N from Eq. 2.24 given by the capacitance model, plus the sum over the absolute energy values of the occupied single-particle states ε_i :

$$E_N^I = E_N + \sum_i \varepsilon_i \quad (2.28)$$

Even though the constant interaction model can describe relatively well the addition spectra of quantum dots, only the Coulomb interactions are taken into account, while other electron-electron interactions, screening, correlation and exchange effects, which can play an important role in many-electron systems, are neglected.

2.2.3. Quantum dots in magnetic field

Obtaining the spectrum of a quantum dot in perpendicular magnetic field requires solving the Schrödinger equation. Considering a circu-

2. Theoretical background

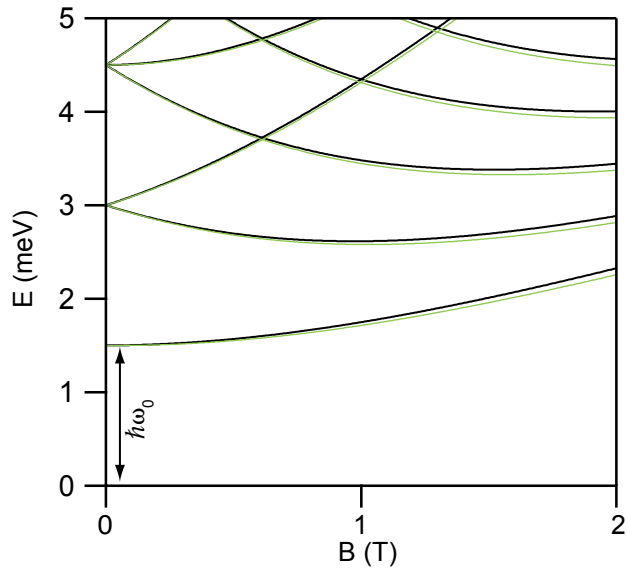


Figure 2.8.:

The Fock-Darwin spectrum of a quantum dot calculated for $\hbar\omega = 1.5$ meV. Black lines represent spin up, while green lines are for spin down. The red square marks the intermediate magnetic field region discussed in Sec. 2.2.3.

lar shaped quantum dot of radius r , in a parabolic confinement, the potential of the dot can be written as:

$$V(r) = \frac{1}{2}m^*\omega_0^2r^2 \quad (2.29)$$

The corresponding Schrödinger equation, initially solved by V. Fock and C.G. Darwin [41, 42], yields:

$$\varepsilon_{n,l}(B) = (2n + |l| + 1) \sqrt{\hbar^2 \omega_0^2 + \frac{1}{4} \hbar^2 \omega_c^2} - \frac{1}{2} l \hbar \omega_c \pm \frac{1}{2} g^* \mu_B B \quad (2.30)$$

where $n = 0, 1, 2, \dots$ is the radial quantum number, $l = 0, \pm 1, \pm 2, \dots$ is the angular quantum number and g^* is the effective electron Landé factor, describing the Zeeman splitting of energy levels in magnetic field. For zero magnetic field the spectrum is formed by equally spaced levels located at $(j + 1)\hbar\omega_0$, where $j = 2n + |l|$ is the shell number. The shells hold an orbital degeneracy and each level within is spin degenerate. The perpendicular magnetic field lifts the orbital and spin degeneracy and the energy levels dependence on magnetic field is given by the so-called *Fock-Darwin spectrum*, represented in Fig. 2.8.

Intermediate magnetic fields

Figure 2.10 (a) describes a region of intermediate magnetic field, where the electrostatic confinement energy becomes less important, and the energy levels are brought together to form Landau levels (Fig. 2.9). In this case the energy states that belong to Landau level 0 (LL0) have a downward slope with increasing magnetic field, while states from Landau level 1 show an increasing trend with magnetic field, resulting in multiple energy level crossings, in a diamond-like pattern. The Landau level spacing is given by $\hbar\omega_c$. The depopulation of higher Landau levels with increasing magnetic field is reflected in the lower energy of Landau level 0, and at a sufficiently high magnetic field all the electrons are found in the lowest Landau level.

If we consider the situation when the electron number on the dot is constant, the chemical potential of the dot, as well as its energy, develops a so-called *zig-zag* pattern in magnetic field. This is in fact due to

2. Theoretical background

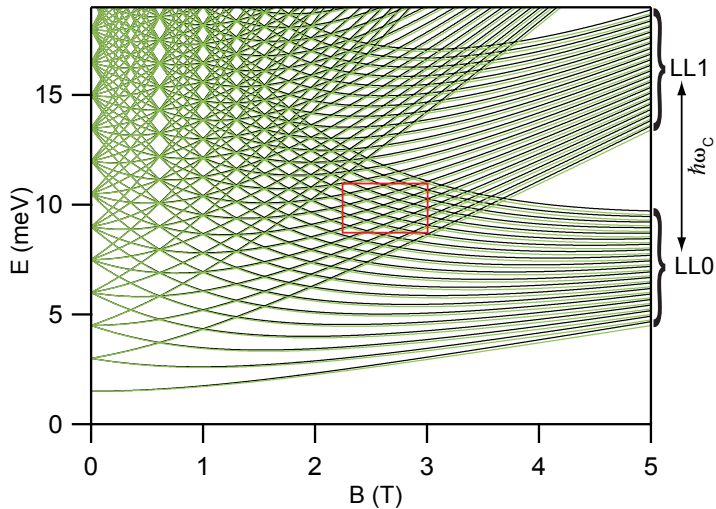


Figure 2.9.:

Quantum dot Landau levels - The Fock-Darwin spectrum of a quantum dot for a confinement energy of $\hbar\omega_0 = 1.5$ meV. At high magnetic fields the energy states are brought together to form Landau levels. Black lines represent spin up, while green lines are for spin down.

the orbital occupation rules, the electrons always being located on the lowest energy unfilled orbital. Such a situation is marked by thick lines for the N th (black) and $(N-1)$ th electrons in Fig. 2.10 (a) ¹. Initially the N th electron is in a LL0 orbital (negative slope). At the first crossing the N th electron moves to a LL1 orbital with positive slope, while the $(N-1)$ th takes its place in the LL0 orbital. At the next crossing the N th electron changes again to a lower energy LL0 orbital, while the $(N+1)$ th is forced into LL1. The oscillation period in the magnetic

¹In this case the spin splitting is neglected for simplicity reasons, so the levels are spin degenerate

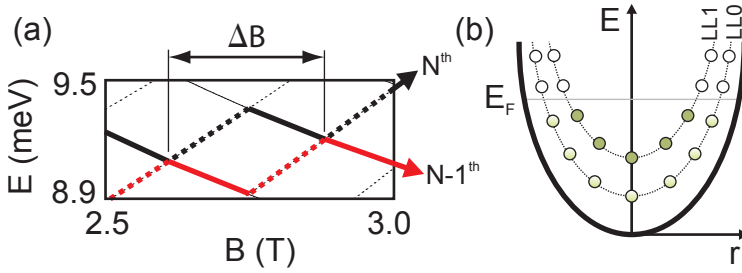


Figure 2.10.:

The quantum dot chemical potential at intermediate magnetic fields. (a) Area of the spin-degenerate Fock-Darwin spectrum with the zig-zag pattern exhibited by the chemical potential of the dot for the N^{th} and $(N-1)^{\text{th}}$ electrons (thick lines). Full lines mark the LL0 orbitals, while dashed lines mark orbitals that belong to LL1. (b) Schematic representation of the first two Landau levels in a parabolic confinement potential.

field direction can be approximated by $\Delta B \approx (\omega_0/\omega_c)^2 B$, while the energy spacing is given by $\Delta E \approx \hbar(\omega_0^2/\omega_c)$ [40], independent of the corresponding quantum numbers.

In Fig. 2.10 (b) the first two Landau levels in the parabolic confinement of a quantum dot are depicted. As we can see, Landau level 1 is formed near the center of the dot, which makes its energy states to couple weakly to the leads, equivalent to a thicker tunnel barrier, due to the longer distance the electron has to tunnel. On the other hand, energy states that belong to LL0 will couple stronger to the leads. Even though here we consider only a parabolic confinement, this model can also be extended to other types of potentials, like the hard-wall potential that characterizes quantum dots produced by Local Anodic Oxidation [43].

2. Theoretical background

Charge density in a quantum dot

The constant interaction model can be further extended to include the electron-electron Coulomb interaction, that influences the addition spectrum in magnetic field. McEuen *et al.* [44] have performed self-consistent calculations starting from the following expression of the QD's total energy:

$$E_{tot}(N) = \sum_n \sum_s \left[\left(n + \frac{1}{2} \right) \hbar \omega_c + g^* \mu_B B S_z \right] \int d^2r n_{ns}(r) + \int d^2r n(r) \left[V_{ext}(r) + \frac{1}{2} \int d^2r' n(r') V_{ee}(r, r') \right] \quad (2.31)$$

where n_{ns} is the electron density in the n -th Landau level, S_z the spin polarization, $n(r)$ the total electron density and $V_{ext}(r)$ the unscreened confining potential. The electron-electron interaction is included in $V_{ee}(r, r')$. The first two terms describe the single electron energy, while the last term describes the electron interaction.

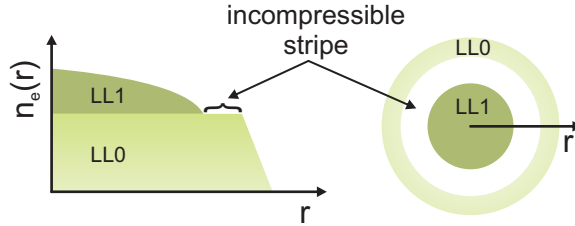


Figure 2.11.:

Schematic of the quantum dot charge density in high magnetic fields. (Left) Self-consistent calculation of the charge density for the first two Landau levels. (Right) Quantum dot charge density viewed from above.

The result of self-consistent calculations for the charge density distribution inside the quantum dots is qualitatively depicted in Fig. 2.11. At high magnetic fields electrons are initially placed in Landau level 0 at the center of the dot, where there is a potential minimum (Fig. 2.10 (b)), while further electrons are placed near the edge due to the Coulomb repulsion. After LL0 becomes completely occupied electrons are added to Landau level 1, after overcoming the $\hbar\omega_c$ energy that separates the Landau levels. Thus, in the central region where the confining potential is completely screened, LL0 yields a constant charge density, while at the edge the charge density drops rapidly. The partial occupation of LL1 results in a gradual drop in charge density from center towards the edges. In between two Landau levels there are regions with a constant charge density, so-called *incompressible strips*, that do not contain energy states at the Fermi energy, and thus do not contribute to transport, i.e. have an insulating behavior. On the other hand the regions where the charge density varies (e.g. LL1 or the edge area of LL0) are called *compressible*, and have a metallic behavior. These compressible and incompressible region model is similar to the formation of edge states in the quantum Hall regime, discussed in 2.1.1.

2.2.4. Quantum dots in transport

In the following we review the basic methods for probing the internal structure of a quantum dot by transport spectroscopy. This method requires a current flow through the dot, so first of all the tunnel barriers have to be transparent enough to allow it. As we have discussed in the previous sections, the chemical potential of a zero-dimensional system has only discrete values. We also consider that the quantum dot is coupled to leads that have a two-dimensional density of states.

In the situation represented schematically in Fig. 2.7 (b), the states with an energy lower than the chemical potential of the leads are filled,

2. Theoretical background

while the ones with higher energy are left unfilled. However in this case the transport is Coulomb blocked. In order to measure a current flow through one of the discrete energy states, the dot can be investigated in either the linear (ohmic) response, or in the non-linear response regime.

Linear measurements

A system is considered in the linear response regime if the measured current is proportional to the applied bias. This behavior is valid only when the bias applied to the Source or the Drain contacts is very small compared to the thermal energy, in other words $\mu_S - \mu_D \ll k_B T$ [45]. Because of the small single particle energy spacing, with typical

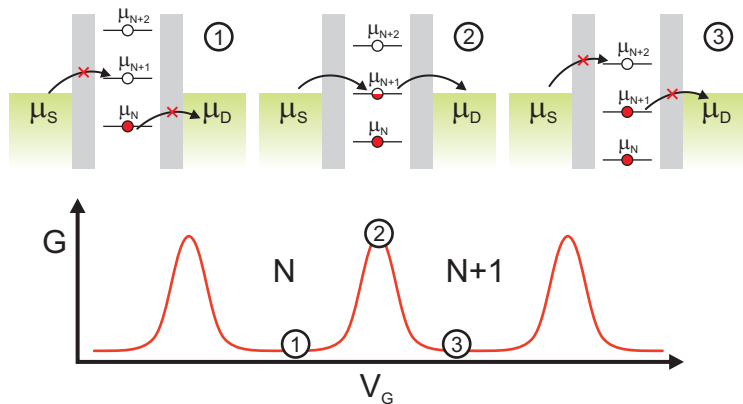


Figure 2.12.:

Linear measurements through a quantum dot: (1) Quantum dot containing N electrons while transport is Coulomb blocked. (2) The chemical potential of the $(N+1)$ th electron is in resonance with the leads. Single electrons hop on and off the dot, the charge oscillating between N and $N+1$, giving rise to a finite current. (3) The dot charge is stable at $N+1$ and transport is again blocked.

values of some tens μeV , quantum dots are measured at temperatures under 1 K. Therefore to fulfill the linear response regime the electron-chemical potentials of the Source and the Drain have to be kept at the same level, ($\mu_S \cong \mu_D$). A voltage applied to a plunger gate coupled capacitively to a quantum dot influences the electrostatic potential of the dot, and can tune energy of the discrete levels, hence the analogy to a plunger.

While the quantum dot energy states are separated only by a small energy $\Delta\varepsilon_i$, the charging energy E_C for a small capacitor is large and can lead to a blockade, as in the situation in Fig. 2.12 (a), where N electrons are located in the QD. The $(N+1)$ th electron cannot tunnel into the next level because the chemical potential of the state will be higher than the reservoirs, so for $\mu_N < \mu_S, \mu_D < \mu_{N+1}$, the transport is blocked. This is the so-called *Coulomb blockade*.

Changing the voltage applied to the plunger gate in order to align the chemical potential of the $(N+1)$ th electron with the Source and Drain chemical potentials ($\mu_N = \mu_S, \mu_D$) will allow electrons from the leads to tunnel in and out of the dot, resulting in a finite current flow, depicted in Fig. 2.12 (2). In this situation the charge on the dot is no longer quantized, oscillating between N and $N+1$. Further increasing the gate voltage will lower the chemical potential of the $(N+1)$ th electron until it is below the Source and Drain potentials $\mu_{N+1} < \mu_S, \mu_D$ and again the transport is blocked (Fig. 2.12 (3)). Sweeping the gate voltage on a larger scale will result in a series of peaks in the linear conductance $G = I_{SD}/V_{SD}$ that oscillate between zero (blocked transport) and a finite value, similar to the schematic on the lower part of Fig. 2.12. The peak spacing in gate voltage is given by:

$$\Delta V_G = \frac{C}{eC_G} \left(\Delta\varepsilon_i + \frac{e^2}{C} \right) \quad (2.32)$$

However, if we neglect the single level energy spacing $\Delta\varepsilon_i$, this

2. Theoretical background

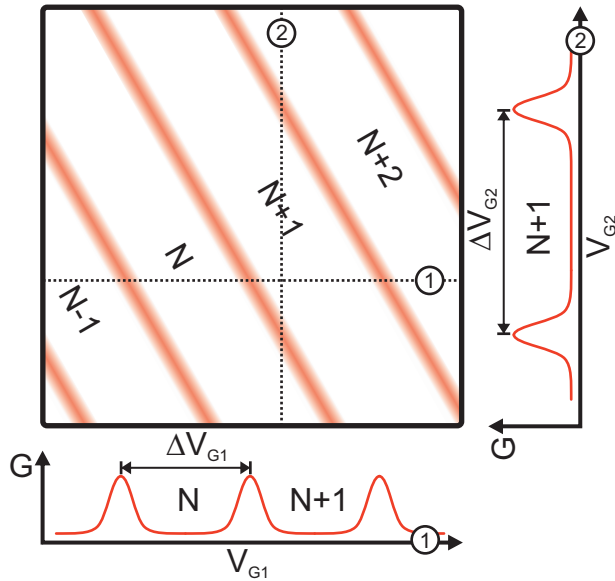


Figure 2.13.:

Charge stability diagram of a quantum dot showing the position of the Coulomb peaks as a function of gate voltages. The oscillation period in the direction of gate 1 ΔV_{G1} is different than in gate 2 direction ΔV_{G2} .

relation becomes $\Delta V_G = e/C_G$ which would result in periodic oscillations.

The charge on the quantum dot depends on all the voltages applied to the nearby leads, so if a second gate is attached one can map the dot charge dependence on two lead voltages at the same time, resulting in the so-called *charge stability diagram*, which is depicted in Fig. 2.13 as a function of two plunger gates. The periodicity of the conductance oscillation does not have to be the same in both directions, since plunger gates can couple differently to the electron island.

Non-linear measurements

An applied voltage to the Source or Drain would generate an electric field across the quantum dot which can make the response non-linear [45]. Thus measurements as a function of bias are usually termed *non-linear* measurements. The effect of an applied bias voltage is increased electro-chemical potential in a lead, e.g. Source with respect to the Drain potential, which is kept at virtual ground. The result is a transport window equal to $\mu_S - \mu_D = eV_{SD}$.

Beside the gate voltages, the position of the energy levels on the dot depends also on the bias voltage. In the frame of the constant interaction model it is assumed that the lead capacitances are constant, so the dot chemical potential has a linear dependence on the applied voltages. Thus, in the stability diagram as a function of gate voltage and Source-Drain bias, the regions where the charge on the dot is stable are defined by straight lines, forming the so-called *Coulomb diamonds*, depicted in Fig. 2.14. A trace in the gate voltage at zero bias (Fig. 2.14 (1)) will show the same succession of conductance peaks as in Fig. 2.13, and the charge on the dot N changes monotonously step-like with the gate voltage. In the Source-Drain bias direction, whenever an energy level enters the transport window the average charge on the dot changes similarly and the differential conductance ($\sigma = dI_{SD}/dV_{SD}$)² shows a peak (Fig. 2.14 (2)).

In the white regions in Fig. 2.14 the transport window is still smaller than the charging energy necessary to add the next electron, so the transport is Coulomb blocked (Fig. 2.14 (3)). The blockade is removed if the bias is gradually increased until the next free level enters the transport window (Fig. 2.14 (4)). The areas when one energy level is in transport are marked with light grey in Fig. 2.14. When the bias energy reaches the charging energy value $eV_{SD} = E_C$, one can observe trans-

²At zero bias the differential conductance is equal to the linear conductance

2. Theoretical background

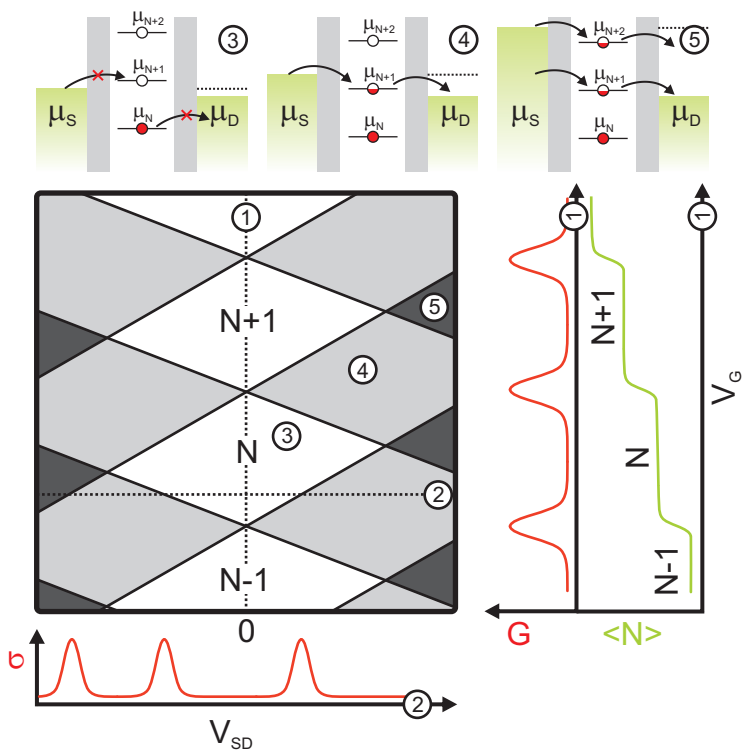


Figure 2.14.:

Charge stability diagram as function of bias and gate voltage exhibiting the Coulomb diamonds. (1) The zero-bias trace shows the Coulomb peaks, while the average charge in the dot $\langle N \rangle$ increases with gate voltage. (2) In the bias direction the differential conductance shows similarly a peak each time an energy level enters the transport window. In the white regions the transport is Coulomb blocked, corresponding to (3); in the light grey regions only one energy level is in transport (4), while in the dark grey regions two energy states are in transport (5).

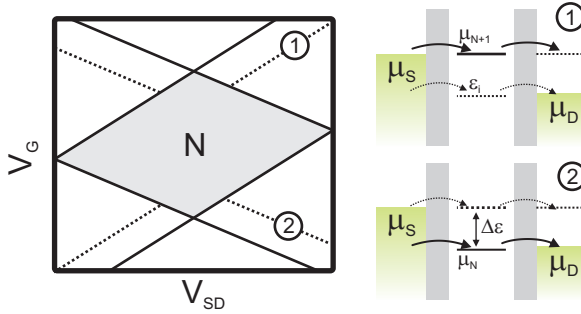


Figure 2.15.:

Excitation spectroscopy schematic of a quantum dot. The full lines mark increased differential conductance due to transport through the ground state. Dotted lines correspond to the opening of additional transport channels, related to tunneling through the excited states, as represented in the energy diagrams on the left side. (1) The first lower excited states in resonance with the Drain potential. (2) The first higher excited state comes into resonance with the Source potential.

port via two energy levels, corresponding to situation (5) and marked with dark grey in Fig. 2.14.

The non-linear measurements are also used to characterize the excitation spectrum and to estimate the single level energy spacing $\Delta\varepsilon_i$. On the outer edges of the Coulomb diamonds, when more than one level is in the transport window and $eV_{SD} \simeq \Delta\varepsilon$, an electron can either tunnel into the ground state ε_i or the first excited state ε_{i+1} and a secondary smaller peak is visible in the differential conductance (see Fig. 2.15). However the two states are not simultaneously occupied since the charging energy is still larger than the bias $E_C > eV_{SD}$, and because the electron will tunnel with smaller probability into the excited state, the peak given by the excited state will be much smaller than the one corresponding to the ground state.

2. Theoretical background

Until now we have discussed only resonant transport, given by sequential or first order tunneling events introduced in Section 2.1.2. However in the regions where transport is energetically forbidden, higher order tunneling phenomena, so-called *cotunneling*, can occur, yielding increased conductance. Cotunneling events that take place at zero bias are termed *elastic*, while non-zero bias events are called *inelastic*. An example of elastic cotunneling is the Kondo effect which will be discussed in the next section.

2.3. Kondo effect

The high versatility and tunability of quantum dots has kept them constantly in the focus of the scientific community for the past 20 years, with many breakthroughs achieved during this time, like controlled spin entanglement or single electron counting. One of the landmarks in quantum dot research was the realization of the artificial Kondo impurity in 1997 by D. Goldhaber-Gordon *et al.* [8]. In this section we introduce the main theoretical aspects that are used in the description of Kondo effect, starting from its discovery in bulk metals, followed by the application to quantum dots.

2.3.1. Introduction

The temperature dependence of the electrical resistivity of a pure metal is usually dictated by the phonon contribution, thus lowering the temperature and reducing the lattice vibrations will also lower the resistance, as the electrons can travel further without scattering. However at low temperatures around 10K the resistance will saturate at a constant level due to static defects in the crystal (solid line in Fig. 2.16). Deviations from this behavior can happen, as some metals can lose their resistance completely and become superconducting as the temperature is lowered below a certain threshold, when a phase transition takes place. In the 1930's another deviation from this behavior was observed for metals that contained a small amount of magnetic impurities, e.g. cobalt or iron. As the temperature was lowered, an increase in the resistance was observed after reaching a minimum, instead of a saturation. The temperature at which the resistance showed a minimum was seen to depend on the impurity concentration [46].

In 1961 P.W. Anderson published a simple model that describes the interaction of conduction electrons with the spin of an impurity [47].

2. Theoretical background

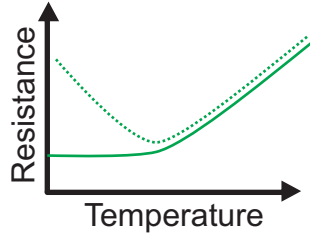


Figure 2.16.:

Schematic temperature dependence of the resistance of a pure metal (solid line) and a metal containing magnetic impurities (dashed line).

However it took until 1964 for a consistent explanation for the resistance minimum to appear, when Jun Kondo proposed a s - d exchange model [11] in which a localized impurity spin was coupled via an exchange interaction J to the delocalized conduction electrons. The Hamiltonian introduced by Kondo is:

$$H = \sum_{k\sigma} \varepsilon_k c_{k\sigma}^\dagger c_{k\sigma} + J_K S \cdot s(0) \quad (2.33)$$

with ε_k the energies of the k state in the conduction band, the creation (annihilator) operator $c_{k\sigma}^\dagger$ ($c_{k\sigma}$) for the k state with spin σ , and $J_K < 0$ the anti-ferromagnetic exchange coupling between the spin of the impurity S and the spin of the conduction electrons $s(0)$.

Using higher order perturbation theory he found the following temperature dependence of the resistivity:

$$\rho(T) = \rho_0 + aT^2 + bT^5 + c \{ J_K^2 + J_K^3 D(E_F) \ln(T) \} \quad (2.34)$$

where ρ_0 is the lattice resistivity, aT^2 the resistivity due to impurity potential, and bT^5 the phonon contribution. Only the third order term shows a low temperature dependence due to increased scattering

at the Fermi level, which leads to an increase in the resistivity. This model describes correctly the behavior of the resistivity for temperatures above a certain point, the so-called *Kondo temperature*, however it also incorrectly implies that in the $T = 0$ limit, it diverges to infinity. This problem was later addressed by P.W. Anderson who proposed a "scaling" method [48] and by K. Wilson through so-called "numerical renormalization" that overcame the shortcomings of perturbation theory calculations [49]. A comprehensive review of the Kondo effect can be found in Ref. [16].

A qualitative explanation can be given considering a single impurity energy state ε_0 localized below the Fermi level, $\varepsilon_0 < E_F$. Kondo effect arises only if the spin of the impurity is non-zero, in other words magnetic. In the simplest spin $\frac{1}{2}$ case, the impurity can be in either a spin up or spin down state. An itinerant conduction electron with opposite spin can couple to the impurity spin through so-called exchange processes, forming an intermediate virtual singlet state. The impurity electron will then leave the impurity site to one of the free states at the Fermi energy, and the itinerant electron will take its place. So, in the final state the spin at the impurity site is flipped. Classically such a process is forbidden without energy input into the system, however the Heisenberg uncertainty principle tells us that within a short time window $\Delta t = h/\varepsilon_0$ this is possible. Through many such spin flips, the impurity spin is screened by the conduction electrons, which gives rise to the additional scattering that leads to the increased resistivity below the Kondo temperature. The interaction between the localized spin and delocalized electrons can also be viewed as a many particle singlet state, with a binding energy E_K , given by:

$$E_K = k_B T_K \simeq \exp \left[-\frac{1}{J_K D(E_F)} \right] \quad (2.35)$$

where T_K is the Kondo temperature. At temperatures higher than T_K ,

2. Theoretical background

the singlet state is broken by the thermal energy and Kondo effect vanishes.

2.3.2. Kondo effect in quantum dots

A quantum dot embedded in a Fermi sea of electrons can be also seen as a localized impurity. If the number of confined electrons is odd then the total spin of the dot is necessarily different from zero, with a minimum value of $\frac{1}{2}$. In the late 80's it was theoretically predicted that Kondo effect should occur also in quantum dots [12]. This situation is similar to a bulk metal system containing an impurity. In a quantum dot all the electrons have to travel through the device, so in a Coulomb blocked situation with lowering the temperature the resistance of the dot should increase. However at low temperatures Kondo effect allows states that belong to the opposite leads to mix [50], thus decreasing the resistance, or increasing the conductance, in contrast to a metallic system where the scattering on an impurity increases the resistance.

Let us consider a dot with a single spin degenerate energy state ε_0

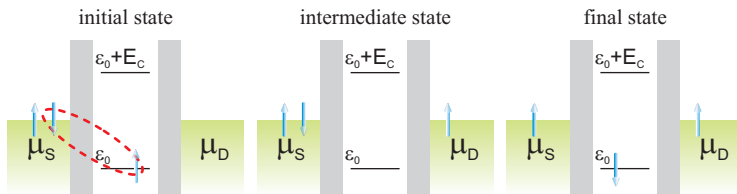


Figure 2.17.:

Anderson model for a single level quantum dot. This model assumes a dot with an energy level ε_0 , well below the chemical potentials of the leads, occupied by a spin up electron in the initial state. The electron can tunnel out of the dot into a forbidden intermediate state, and be replaced by an electron from the leads with opposite spin.

situated well below the Fermi level, occupied by a single electron with spin up so transport through this state is forbidden. The Coulomb charging energy necessary to bring another electron on the dot, must be larger than the other energy scales involved, i.e. $\varepsilon_0 + E_C > E_F$ (see the initial state in Fig.2.17). As in the case of bulk metals, the delocalized electrons in the leads screen the impurity spin, forming a singlet state. Due to the quantum mechanical uncertainty, the spin of the dot can tunnel into the leads, leaving the system into a "virtual" intermediate state (middle part in Fig.2.17), and the other spin forming the singlet will take its place filling the state on the dot. Hence, if the initial spin up will be replaced by a spin down electron, the quantum dot effective spin is flipped (final state in Fig.2.17).

The spin of the dot constantly fluctuates between spin up and spin down, and this changes the energy spectrum of the systems. In contrast to resonant tunneling, the Kondo effect processes are generated by exchange interactions, and because many electrons are involved this is called a *many-body phenomenon*. This generates the emergence of a very sharp peak in the density of states of the quantum dot. This Kondo resonance is pinned exactly at the Fermi level (Fig. 2.18), thus the system is always on resonance, regardless whether the position of the ε_0 state is changed by a plunger gate. In Fig. 2.18 the Kondo resonance width gives the energy scale, i.e. the Kondo temperature, while Γ is the ground state broadening due to tunnel coupling to the leads.

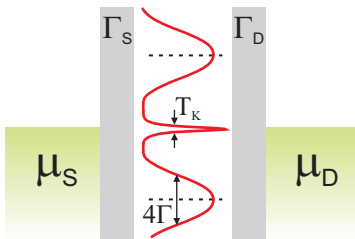


Figure 2.18.: Density of states in the Kondo regime. The successive spin flips lead to the emergence of a peak in the DOS pinned at the Fermi level.

2. Theoretical background

The Anderson model for a quantum dot

The Anderson Hamiltonian for a quantum dot is essentially the same as in the case of a bulk system, however as a quantum dot is investigated in transport measurements, it is connected to two (or more in some cases) leads. In the two lead case, it can be written as follows [51]:

$$H = H_S + H_D + H_{QD} + H_t \quad (2.36)$$

where H_S and H_D are the Hamiltonians of the electrons in the Source lead, and Drain respectively:

$$H_{S,D} = \sum_{k,\sigma} \varepsilon_{(S,D)k} c_{(S,D)k\sigma}^\dagger c_{(S,D)k\sigma} \quad (2.37)$$

with $c_{(S,D)k\sigma}^\dagger$ ($c_{(S,D)k\sigma}$) the creation (annihilator) operators, and dispersion $\varepsilon_{(S,D)k}$.

$$H_{QD} = \sum_{\sigma} \varepsilon_0 d_{\sigma}^\dagger d_{\sigma} + E_C d_{\sigma+}^\dagger d_{\sigma+} + d_{\sigma-}^\dagger d_{\sigma-} \quad (2.38)$$

is the quantum dot Hamiltonian, ε_0 is the impurity energy level, d_{σ}^\dagger the impurity electron creation operator and E_C the charging energy for double occupancy of a spin up and spin down.

A tunneling Hamiltonian H_t is taken into account since Kondo effect involves tunneling events from the leads onto the dot and vice-versa:

$$H_t = \sum_k \sqrt{U_{Sk}^2 + U_{Dk}^2} \left[c_{k\sigma}^\dagger d_{\sigma} + h.c. \right] \quad (2.39)$$

where $U_{(S,D)k}$ are hybridization constants of an energy state k on the impurity site with states in the leads, and are related to the level broadening by $\Gamma = \pi |U_{(S,D)k}|^2 D(E_F)$, with $D(E_F)$ the density of states

at the Fermi energy in the leads [12]. The obtained Hamiltonian for a quantum dot is essentially the same as in the case of bulk systems, thus the behavior of the Anderson model is retained under equilibrium conditions.

The Kondo temperature is related to the Anderson model parameters by [52]:

$$T_K = \frac{\sqrt{E_C \Gamma}}{2} \exp \left[-\frac{\pi \varepsilon_0 (\varepsilon_0 + E_C)}{E_C \Gamma} \right] \quad (2.40)$$

with Γ the broadening of the ε_0 energy state.

One of the controversial aspects of the theory of Kondo effect is the so-called *Kondo cloud*. This consists of the electrons that have previously interacted with the impurity spin, and contain information about each other [50], being a measure of the range to which the Kondo screening extends around the impurity. The Kondo cloud has an estimated radius given by:

$$r_K = \frac{\hbar v_F}{k_B T_K} \quad (2.41)$$

where $k_B T_K$ is the Kondo energy, with T_K the Kondo temperature, $v_F = \hbar k_F / m^*$ the Fermi velocity and $k_F = \sqrt{2\pi n_e}$ the Fermi wavevector [53].

2.3.3. Transport characteristics in the Kondo regime

In Figure 2.19 are depicted the main transport characteristics through a quantum dot in the Kondo regime. At zero magnetic field the dot energy levels are spin degenerate, and for an odd number of electrons (N) the total spin is different from zero. In the simplest case we could assume a total spin of one half for N =odd, while for $N+1$ and $N-1$ the simplest assumption is $S = 0$, in which case Kondo effect is not expected to occur. Thus looking at the linear conductance through the

2. Theoretical background

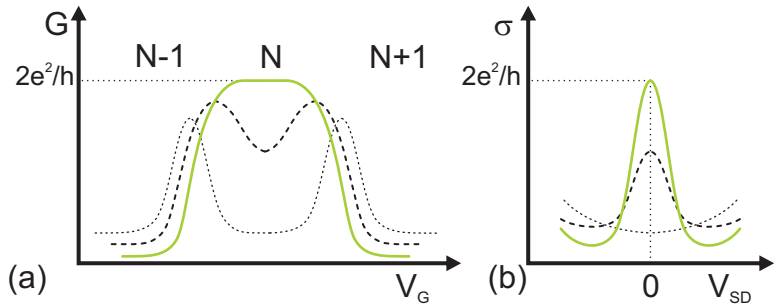


Figure 2.19.:

(a) Linear conductance through a quantum dot for different temperatures. In the Coulomb valleys corresponding to an odd electron number on the dot, the conductance is enhanced at low temperature. (b) Non-linear conductance in the Kondo valley, showing the Kondo resonance. The solid line corresponds to $T \ll T_K$ when the Kondo conductance reaches the unitary limit, the dashed line for $T \approx T_K$, while the dotted line to $T > T_K$.

dot (Fig. 2.19 (a)), in the Coulomb valleys with $N=\text{odd}$ the conductance is enhanced by the Kondo effect as the temperature is decreased, while in the valleys with an even number of electrons the conductance decreases due to reduced thermal excitation. At temperatures much smaller than the Kondo temperature $T \ll T_K$, the conductance reaches the so-called *unitary limit* of $2e^2/h$ (solid line in Fig. 2.19 (a) and (b)), that is the maximum conductance of a spin degenerate channel [54]. Which means that even though the dot is separated from the leads by tunnel barriers, Kondo effect allows a perfect transmission.

As a function of bias, the Kondo resonance is manifested as a zero-bias peak - also called zero-bias anomaly (ZBA) - in the conductance (Fig. 2.19 (b)), which decreases rapidly with increasing bias. At finite bias the Kondo resonance splits into two peaks pinned at the Fermi levels of the leads and in this case the Kondo correlations drop to zero

due to violation of the energy conservation (see e.g. [55]).

Estimating the Kondo temperature

The most relevant parameter accessible experimentally is the Kondo temperature, however its determination is not always straightforward. The easiest method is using the Kondo resonance width from the bias dependence [16]:

$$T_K = \frac{w\pi\Delta}{4k_B} \quad (2.42)$$

where $w = 0.4128$ is the Wilson number, k_B is the Boltzmann constant and Δ the half width at half maximum (HWHM) of the Kondo zero-bias anomaly.

The Kondo singlet is very sensitive to temperature variations and the conductance shows a logarithmic increase as the temperature is lowered. A schematic temperature dependence is depicted in Fig. 2.20. The variation of the conductance as a function of temperature is described by the following empirical formula, obtained using numerical

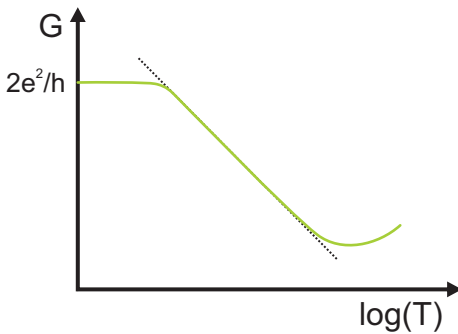


Figure 2.20.:
Temperature dependence of the Kondo conductance.

2. Theoretical background

renormalization group (NRG) calculations [56]:

$$G(T) = G_0 \left(\frac{1}{1 + (T/T'_K)^2} \right)^s \quad (2.43)$$

where

$$T'_K = \frac{T_K}{\sqrt{2^{1/s} - 1}}$$

where G_0 is the low temperature conductance while the s parameter is dimensionless and it is expected to have a value of ~ 0.2 for the spin one-half Anderson impurity model in the middle of the Kondo valley [9]. The fit with this formula provides a good estimation of the Kondo energy scale.

Another method of estimating the Kondo temperature is directly from Eq. 2.40. Although estimating the position of the impurity level with respect to the Fermi energy ε_0 and the charging energy E_C can be done with good precision for a quantum dot, determining the level broadening Γ is not straightforward. In the low temperature limit, $T \ll \Gamma$, the FWHM of the Coulomb peaks is 2Γ for a non-interacting quantum dot [58], while for a dot coupled via a Kondo singlet to the leads (interacting case) the Anderson model yields a FWHM doubled to 4Γ [59]. For large temperatures, $T \geq \Gamma/2$, the temperature dependence of the Coulomb conductance peak can be described by a convolution of the Lorentz fit of the peak full width at half maximum (FWHM) and the Fermi-Dirac function $3.52k_B T$. Extrapolating line fit of $\text{FWHM} = 0.78\Gamma + 3.52k_B T$ to $T = 0$ gives the intrinsic level broadening Γ [9]. However since several data analysis steps are necessary, this method of estimating the Kondo temperature can give large errors, so throughout this work we have used only the first two methods.

The Kondo temperature has a strong dependence on the tunnel coupling to the leads, thus T_K exhibits a minimum in the middle of

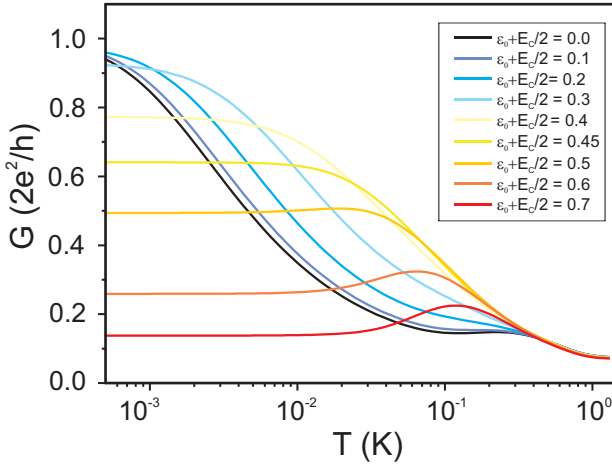


Figure 2.21.:

Temperature dependence as function of detuning in the Kondo valley. The data is calculated for the Single Impurity Anderson Model, where $\varepsilon_0 + E_C/2 = 0$ corresponds to the middle of the Kondo valley and $\varepsilon_0 + E_C/2 = 1$ to the charge degeneracy point [57].

the Kondo valley, the so-called *particle-hole symmetric point*, ($\varepsilon_0 = -E_C/2$) and it increases exponentially as we approach the charge degeneracy points ($\varepsilon_0 = 0, E_C$). In Fig. 2.21 are presented NRG calculations of the Kondo conductance temperature dependence for several positions of the impurity energy level ε_0 . As we move away from the middle of the Kondo valley ($\varepsilon_0 + E_C/2 = 0$) toward the charge degeneracy points, the description of T_K in terms of Eq. 2.40 becomes invalid. One can also observe that for values higher than $\varepsilon_0 + E_C/2 = 0.5$ the temperature dependence becomes non-monotonic.

2. Theoretical background

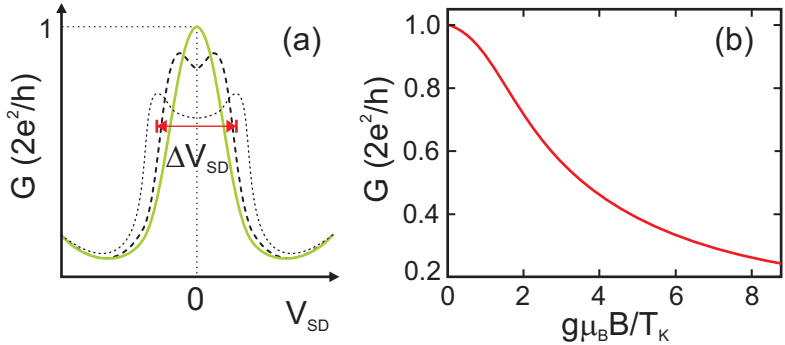


Figure 2.22.:

(a) The Kondo resonance of $B=0$ (solid line). For higher magnetic fields the Kondo resonance is split into two peaks located symmetrically around zero bias. (b) Zero bias Kondo conductance in an external magnetic field for $T=0\text{K}$ [57].

Kondo conductance in magnetic field

A magnetic field will lift the spin degeneracy of an energy level. If we consider the case for an in-plane magnetic field - here the orbital effects can be neglected - the level degeneracy is lifted by $\Delta\varepsilon_0$. The Kondo peak in the density of states is expected to be split by the Zeeman energy, resulting in two peaks each located at $\pm g^* \mu_B B$ (see. Fig. 2.22 (a)) [8, 10]. From the peak to peak distance ΔV_{SD} we can directly extract the Zeeman energy:

$$E_Z = e\Delta V_{SD} = 2g^* \mu_B B \quad (2.44)$$

where g^* is the effective electron *Landé* factor. Although g^* is material dependent, the value obtained with this method does not always coincide with the bulk material value, most likely due to the confinement. The splitting of the Kondo resonance in parallel magnetic field

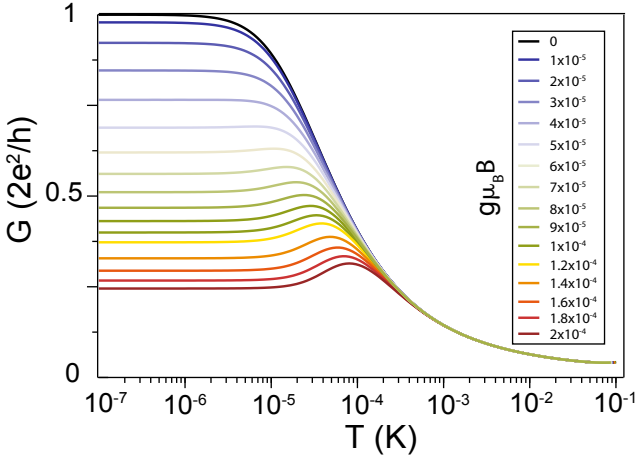


Figure 2.23.:

Temperature dependence of the zero-bias Kondo conductance in an external magnetic field.

is considered the most distinctive sign of Kondo physics.

With increasing magnetic field the peak splitting increases linearly according to Eq. 2.44, and because at equilibrium, i.e. $V_{SD} = 0$, the peak in the DOS is no longer present, the zero-bias conductance shows a monotonic decrease. In Fig. 2.22 (b) it's shown an NRG calculation of the zero-bias Kondo conductance at the particle-hole symmetric point with increasing magnetic field for $T=0K$, while in Fig. 2.23 there is the temperature dependence of the zero-bias Kondo conductance for increasing magnetic fields. An important feature here is the fact that for higher magnetic fields the temperature behavior of the conductance becomes non-monotonic, similar to the detuning from the particle-hole symmetric point situation in Fig. 2.21, although this is a signature of the splitting.

2. Theoretical background

3

Chapter 3.

Experimental techniques

The third chapter presents the experimental means used to produce nanometer scale structures and measure their transport properties. We will briefly present the technology used to obtain high quality 2DEGs through Molecular Beam Epitaxy (MBE), then discuss the layer sequence and properties of the wafers used throughout this thesis. The optical and AFM lithography steps will be later presented in detail, followed by the quantum dot structures produced. The chapter ends with the discussion of the cryogenic and low-current measurement setup used for investigating the samples.

3. Experimental techniques

3.1. Sample preparation

Fabricating devices on a nanometer scale is still a technological challenge. High quality materials are required as well as high resolution lithographic methods. Even though silicon is the most used material in the electronic industry today, for low noise applications the material of choice is GaAs. Lithographically patterned GaAs/AlGaAs heterostructures containing a two dimensional system have shown very high versatility and tunability in nanoscale applications. Modern material growth techniques allow production of 2DEGs with high homogeneity and different carrier densities [60]. Using the 2DEG as a starting point, one-dimensional (quantum wires or quantum point contacts) or zero-dimensional (quantum dots) systems can be patterned in countless combinations.

3.1.1. Heterostructures

A heterostructure is usually defined as a semiconductor structure in which the chemical composition changes with the position. The simplest example is a structure consisting of a single heterojunction - an interface within a crystal between two layers of different crystalline semiconductors [28].

High quality, defect-free heterostructure are obtained by combining single crystal growth for the substrate with cutting edge epitaxial methods. The standard growth method for single crystals is the *Czochralski* technique, where a small pure single crystal, called *seed*, is put in contact with the melted material. In an argon atmosphere the seed is slowly pulled out while rotating and the single crystal is thus formed around the seed. Being a binary material, single crystal GaAs is not as straight forward to grow as e.g. Si, due to the different vapor pressures of the components. To bypass this problem, the

3.1. Sample preparation

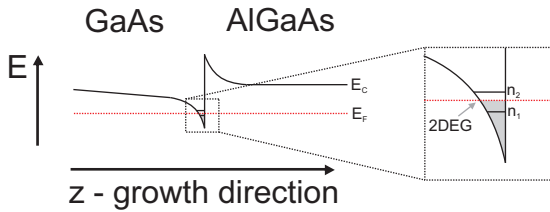


Figure 3.1.:

Conductance band minimum across the GaAs/AlGaAs interface - the conductance band minimum of GaAs bend downward creating a triangular potential well at the interface with AlGaAs. Using modulation doping the position of the Fermi energy can be adjusted so that only the first energy level in the potential well is occupied.

melt is covered with a fluid that does not mix with the components, a method named the *liquid encapsulated Czochralski* (LEC) [40]. After the growth, the single crystal usually in the form of a cylinder, is then cut into thin disks, the so-called *wafers*, and mechanically polished to reduce the surface roughness. The wafers thus obtained are used as substrates for epitaxial growing of layered structures, such as GaAs/ $\text{Al}_x\text{Ga}_{1-x}\text{As}$.

For fundamental research, samples are most commonly produced by Molecular Beam Epitaxy (MBE), a method that can grow epitaxial layers with atomic precision. To start with, a single crystal GaAs substrate is placed in an ultra high vacuum (UHV) chamber to avoid sample contamination, then heated and slowly rotated. The necessary material components for the heterostructure, like Ga, Al, Si for n-doping or B for p-doping, are placed in crucibles called *effusion cells* and heated until they start to sublime, thus creating a molecular beam. The gaseous elements then condense on the substrate where they can react with one-another forming a single crystal. The layer deposition process is monitored by *reflection high-energy diffraction* (RHEED), a

3. Experimental techniques

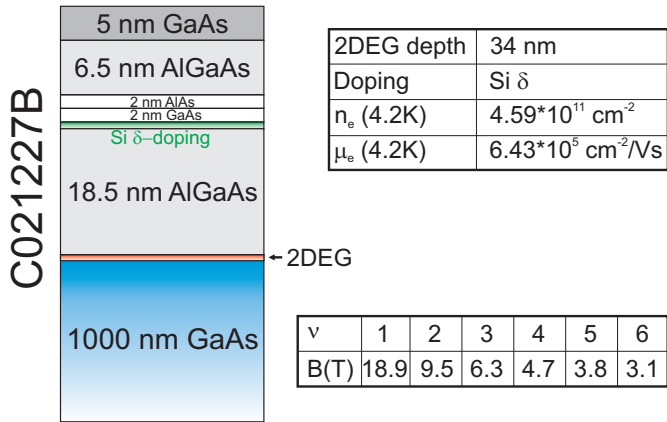


Figure 3.2.:

Layer sequence for wafer C021227B - MBE growth by M. Reinwald and W. Wegscheider, University of Regensburg

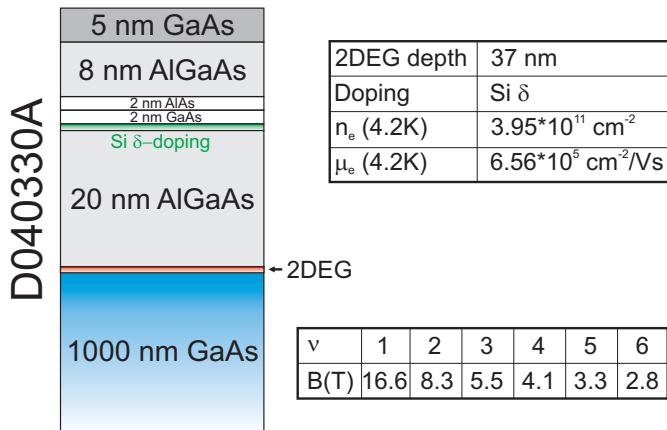


Figure 3.3.:

Layer sequence for wafer D040330A - MBE growth by D. Schuh and W. Wegscheider, University of Regensburg

3.1. Sample preparation

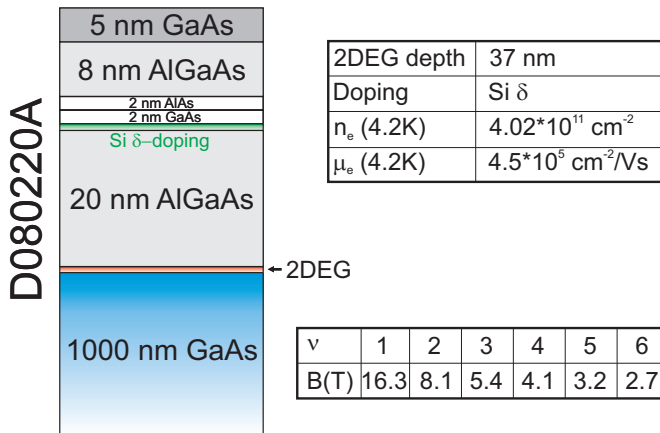


Figure 3.4.:

Layer sequence for wafer D080220A - MBE growth by D. Schuh and W. Wegscheider, University of Regensburg

technique that measures the reflection of an electron beam hitting the surface at a very small angle. The beam has a penetration depth of a few monolayers, so the created interference pattern is very sensitive to changes in the surface morphology.

The materials of choice for our purposes are GaAs and $\text{Al}_x\text{Ga}_{1-x}\text{As}$. Due to their nearly identical lattice constants ($a_{\text{GaAs}} = 5.65\text{\AA}$, $a_{\text{AlAs}} = 5.66\text{\AA}$) the heterojunction can be MBE grown nearly defect-free at an atomic level. The different band gaps of the two semiconductors ($E_{\text{GaAs}} = 1.43 \text{ eV}$, $E_{\text{AlAs}} = 2.16 \text{ eV}$), as well as different vacuum level energies, lead to band bending at the interface, creating a triangular potential well (Fig.3.1). The position of the Fermi level can be engineered by appropriate doping, so that only the first energy level in the potential well is occupied at 4.2K, realizing a two dimensional system at the heterojunction. In order to populate the potential well

3. Experimental techniques

with electrons, charged donors (usually silicon atoms) are placed in the growth process some tens of nanometers away from the GaAs/AlGaAs interface. The doping electrons relax in the potential well at the interface, thus creating a separation between the donor atom layer and the charge carriers in the 2DEG. This separation, called *modulation doping*, is responsible for creating a very smooth potential in the 2DEG.

In Fig.3.2, 3.3 and 3.4 the layer sequence and electronic properties of the three wafers used in this work are presented. The materials were grown in Regensburg, at the Institut für Experimentelle und Angewandte Physik by M. Reinwald and W. Wegscheider (C021227B - Fig.3.2) and D. Schuh and W. Wegscheider (D040330A - Fig.3.3 and D080220A - Fig.3.4).

3.1.2. Optical lithography

After the growth process, the wafers are cut into smaller pieces, usually about 2 square millimeters and laterally patterned through an optical lithographic process. The lateral resolution of the optically patterned samples is in the sub-micrometer range, therefore this requires that most of the fabrication steps to be carried out inside a dust-free *clean room* to avoid sample contamination. The optical lithographic steps are schematically represented in Fig. 3.5.

The first stage of the optical patterning is defining the so-called *mesa*, that is the usable sample area containing the 2DEG. The samples are cleaned with acetone in an ultra-sonic bath before depositing a photo-sensitive resist layer on the surface. For higher lateral resolution the resist layer has to be very thin and homogeneous, therefore the sample is rotated at high speed to achieve the desired result (60s at 4000 rpm in our case) - step 1 in Fig. 3.5. Through a baking process the solubility of the exposed resist can either be increased (so-called *positive* resist) or decreased (so-called *negative* resist) with respect to the unex-

3.1. Sample preparation

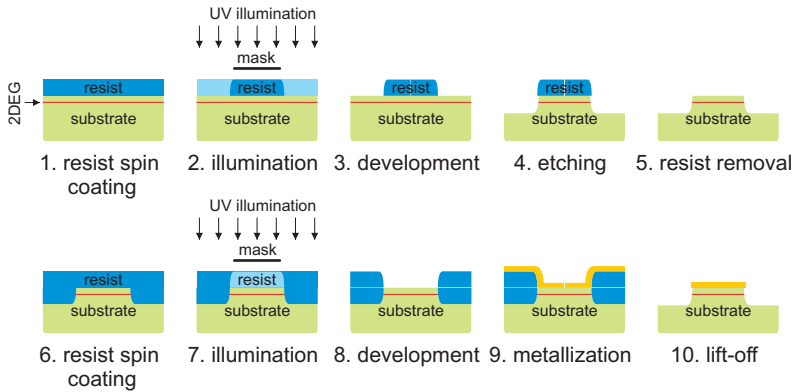


Figure 3.5.:
Optical lithography processing steps - schematic diagram

posed resist. Next, the sample is mounted into a mask aligner, a device that allows positioning the sample with respect to a mask. An illumination step follows, carried out using ultra-violet (UV) light, through a mask placed between the sample and an UV source in order to selectively expose the desired areas (step 2 in Fig. 3.5 and Fig. 3.6 (a)). Using a suitable developer the resist in the exposed areas is removed (step 3). The remaining resist on the surface acts as an etch mask in the wet chemical etching process that follows, thus defining the *mesa* (step 4 and 5 in Fig. 3.5 and Fig. 3.6 (b)). The etchant is a water diluted solution containing H_2O_2 for surface oxidation and an acid (typically H_3PO_4) that removes the oxide. The process is stopped by immersing the sample in distilled water.

The second processing stage is the metallization and contacting of the 2DEG. Because all the measurements presented throughout this thesis are current-voltage characteristics we need an electrical contact between the 2DEG and an attached wire. The first lithographic steps

3. Experimental techniques

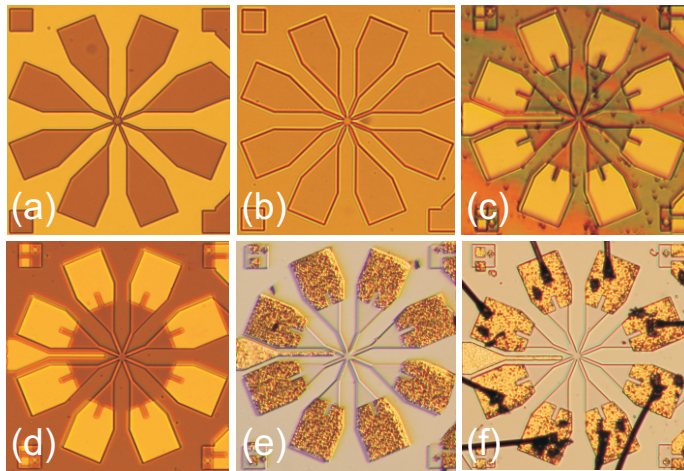


Figure 3.6.:

The sample during optical lithography - Sample after: (a) mesa development - resist is present in the darker areas. (b) mesa etching - the 2DEG is removed in the light colored area. (c) ohmic contact development - the yellow areas are developed, while the rest of the sample is still covered with resist. (d) metal deposition and lift off - yellow parts are covered with metal. (e) ohmic contact annealing. (f) wedge bonding

are repeated: the sample is cleaned again with acetone and a new layer of resist is deposited (steps 6 and 7). This time we use a negative resist, so the resist in the areas protected by the mask from the UV exposure will be removed in the development (step 8 in Fig. 3.5 and Fig. 3.6 (c)). In order to obtain a good contact we have to make sure that all the resist is removed from the areas where the metal should be deposited. Therefore in between steps 8 and 9 the sample is exposed to oxygen plasma. A side effect of the oxygen plasma is the oxidation of the exposed surface, which also degrades the contact. Since GaAs doesn't react with most

3.1. Sample preparation

acids, the oxide on the surface can be removed by immersing the sample in a suitable acid (e.g. 18% HCl). The sample is then placed in an UHV evaporation chamber and several metal layers are deposited on the sample surface (step 9 in Fig. 3.5)). A typical sequence is 40 nm Ge, 60 nm Au, 27 nm Ni, 150 nm Au. Afterwards the resist including the metal on top of it has to be removed in a *lift-off* process. This leaves the sample with the metal only in the desired areas (step 10 in Fig. 3.5 and Fig. 3.6 (d)).

A good contact should have in the first place a linear current-voltage characteristic - for this reason are called *ohmic contacts* - in the range relevant for the experiment (approx. $0.1 \mu\text{A}$), and secondly have a vanishing or very low resistance at low temperatures compared to the measured device (for GaAs a typical value is $1\text{k}\Omega$ at 4.2 K). After the lift-off, there is a Schottky barrier formed between the sample and the metal on the surface. Through an annealing process, i.e. heating the sample to 470°C for 120 s, the metal breaks the physical metal-semiconductor barrier and diffuses into the GaAs. From the three metallic components, germanium is the one that lowers the Schottky barrier, being an n-type dopant, and gives the ohmic behavior. Fig. 3.6 (e) shows the metallic pads on the sample after the annealing process. The last processing step is mounting the sample in a standard ceramic chip carrier and attaching some gold wires between the ohmic contacts on the sample and the chip carrier (Fig. 3.6 (f)).

3.1.3. Scanning probe nanolithography

The atomic force microscope

The atomic force microscope (AFM) [61] is a very powerful tool and can be used in a large variety of operational modes to investigate and modify surfaces. In comparison with the Scanning Tunneling Microscope (STM) [62] where the surface information is acquired via a tun-

3. Experimental techniques

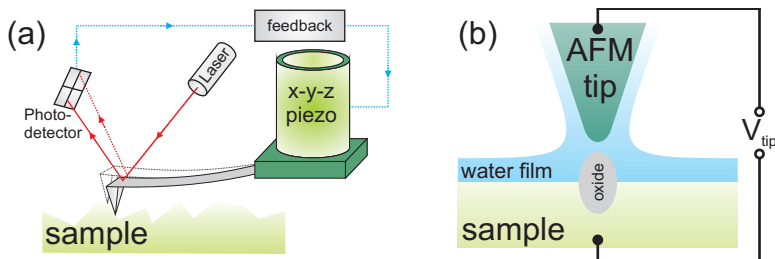


Figure 3.7.:

(a) Schematic diagram of the AFM. The setup consists of a piezo-crystal, a laser diode focused on the cantilever and a photo-detector. (b) Electrolytic cell for Local Anodic Oxidation - The water film on the surface of the sample acts as a catalyst for the chemical reaction generated by the current flow between the AFM tip and the sample, forming an oxide.

neling current that flows between a very sharp tip and the sample, the AFM uses the mechanical tip-sample interaction to build a surface profile, and therefore it does not suffer from the limitations imposed by the tunnel current. The AFM also is a promising lithographic tool for achieving further downsizing of electronic devices. Moving single atoms in a controlled way has been already demonstrated [63], nanostructures have been produced by engraving or nanomachining a surface [64, 65] and more recently by local anodic oxidation (LAO) [43, 66–70].

The principle behind an AFM is quite simple: a sharp tip attached to a piezo-resistive crystal is brought in contact with a sample and the tip-sample mechanical interaction is used to obtain the surface information. The piezo-resistive crystal can be deformed with sub-angstrom precision in all directions by applied voltages and is used to scan the tip across the surface. The interaction between the tip and the sample can be precisely monitored using a laser focused on the cantilever and mea-

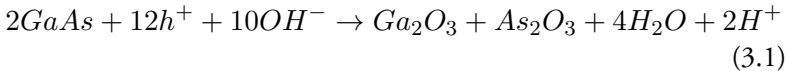
3.1. Sample preparation

asuring its deflection with a photo-detector (see Fig. 3.7 (a)). As the tip is moved across the surface the cantilever bends upwards or downward following the surface profile and the recorded deflection is assembled into a matrix that can be translated into a height profile of the surface.

The two main AFM operation modes are contact and tapping mode. As its name suggests, in contact mode the tip is in permanent contact with the surface, and the cantilever deflection is used as a feedback parameter to keep the force between the tip and the surface constant by adjusting the piezo in z-direction. In tapping mode the cantilever is oscillated near the sample surface so that at the lower oscillation point it touches the surface, or *taps* the surface. The cantilever oscillation frequency is chosen in such a way that a small amplitude change gives a large response in frequency, so-called *resonance frequency*. The signal acquired by the detector in this case is a sinus wave with the frequency of the oscillating tip and the feedback parameter here is the amplitude of the signal, i.e. cantilever.

Local anodic oxidation

Local anodic oxidation is a very convenient and flexible method that has been also used to directly pattern a two dimensional electronic system in a GaAs/AlGaAs heterostructure. In Fig. 3.7 (b) there is a schematic representation of the setup used for LAO with an AFM. Under ambient conditions on the surface of the sample there is a thin water film formed which acts as an electrolyte. A conductive AFM tip acts as a cathode, while the grounded sample acts as the anode. Applying a voltage between the tip and the sample generates a current flow, that in turn initiates a chemical reaction [71], locally oxidizing the GaAs surface under the tip:



3. Experimental techniques

where h^+ are positively charged holes in GaAs.

The result is that right underneath the oxide the 2DEG is depleted [66, 67]. The underlying mechanism that generates the depletion is explained in terms of surface states. In shallow 2DEGs, e.g. Fig. 3.2-3.4, due to the small distance between the 2DEG and the surface, only $\sim 10\%$ of the doping electrons relax into the electron system, while the remaining are captured by the surface states [40]. This makes the 2DEG very sensitive to surface modifications. The oxide created by LAO underneath the AFM tip protrudes also into the sample, sub-

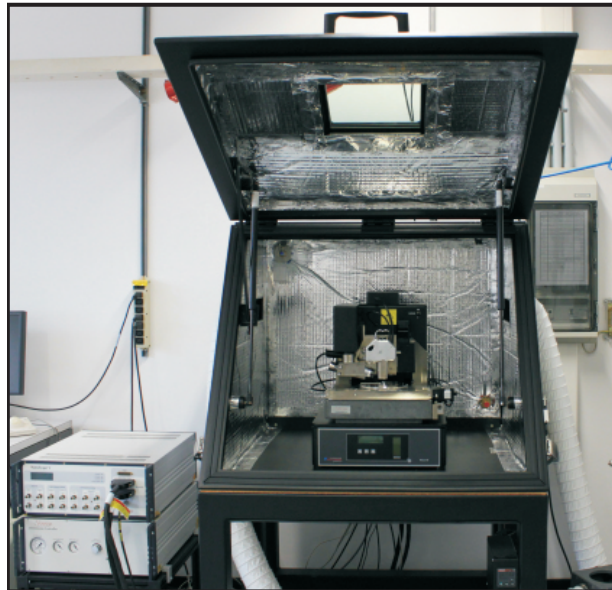


Figure 3.8.:

The AFM setup for Local Anodic Oxidation - The microscope is placed on an active table, inside an acoustic insulating hood. The atmosphere inside the hood is temperature and humidity controlled.

3.1. Sample preparation

sequently bringing the surface closer to the 2DEG. The extra surface states effectively change the internal electric fields and lead to the local depletion of the 2DEG. Using this technique one can create isolating regions that can be combined to define complex lateral nanodevices on the heterostructure [69, 70].

While the oxide itself does not play any role in the depletion of the electronic system, the aspect ratio of the oxide lines determines the shape of the grooves created on the surface, and consequently the shape of the created potential in the 2DEG. The ideal oxide line will create a potential that for a small voltage applied on one side generates a large field effect on the other side. This is equivalent to a large capacitor. The capacitive coupling between two regions is mainly dictated by the thickness of the oxide lines, a thick oxide resulting in a poor coupling, i.e. small capacitance. On the other hand the depletion of the electronic system can also be viewed as a tunnel barrier, where the height of the barrier is determined by the depth (which is proportional to the oxide height) of the groove. The aspect ratio of oxide lines depends on several parameters, like ambient humidity, applied voltage, writing speed, tip geometry and material.

In Fig. 3.8 there is a picture of the AFM setup used in this work. The AFM is a Veeco Dimension V with a Nanoscope V controller. The small length scales on which the AFM operates makes it very sensitive to vibrations. To improve the quality and precision of the acquired data, the AFM is sitting on a table that actively compensates mechanical vibrations, and the whole setup is inside an acoustic isolating hood. The humidity inside the hood is externally controlled using a humid air flow.

3. Experimental techniques

3.1.4. Samples

In the present work the main objective was to create a system that allows the experimental realization and measurement of the classical two-impurity Kondo problem (2IKP). That means measuring the interaction between two solid-state embedded spins via non-local exchange interaction.

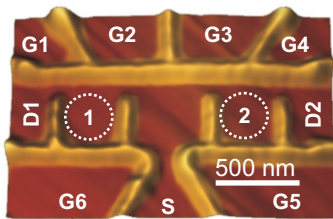


Figure 3.9.:
C021227B structure

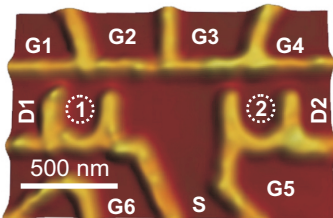


Figure 3.10.:
D080220A structure

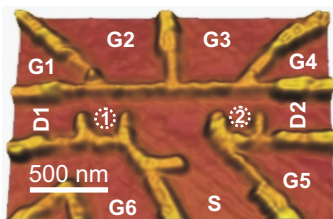


Figure 3.11.:
D040330A structure

3.1. Sample preparation

The system of choice was made of two quantum dots located at a certain distance apart, so that capacitive or tunnel coupling would not play a role. In Fig. 3.9, 3.10 and 3.11 are pictured the devices used in this work. The structures were produced by LAO with an AFM (see section 3.1.3) using the wafers introduced in section 3.1. The oxide lines that define the devices are highlighted in blue. The basic layout is in all three cases the same: two quantum dots (labeled 1 and 2 and marked by dashed circles) connected to the source contact (labeled S) via an open conducting region, and to individual drains (labeled D1 and D2). Six in-plane gates, G1 to G6, coupled capacitively to the QDs are acting as plunger gates, controlling the position of the discrete energy levels on the dots. Due to their relatively large area compared to the QDs, the gates are also controlling the coupling to the leads. Beside the different materials used, the device geometry is also varied. The quantum dots in the C021227B structure (Fig. 3.9) have a lithographic diameter of ~ 300 nm, and are placed ~ 600 nm apart, including the width of the oxide lines. In the case of structure D080220A we find a diameter of ~ 150 nm for both quantum dots, with a distance in between of ~ 700 nm, while the D040330A structure is characterized by a diameter of ~ 125 nm for QD1 and ~ 140 nm for QD2, with a distance of ~ 750 nm in between. In order to decouple the region between the dots from the Source, we have also designed the samples with a small 1D constriction between the central region and the Source. Their electronic properties will be discussed in the next Chapter.

3. Experimental techniques

3.2. Measurement setup

Measuring the current and conductance of a mesoscopic system is not straight forward. The relatively small single level energy spacing of a quantum dot requires a small thermal carrier energy and low-noise setup. The first is achieved by cooling the sample to very low temperatures in a cryostat. The second, by applying and detecting small signals, avoiding ground loops, using suitable signal filtering and proper wiring. Both will be discussed in the following.

3.2.1. The dilution refrigerator

The measurements presented in this thesis were performed in a Kelvinox TLM and in a Kelvinox 300 $^3\text{He}/^4\text{He}$ dilution refrigerator. While the working principle is the same in both cases, in the following we will discuss mainly the Kelvinox 300 system. This system can reach temperatures as low as 5 mK using the properties of liquid ^4He and the $^3\text{He}/^4\text{He}$ mixture. To reach down to the milikelvin range necessary for our measurement we use several cooling stages. First of all the cryostat insert (Fig. 3.12) is immersed in a liquid ^4He bath, which cools the insert to 4.2 K, the temperature of liquid ^4He under atmospheric pressure. To cool the inset further the part of the insert containing the other cooling stages (Fig. 3.12) are placed in an inner vacuum chamber (IVC) to reduce the thermal exchange with the ^4He bath. The dilution fridge uses two continuous cooling circuits. One is the ^4He circuit, the so-called 1K-pot, with a temperature of ~ 1.5 K. Liquid ^4He is let into the 1K-pot from the main bath and is pumped on it, reducing its vapor pressure, which in turn cools the liquid. At 1 mbar it reaches a temperature of 1.2 K [40].

The second circuit of the fridge is the $^3\text{He}/^4\text{He}$ mixture closed loop. The mixture is stored at room temperature, so it is pumped into the

3.2. Measurement setup

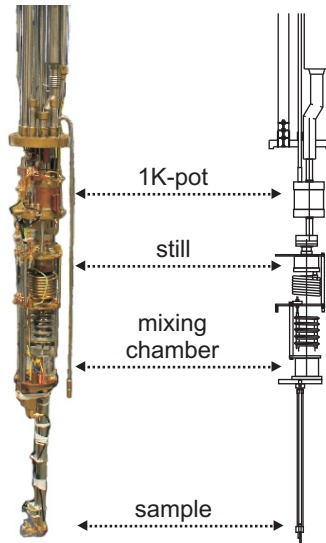


Figure 3.12.:

Kelvinox 300 dilution refrigerator with the cooling stages marked

cryostat in the gas phase. The inlet is thermally coupled to the 1K-pot, so the mixture is first cooled to 1.5 K. We know that at ~ 4.2 K ^4He becomes liquid and at ~ 2.17 K undergoes a phase transition into a superfluid state, while ^3He liquifies at ~ 3.19 K under atmospheric pressure [40]. So initially the mixture condensates in the mixing chamber, and the temperature is further reduced by pumping on it. Below 860 mK the mixture goes through a phase separation into a ^3He -dilute phase and a ^3He -concentrated phase. Since ^3He is lighter than ^4He , the ^3He -concentrated phase will be formed on top of the dilute phase. The mixing chamber is connected to a heated still (around 600 mK) through a pipe that reaches the lower phase, i.e. the ^3He -dilute phase. Therefore ^3He is taken from the dilute-phase and evaporated (at this

3. Experimental techniques

temperature the vapor pressure of ^4He is negligible, so only ^3He evaporates). Being a quantum fluid, the $^3\text{He}/^4\text{He}$ ratio in the dilute phase is constant, so while ^3He is pumped out through the still, other ^4He atoms are passing the phase boundary from the concentrated to the dilute phase. This process consumes latent heat and the mixture becomes colder, reaching the millikelvin range. The evaporated ^3He is circulated through an external pump and recondensed in the mixing chamber, thus maintaining a continuous cooling cycle. The sample is cooled either by thermal coupling to the mixing chamber via a cold finger (as in Fig. 3.12), or by directly immersing it in the mixture.

3.2.2. Electrical setup

In Fig. 3.13 and 3.14 we have sketched the simplified setups for the transport measurements performed throughout this work. In the setup in Fig. 3.13 the oscillating voltage from a EG&G 7200 lock-in ampli-

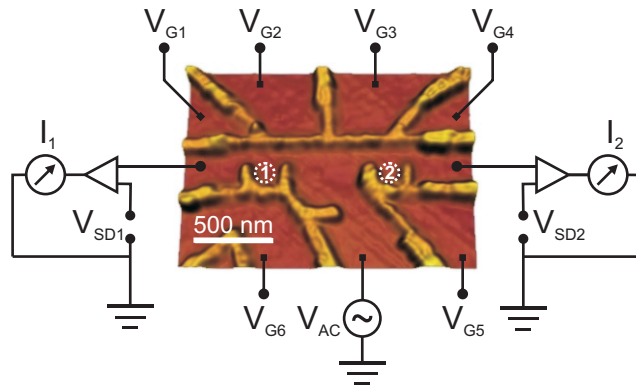


Figure 3.13.:
Measurement setup for samples C021227B and D08022A.

3.2. Measurement setup

fier V_{AC} is added with the DC signal V_{SD} from a digital-to-analog converter IOtech DAC488HR, and supplied to the Source contact of the sample (a schematic of the adder is provided in Appendix D, in Fig. D.2). To increase the precision of the applied voltages, the AC signal is divided by a factor of 10000 and the output amplitude is $10 \mu\text{V}$ (to keep the excitation power as low as possible) at a frequency of 83.333 Hz (it will be discussed later why we have chosen this particular frequency). The DC signal is similarly divided by a factor of 2000, thus using the DAC outputs in the $\pm 10 \text{ V}$ range we can apply up to $\pm 5 \text{ mV}$ with a precision of $\sim 150 \text{ nV}$. The two drains, D1 and D2, are connected each to an Ithaco DL 1211 current amplifier that picks up the currents flowing through the left and right dot. The amplifier output is split between the lock-in, for the AC measurement, and a Keithley 2000 multimeter, for the DC measurement. Before the multimeter, the signal is low-pass filtered to remove the oscillating AC signal that would otherwise compromise the accuracy of the DC measurement. The multimeter further uses an internal digital filter that averages over 5 powerline cycles (1 PLC=50 Hz=20 ms), keeping the DC measurement in phase with the AC frequency - 3 times the lock-in frequency 83.333 Hz equals exactly 5 PLCs. The in-plane gate voltages are supplied by other DAC ports and are all fed through 1 Hz low-pass filters before reaching the sample.

In the first setup (Fig. 3.13) the potential of the Drains is kept on the virtual ground defined by the current amplifiers, while the Source potential is basically defined by the V_{SD} voltage. The main difference in the second setup (Fig. 3.14) is that now the Source contact is put to ground via a 50Ω resistor, while we apply two DC signals on the drains using the optional external bias ports of the amplifiers. Basically now the DC virtual ground of the amplifiers is given by two externally supplied potentials set by the DAC. A detailed schematic of the signal and grounding setup can be seen in Fig. D.1 from Appendix D.

3. Experimental techniques

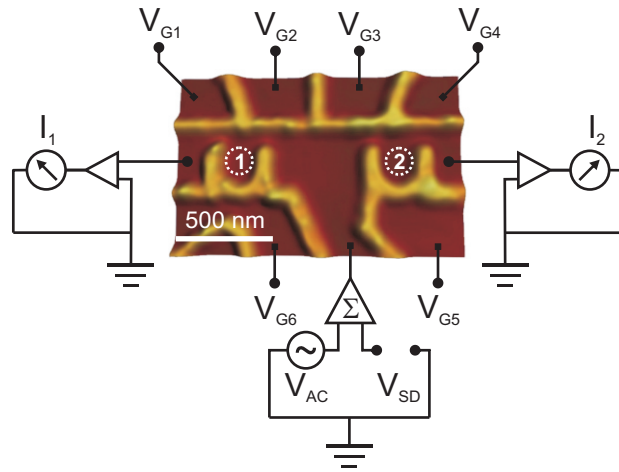


Figure 3.14.:
Measurement setup for sample D040330A

4

Chapter 4.

Inelastic Cotunneling Spectroscopy

This chapter covers measurements of higher order tunneling phenomena in a few-electron single quantum dot. The inelastic cotunneling threshold for the first and second excited states are identified and we investigate the dependence of the cotunneling threshold on bias and perpendicular magnetic field. From a comparison with the Fock-Darwin spectrum we estimate the electron number contained in the quantum dot.

4.1. Inelastic cotunneling at zero-magnetic field

As it was introduced in Chapter 2.3 an elastic cotunneling process can be explained considering a virtual tunnel event of one electron involving only the dot ground state, a quantum mechanical process which gives rise to the Kondo effect. However, if the quantum dot is left in

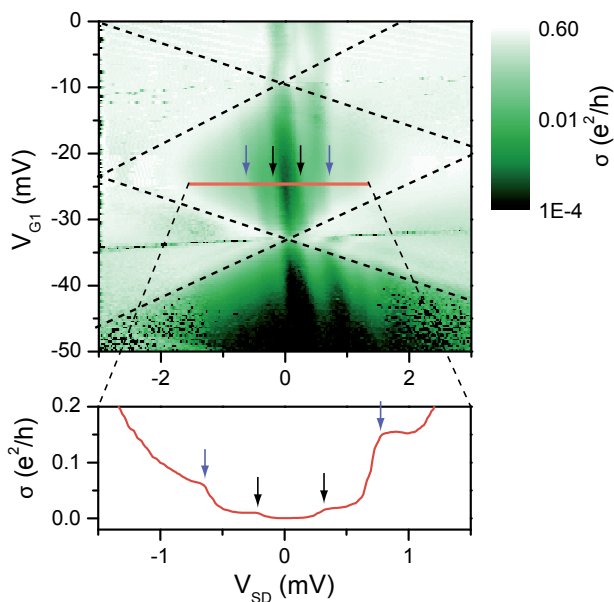


Figure 4.1.:

Coulomb diamond measurement of QD1 on sample C021227B (logarithmic color scale). (top) Inside the Coulomb diamond there are two thresholds corresponding to the cotunneling onset of the first (black arrows) and second (blue arrows) excited states. (bottom) Cut in the differential conductance taken at $V_{G1} = -25$ mV, along the line in the top plot.

4.1. Inelastic cotunneling at zero-magnetic field

an excited state after such an event, the cotunneling process is called inelastic and implies correlated tunneling of two electrons. We will show in the following that exploring the onset of inelastic cotunneling can be used to measure the excitation spectrum of a quantum dot with improved accuracy, as well as accurately identify a change in the ground state of the system.

The measurements presented here are performed on QD1 from sample C021227B. The sample is measured at a base temperature $T \approx 20$ mK, using the electronic setup in Fig. 3.13 with the transport path through QD2 completely cut off. Figure 4.1 shows a logarithmic scale differential conductance intensity plot of the charge stability diagram, as a function of bias and gate voltage. Dashed lines highlight the edges of the Coulomb diamond, marking the onset of first order tunneling via the ground state of the dot. The measurement yields an unusually large charging energy of the dot, that is $E_C \cong 3$ meV. A comparison with e.g. QD1 on sample D040330A (Fig. 5.1) discussed in the next chapter, shows that in this case the charging energy is roughly one order of magnitude larger. This fact suggests a large confinement energy, thus well separated energy levels.

Inside the Coulomb blocked area we observe two thresholds symmetric around zero-bias that mark an increase in the conductance. A cut at $V_{G1} = -25$ mV, along the red line in the top plot, shows that for each threshold visible in the contour plot we observe a corresponding step in the differential conductance. These features are corresponding to the onset of inelastic cotunneling through excited states [72, 73]. We extract an excitation energy for both thresholds using $e\Delta V_{SD} = \Delta\varepsilon_i$. Assuming the thresholds correspond to the first and second excited states we obtain $\Delta\varepsilon_1 \simeq 0.3$ meV for the first excited state, and $\Delta\varepsilon_2 \simeq 0.71$ meV for the second excited state. The fact that $\Delta\varepsilon_2 \sim 2\Delta\varepsilon_1$ indicates roughly a harmonic confinement.

A schematic diagram explaining the process is illustrated in Fig. 4.2

4. Inelastic Cotunneling Spectroscopy

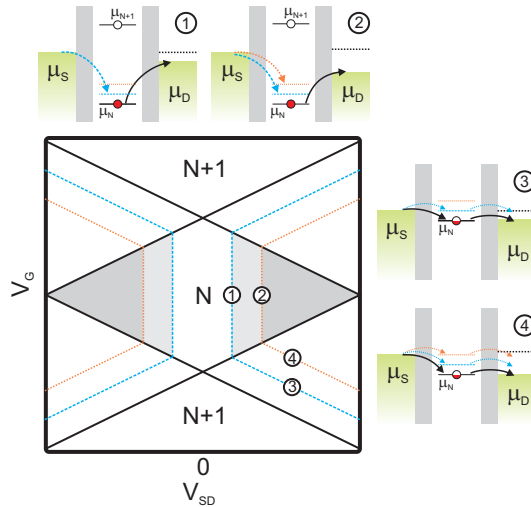


Figure 4.2.:

Schematic of a Coulomb diamond with two cotunneling peaks visible. Sloped lines mark the resonance of a dot energy level with the Fermi energy in the leads. (1) For $eV_{SD} \geq \Delta\varepsilon_{N+1}$, and (2) $eV_{SD} \geq \Delta\varepsilon_{N+2}$ inelastic cotunneling processes increase the conductance in the Coulomb blocked region. Illustration of the sequential tunneling through the ground state and (3) first and (4) second excited states.

for a quantum dot containing N electrons. Inelastic cotunneling sets in once the bias energy equals the energy spacing to the first excited state, $e|V_{SD}| = \Delta\varepsilon_1$. For instance, an electron on the ground state can escape to the Drain, while an electron from the Source tunnels into the first excited state (situation 1 in Fig. 4.2). Even though the process is called inelastic, the total electron energy is conserved, because the excitation energy is provided by the energy drop in the bias voltage eV_{SD} [72]. Thus the cotunneling through the first excited state sets in along the blue dashed lines inside the diamond. For the following

4.2. Inelastic cotunneling in perpendicular magnetic field

cotunneling process to occur, the electron on the excited state has to relax to the ground state and the excitation energy is lost, most likely by acoustic phonon emission [74].

In comparison with elastic cotunneling via a Kondo state, inelastic cotunneling currents are much smaller due to the relaxation time of the excited electron. For the second excited state (situation 2 in Fig. 4.2) the process is similar. That is when the bias window reaches the energy spacing to the second excited state, the electron on the ground state leaves the dot and an electron from the lead can tunnel either into the second or the first excited state. Therefore a second step in the cotunneling current appears. At the edges of the Coulomb diamond the cotunneling lines connect to the diagonal lines corresponding to the first order tunneling through the first and second excited state (situation 3, respectively 4 in Fig. 4.2).

4.2. Inelastic cotunneling in perpendicular magnetic field

A measurement as a function of bias voltage and perpendicular magnetic field, carried out for $V_{G1} = -25$ mV (corresponding to the solid line in Fig. 4.1) allows us to follow the cotunneling onset with magnetic field up to $B=6$ T. The data obtained is presented in Fig. 4.3, where the positions of the cotunneling onsets are marked with dashed (for the first excited state) and dotted (for the second excited state) white lines.

Already at fields up to 1 T a strong dependence of the cotunneling threshold corresponding to the second excited state can be observed. Around 0.2 T there is a crossing between the second and the first excited states, situation depicted in the first schematic (1) at the bottom of Fig. 4.3. Around 0.7 T the second excited state ε_2 reaches the ground state of the quantum dot (2 in Fig. 4.3). The second excited state has

4. Inelastic Cotunneling Spectroscopy

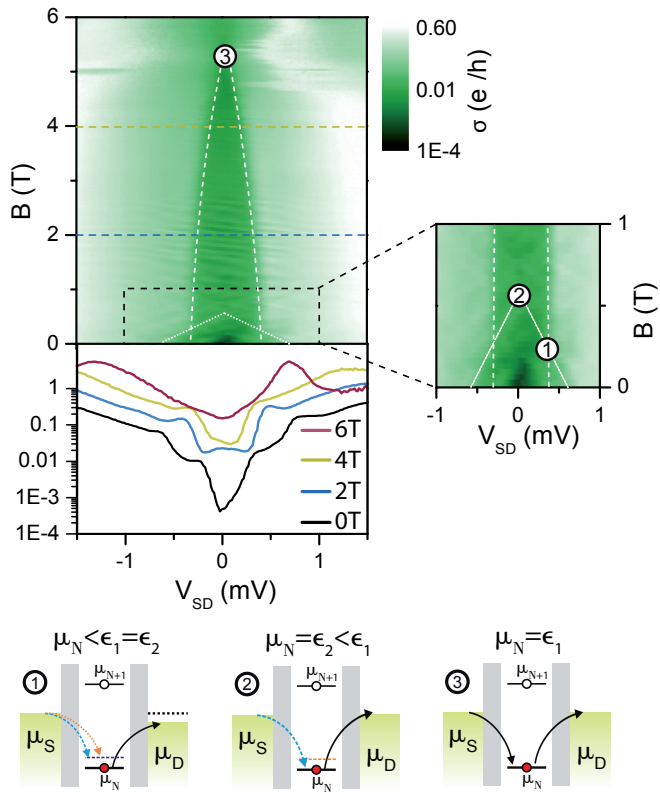


Figure 4.3.:

(top) Non-linear measurement of the cotunneling peaks as a function of perpendicular magnetic field for $V_{G1} = -25$ mV, along with cuts at $B=0,2,4,6$ T (bottom). We observe a strong magnetic field dependence of the second excited state (right). The numbers correspond to the schematic illustrations shown at the bottom.

4.2. Inelastic cotunneling in perpendicular magnetic field

a strong dependence on magnetic field, corresponding to an electron effective Landé factor of $g_{\varepsilon_2}^* \simeq 12$, while the first excited state ε_1 has a much lower magnetic field dependence with $g_{\varepsilon_1}^* \simeq 0.9$. In both cases the g^* factor is enhanced by the orbital effects induced by applying a field perpendicular to the 2DEG. Around 5.5 T the cotunneling gap Δ_{Cot} closes completely when the first excited state ε_1 crosses with the ground state. In the cuts taken at 0, 2 and 4 T (Fig. 4.3) the evolution of the cotunneling gap is visible. However in the 6 T cut, the two shoulders in the conductance at roughly ± 0.2 mV suggest a re-opening of the gap. This behavior could explain the crossing as a magnetic field driven ground state transition [75].

Figure 4.4 shows the cotunneling gap as a function of magnetic field measured from the contour plot in Fig. 4.3, together with the zero-bias conductance. Two steps are observed on the zero-bias conductance. The first step corresponds to the point where the two excited states become degenerate $\varepsilon_1 = \varepsilon_2$, related to the abrupt change in the cotunneling gap linear behavior. A linear fit of Δ_{Cot} in this region and extrapolating to 0 (dashed line in Figure 4.3) gives the magnetic field value at which it is expected to cross the ground state - $B \simeq 1.2$ T. The second step in the zero-bias conductance coincides with the closing of the cotunneling gap $\Delta_{Cot} = 0$, and marks the point where the first excited state crosses the ground state, around $B \simeq 5$ T.

The cotunneling onset behavior with magnetic field can be seen also in measurements as a function of bias and gate voltages at different field values, shown in Fig. 4.5. The differential conductance peaks corresponding to tunneling through the ground state of the systems are marked in all measurements with black dashed lines, while dotted lines mark transport via the excited states. Up to $B=6$ T the cotunneling onset is also evidenced in the figure by blue dotted lines. Although it is expected to remain constant as a function of gate voltage (see Fig. 4.2), it can be seen that the blue dotted lines marking the onset of cotunnel-

4. Inelastic Cotunneling Spectroscopy

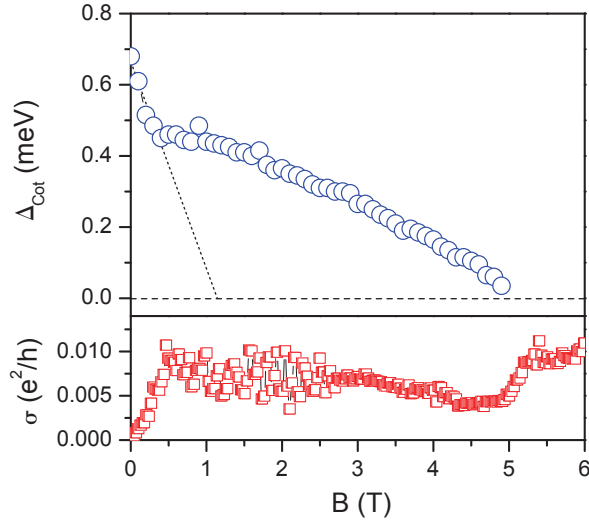


Figure 4.4.:

Cotunneling energy gap (top) and zero-bias conductance (bottom) as a function of magnetic field. Steps in the conductance mark the change in the ground state of the system.

ing are not parallel as expected, but having a finite slope. This feature is attributed to a modification of the confining potential as a function of gate voltage [72][75]. The cotunneling onset shows here the same behavior as in Fig. 4.3, that is a decrease with magnetic field, up to 5 T when the cotunneling gap closes ($\Delta_{Cot} = 0$). However the measurement at $B=6$ T shows a very weak cotunneling onset, which indicate the reopening of the gap, as expected for a ground state transition. For $B=0.15$ T and 2 T the conductance peaks corresponding to first order tunneling through the first excited state (dotted red line) are also visible, however only on the positive bias side which is given by resonant

4.2. Inelastic cotunneling in perpendicular magnetic field

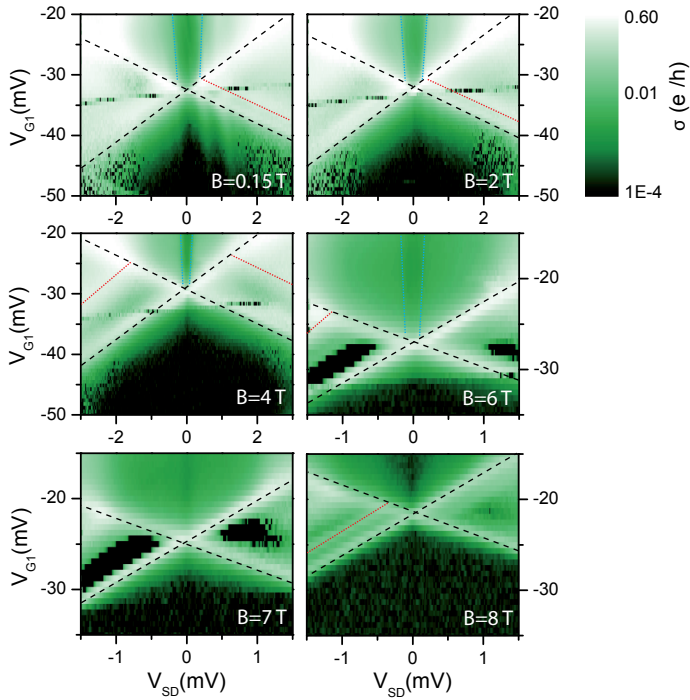


Figure 4.5.:

Non-linear measurements showing the cotunneling peaks at different magnetic fields. With increasing the magnetic field the cotunneling energy is reduced due to orbital effects.

transport with the Source lead. The first order tunneling peaks through the excited state (dotted red lines) connect at the Coulomb diamond edges to the cotunneling onset (dotted blue line). For magnetic fields higher than 4 T another excited state is visible in transport. In the measurements at $B=0.15, 2$ and 4 T, around $V_{G1} \simeq -35$ mV there is a

4. Inelastic Cotunneling Spectroscopy

disturbance in the measurements most likely caused by a charged trap due to the roughness of the confining potential.

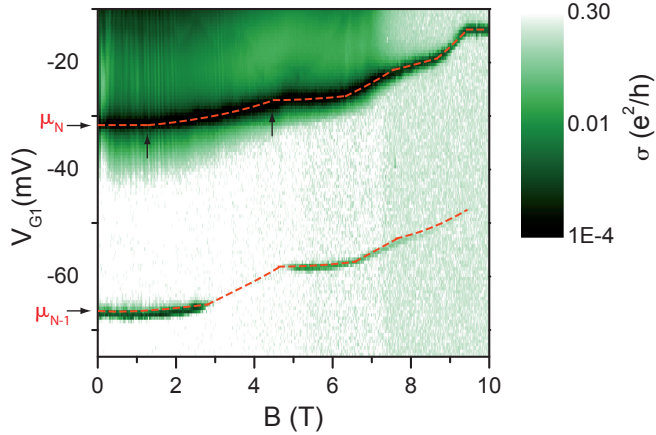


Figure 4.6.:

Measurement of the charge stability diagram in magnetic field showing the zig-zag behavior of the ground states (red).

In the differential conductance measurement as a function of perpendicular magnetic field and gate voltage (Fig. 4.6) we can observe the zig-zag pattern of the chemical potential of the $N-1$ th and N th ground states of the quantum dot. Each kink in the position of the chemical potential corresponds to a change in the ground state, as a result of a crossing with a lower energy state. The similar behavior in the position of the two visible peaks with magnetic field could indicate a spin pairing effect: the states belong to the same orbital, the lower one being filled with spin up, and the upper with spin down [76]. However a clear conclusion whether the N th electron ground state is a singlet or a triplet cannot be drawn. Furthermore, the fact that few kinks in the ground state are visible over a wide range of magnetic field, suggests a

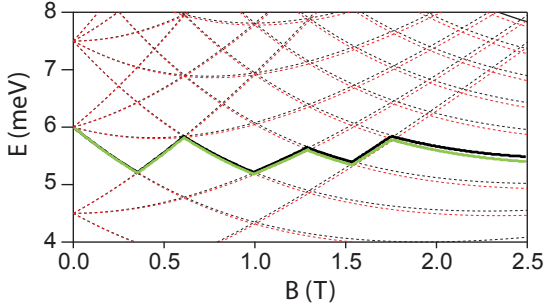


Figure 4.7.:
Fock-Darwin spectrum with the 13th and 14th electron peaks marked (solid lines).

few electron quantum dot with large confinement energy. The kinks in the chemical potential of the N th electron, μ_N , at ~ 1.2 T and ~ 5 T (marked by arrows in Fig. 4.6) correspond to the ground state changes visible also in the cotunneling conductance.

A qualitative comparison can be made with the Fock-Darwin spectrum. In Fig. 4.7 are highlighted the ground states of the 13th and 14th electrons for a parabolic harmonic potential with a confinement energy $\hbar\omega_0 = 1.5$ meV. The 13th and 14th ground states show a similar zig-zag behavior as the two peaks in Fig. 4.6. However, due to the larger confining energy of the quantum dot, there is a factor of 5 discrepancy in the magnetic field scale.

4.3. Summary

In this chapter we have investigated the inelastic cotunneling onset in a few electron quantum dot. The cotunneling thresholds corresponding to the first and second excited states are identified. From non-linear

4. Inelastic Cotunneling Spectroscopy

measurements as a function of perpendicular magnetic field we analyze the orbital effects on the excited states, by monitoring the excitation energy gap. We observe the transition between the excited states and the ground state in magnetic field, and find a corresponding step in the zero bias conductance through the dot. A qualitative comparison of the ground state behavior in magnetic field with the Fock-Darwin spectrum allows an estimation of the number of electrons contained in the quantum dot.

5

Chapter 5.

Kondo effect in Single Quantum Dots

In the following chapter we investigate the Kondo effect in single quantum dots. We start with the occurrence of the zero-bias anomaly at zero magnetic field and explore several methods for a quantitative estimation of the Kondo energy scale. Parallel magnetic field measurements yield the expected Zeeman splitting of the Kondo resonance, while in perpendicular magnetic field we observe a modulation of the Kondo conductance as a function of the magnetic field flux quantum.

5.1. Kondo effect in a single quantum dot

In the following, measurements of the Kondo effect in a single quantum dot are presented, starting with the occurrence of the zero-bias anomaly (ZBA) at zero magnetic field and a discussion about the methods used in this work for estimating the Kondo temperature. From measurements in parallel magnetic field we will extract the Zeeman energy and the effective electron g^* factor for our system. In the third part we discuss the model for the Kondo effect in perpendicular magnetic field and present measurements of the so-called *Kondo chessboard*, followed by introducing a method for extracting the Kondo temperature.

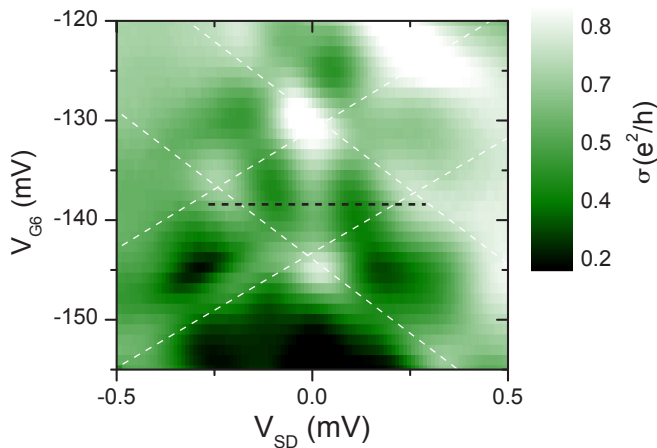


Figure 5.1.:

Non-linear measurement on QD1 from sample D040330A showing the Kondo resonance in the differential conductance. Dashed white lines mark the situation when the ground state is in resonance with the Fermi level in the leads, forming the Coulomb diamonds.

5.1.1. Kondo effect at zero magnetic field

As already introduced in chapter 2.3.2, Kondo effect is manifested as a peak in the differential conductance as a function of bias, the so-called zero-bias anomaly. In Fig. 5.1 is presented a measurement on QD1 from sample D040330A, where we observe the zero-bias anomaly in the differential conductance as a function of gate voltage and bias. In the figure, dashed white lines mark the edges of the Coulomb diamond, yielding a charging energy $E_C \approx 0.3$ meV. The electron number inside the dot is $N \approx 50$ estimated from the lithographic dimensions. Inside the Coulomb diamond, between $V_{G6} \simeq -145$ mV to -130 mV along zero bias, a peak in the conductance can be clearly observed, that is the signature of Kondo effect. Another important detail is that the Kondo ZBA does not extend in the nearby Coulomb valleys, as expected from the Anderson impurity model for an even number of electrons, although for many-electron quantum dots it has been observed that Kondo effect can occur in successive Coulomb valleys, as a signature of higher spin states [77].

Extracting the Kondo temperature from experimental data

An exact estimation of the Kondo energy scale from experimental data is not always possible. Due to this reason we will discuss and compare in the following two methods for estimating the Kondo temperature for the same measured data.

The most straightforward way to estimate the Kondo temperature is by extracting the half width at half maximum Δ from the resonance lineshape and calculate the Kondo temperature using Eq. 2.42. In Fig. 5.2 there is the cut taken along the black dashed line in Fig. 5.1 at $V_{G6} \simeq -139$ mV, showing Kondo resonance at zero bias. The peaks at $V_{SD} \approx -0.2$ mV and 0.3 mV correspond to the charge degeneracy points along the edges of the Coulomb diamond. The Kondo reso-

5. Kondo effect in Single Quantum Dots

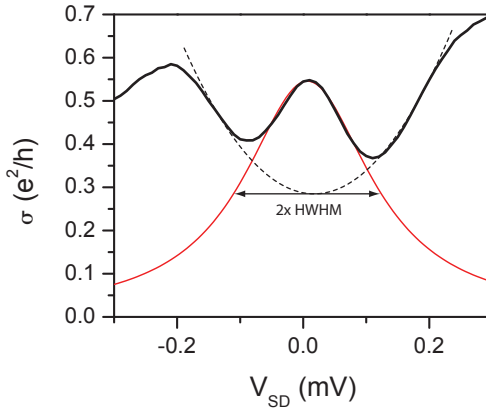


Figure 5.2.:

Lorenz fit of the Kondo resonance versus bias. The half width at half maximum (HWHM) value obtained from the fit yields a $T_K \simeq 460$ mK calculated from Eq. 2.42. The dashed line marks the expected shape of the Coulomb peaks, estimated through a parabolic fit.

nance is fitted with a Lorentz function (red line in Fig. 5.2) with an assumed zero background conductance. The HWHM value obtained from the fit is $\Delta = 0.125$ mV, which results in a Kondo temperature of $T_K \simeq 460$ mK, comparable to previously reported values in the same regime [9]. It must be mentioned that in samples with small charging energy - as in this case - the Coulomb peaks overlap inside the blocked area due to the tunnel broadening which raises the question whether assuming a zero-background conductance for the Kondo resonance fit is the right choice. In Fig. 5.2 a parabolic fit (dashed line) is used as a guide to the eye to estimate the overlap of the Coulomb peaks around zero bias.

Another method of estimating the Kondo temperature is from the temperature dependence. In Fig. 5.3 (a) is shown the temperature de-

5.1. Kondo effect in a single quantum dot

pendence of the Kondo resonance discussed in Fig. 5.2. The position corresponds to the minimum Kondo conductance where the situation is expected to be well described by the Anderson model. We observe that with increasing temperature the Kondo peak decreases and eventually disappears, which is a clear signature of the Kondo effect. As discussed in Section 2.3.2, increasing the temperature destroys the singlet formed between the delocalized electrons in the leads and the localized spin on the dot. As $k_B T$ becomes larger than the Kondo energy $k_B T_K$ the conductance drops.

In comparison, the Coulomb peaks - in Fig. 5.3 (a) it is visible only the negative bias Coulomb peak, located at $V_{SD} \approx -0.2$ mV - exhibit a slight decrease in the peak conductance with temperature, together with a large increase in the width of the peak, as expected for the Coulomb resonance lineshape [58]. At higher temperatures the Coulomb peak widths become large enough to dominate the zero-bias

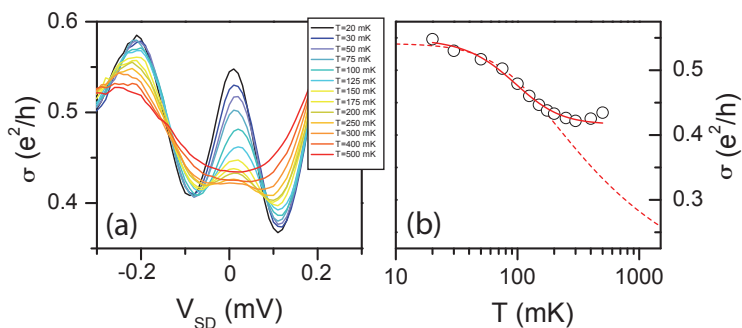


Figure 5.3.:

(a) Temperature dependence of the Kondo resonance as a function of bias taken along the dashed black line in Fig.5.1. (b) Kondo zero-bias conductance as a function of temperature. A $T_K = 92$ mK is obtained from fitting with Eq. 2.43.

5. Kondo effect in Single Quantum Dots

transport, hence the conductance at zero bias will start to increase. In Fig. 5.3 (b) we show the zero-bias conductance as a function of temperature. Up to 200 mK the conductance drops on a logarithmic temperature scale, and can be fitted with Eq. 2.43 (solid line in Fig. 5.3 (b)) if we assume a temperature independent background b . The parameters used in the fitting procedure are $b \simeq 0.416 e^2/h$, $G_0 \simeq 1.03 e^2/h$, $T_K \simeq 92$ mK with $s \simeq 1.4$, a factor of 5 smaller than the value obtained from the resonance width. The Kondo temperature T_K obtained from the fit of the temperature dependence should describe the point where the Kondo conductance reaches one half of its low temperature value, i.e. $\approx 0.55 e^2/h$ in this case. However we can see that the Kondo conductance drops only to $\approx 0.42 e^2/h$, about 24%, before it starts increasing. The reason is an overlap with the Coulomb peaks which are also broadened by the temperature, which results in a underestimation of the Kondo temperature. Another indication of the error in the Kondo temperature estimation is the value of the s parameter, expected to have a characteristic value of ~ 0.22 [9]. To make a comparison with the initial fit, in Fig. 5.3 (b) there is also plotted a fit of the data (dashed line) with $T_K = 460$ mK and $s = 0.22$ fixed, yielding a $G_0 \simeq 1.10 e^2/h$ and $b \simeq 0.137 e^2/h$. Because of the large discrepancy between the values obtained with the two methods, for quantum dots with small charging energy, the temperature dependence measurement can be used only as a qualitative method for estimating the Kondo energy scale.

Tuning the Kondo temperature

The ability to directly change the Kondo energy scale is a challenging task. However, the large number of tunable parameters available in the case of a quantum dot makes it possible in this kind of system. Since the Kondo conductance depends exponentially on the tunnel coupling

5.1. Kondo effect in a single quantum dot

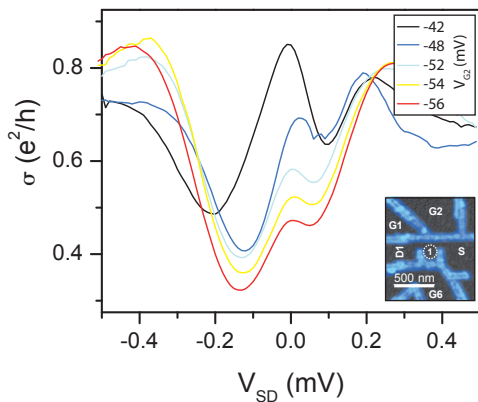


Figure 5.4.:

Tuning the Kondo temperature using an in-plane gate. A decreased voltage on gate 2 (inset) lowers the coupling to the right lead S , thus decreasing the Kondo temperature.

to the leads, one way to tune the Kondo temperature is by changing the position of the dot level with respect to the Fermi level in the leads using a plunger gate (e.g. V_{G6} in Fig. 5.1), although as the dot level nears the charge degeneracy points, the behavior in this regime is not well described by the Anderson model.

Another method is by influencing the tunnel barriers using an in-plane gate close to the barrier. In Fig. 5.4 we show several Kondo resonances for QD1 from sample D040330A (inset). It must be mentioned that the measurements were carried out in a different cooling cycle than the ones shown before. The resonances correspond to the same energy level and are measured in the middle of the Kondo valley, i.e. $\varepsilon_0 \simeq E_C/2$, for different voltages applied on gate $G2$. Making V_{G2} more negative increases the barrier height and/or thickness, hence the tunnel coupling to the leads is reduced, as well as the Kondo cou-

5. Kondo effect in Single Quantum Dots

pling. The measurements show also an increasing asymmetry in the resonance shape as V_{G2} is decreased, indicating a difference between the tunnel couplings to the source and drain leads. In the inset of Fig. 5.4 can be seen that gate G2 is closer to the right tunnel barrier, so it is expected that a more negative V_{G2} will decrease the coupling to the S lead. Using this method we can tune the Kondo temperature between ~ 720 mK for $V_{G2} = -42$ mV, and $T_K \simeq 450$ mK for $V_{G2} = -56$ mV, estimated from the resonance width.

5.1.2. Kondo effect in parallel magnetic field

In the following we will present measurements on QD2 from sample D040330A (see Fig. 3.11) in a parallel magnetic field. The quantum

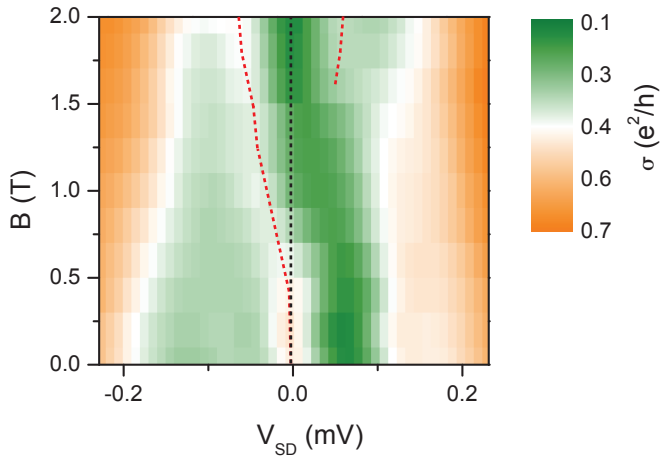


Figure 5.5.:

Conductance contour plot showing the bias dependence of the Kondo ZBA in parallel magnetic field. Red-dashed line marks the position of the Kondo peak.

5.1. Kondo effect in a single quantum dot

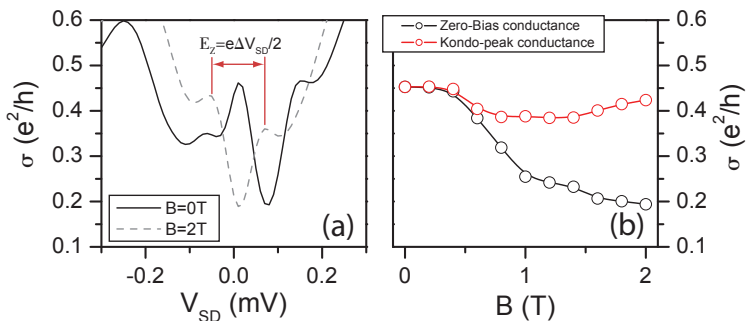


Figure 5.6.:

(a) Kondo resonance as a function of bias at $B=0T$ and $B=2T$ taken from the measurement in Fig. 5.5. (b) Zero-bias conductance (black) and Kondo peak conductance (red) as a function of in-plane magnetic field.

dots contains about 60 electrons estimated from the lithographic size. Non-linear measurements yield a charging energy $E_C \approx 0.3$ mV and single level energy spacing $\Delta\varepsilon_i \approx 50$ μ eV.

A magnetic field applied parallel to the 2DEG splits the spin-degenerate energy states of the dot, as already discussed in Chap.2.3.3. In Fig. 5.5 we show a measurement of the Kondo resonance in the differential conductance through QD2 from sample D040330A, as a function of in-plane magnetic field and bias. Up to a threshold value $B_t \cong 0.5$ T no splitting is visible, while for higher fields the ZBA starts to deviate towards negative bias.

For $B > 1.5$ T a symmetric peak appears for positive bias as well. The absence of the second peak up to ~ 1.5 T is explained in terms of a tunnel coupling asymmetry to the Source and Drain leads. Although from Eq. 2.44 the variation of ΔV_{SD} with magnetic field is expected to be linear, it is acknowledged that the Kondo peak splitting often yields a non-linear behavior (see for example Ref. [78]), visible also in the

5. Kondo effect in Single Quantum Dots

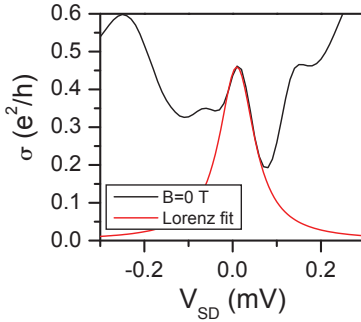


Figure 5.7.:

The zero field Kondo resonance from Fig. 5.5 as a function of bias, with a fit. The secondary peak at $V_{SD} \simeq -0.07$ mV is an inelastic cotunneling peak.

measurement presented here. Figure 5.6 (a) depicts the $B = 2$ T trace (dashed line) in comparison to the zero field trace. Two peaks are visible, located symmetrically around zero bias at $V_{SD} \cong \pm 0.062$ mV. Assuming the peak splitting is given by the Zeeman energy, using Eq. 2.44 we calculate a value of 0.53 for the effective electron g^* factor, with an error of $\sim \pm 0.12$, given a precision of ~ 15 μ eV in estimating ΔV_{SD} , resulting from the broadening of the peaks.

The threshold in-plane field B_t for the appearance of a splitting of the Kondo resonance gives an estimate of the Kondo temperature using the following relation [75]:

$$g^* \mu_B B_t \geq T_K k_B \quad (5.1)$$

With $B_t \simeq 0.5$ T and $g^* \simeq 0.53$ we obtain a $T_K \simeq 180$ mK. A T_K estimation using the Kondo resonance HWHM (shown in Fig. 5.7) and Eq. 2.42 gives in this case a value of 190 mK, being a proof of the reliability of the method.

In Fig. 5.6 (b) the zero bias conductance is shown with magnetic field (black), together with the Kondo peak conductance (red) taken along the red dashed line in Fig. 5.5. The threshold value at which the Kondo resonance starts to split is better visible in this figure. The

5.1. Kondo effect in a single quantum dot

zero-bias trace shows the expected monotonous downward trend with increasing magnetic field as the two Kondo peaks are moving further apart. However the Kondo peak conductance shows a step-like shape up to 1.5 T due to the lifted spin degeneracy of the energy state. At higher magnetic fields the peak conductance starts to increase as the position of the Kondo peaks nears the charge degeneracy points.

5.1.3. Kondo effect in perpendicular magnetic field

Kondo effect can be observed also at finite perpendicular magnetic field. Since one of its main conditions is the presence of both spin up and spin down in the leads, the observation of Kondo effect in magnetic field requires largely unpolarized leads. For filling factor $\nu_{leads} > 2$ (given by Eq. 2.17) the leads are still not fully polarized. At high magnetic fields the filling factor of the dot is lower, i.e. $\nu_{QD} < \nu_{leads}$

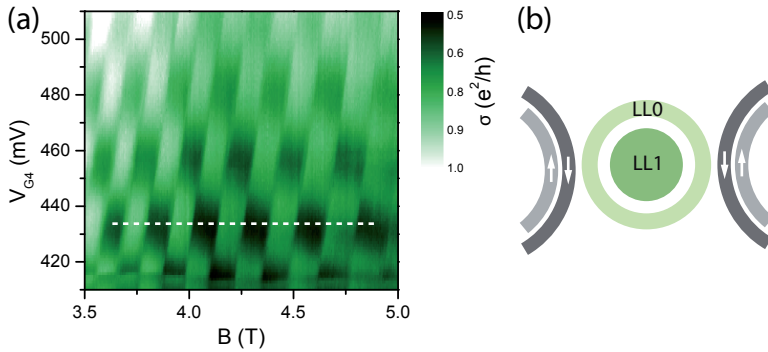


Figure 5.8.:

(a) Differential conductance through QD1 on D080220A showing the Kondo chessboard in perpendicular magnetic field. Bright color represents areas with high conductance. (b) Schematic diagram of the lowest dot Landau levels and edge states in the leads.

5. Kondo effect in Single Quantum Dots

and basically their properties are governed by the lowest Landau level (LL0) formed at the edge and higher Landau levels formed at the core of the dots (see also Sec. 2.2.3). Due to their separation, the tunnel coupling of Landau levels at the core to the leads is relatively low, therefore Kondo effect in perpendicular magnetic field involves only transport through the edge of the dot (LL0), which is closer to the leads (see Fig. 5.8 (b)). Consequently controlling the total spin of LL0 can turn the Kondo transport through the dot on and off.

The total spin number in the edge is given by the number of electrons contained, and it can be changed in two ways: either we add an electron from the leads in which case the total electron number of the dot changes, or we add an electron from the core to the edge, and keeping the total electron number constant. The first mechanism can be controlled by a voltage applied on a nearby plunger gate, while the second mechanism is the result of adding one flux quantum to the dot by increasing the magnetic field [79].

The result of these two mechanisms is a Kondo effect modulation as a function of gate voltage and magnetic field in a regular pattern of high-low differential conductance, generally referred to as the *Kondo chessboard* [79–83]. In Fig. 5.8 (a) there is shown the low temperature Kondo chessboard pattern exhibited by QD2 on sample D080220A, with alternating regions of high (bright) and low (dark) differential conductance as a function of the voltage applied on G4 and magnetic field. In both samples D040330A and D080220A we observe the Kondo chessboard up to 5.5 T. This corresponds to a filling factor of the leads $\nu_{\text{leads}} \simeq 3$, showing that the leads are not fully polarized up to this field value.

The tile periodicity ΔB in Fig. 5.8 (a) can be used for estimating

5.1. Kondo effect in a single quantum dot

the diameter of the quantum dot d with the following expression [77]:

$$d = 2\sqrt{\frac{N_\phi\phi_0}{\pi\Delta B}} \quad (5.2)$$

where $N_\phi = 1$ is the number of flux quantum and ϕ_0 the magnetic flux quantum. For $V_{G4} = 434$ mV, between 3.5 and 5 T we obtain a tile periodicity ranging from 0.108 to 0.152 mT, which in turn corresponds to a dot diameter of 150 to 130 nm, which fits very well with the lithographic diameter of the dot (150 nm). Assuming an electron density inside the dot equal to the 2DEG density, we estimate ~ 70 electrons on the dot.

Estimating the Kondo Temperature in magnetic field

In perpendicular magnetic field the confinement energy of the dot is changed, as well as the electron wave functions overlap in the tunnel barriers, which affects the coupling of the dot to the leads. Thus the Kondo energy scale is also modified by the magnetic field. In this case extracting the Kondo temperature from bias dependent measurements is not always possible because on the one hand the Kondo resonance is Zeeman split, and on the other hand the measurement is usually noisier which leads to broadening. Therefore in this case the only option is to estimate the involved energy scales from temperature dependent measurements.

Figure 5.9 shows a typical temperature dependence in the Kondo chessboard. The most striking feature is the strong temperature dependence of the background conductance ¹. It is also observable that the Kondo conductance is reduced by increasing temperature as expected, however in comparison with the temperature dependence at zero field

¹We consider as *background* the conductance in the regions that do not exhibit Kondo transport

5. Kondo effect in Single Quantum Dots

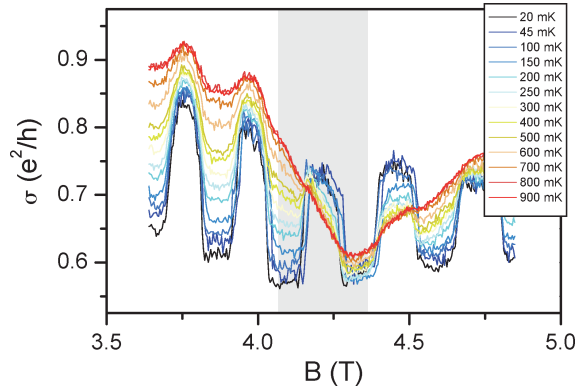


Figure 5.9.:

Temperature dependence in the Kondo chessboard taken along the dashed line in Fig.5.8.

(e.g. Fig. 5.3) here we can see a Kondo conductance even at 1 K. The reason for the higher Kondo coupling in perpendicular magnetic field is mostly due to the change in the confinement of the quantum dot and the proximity between the dot edge and the leads.

A quantitative Kondo energy scale estimation cannot be done in this case from the resonance width, given the relatively high magnetic field value, which induces a splitting of the ZBA. However from a qualitative analysis of the linear conductance temperature dependence one can extract the behavior of T_K with magnetic field. A problem arises from the strong temperature dependence of the background which compromises the quality of the data, and the fit at the same time. The problem can be solved by an estimative fit of the background, followed by its subtraction from the original data. In Fig. 5.10 (a) we show the Kondo temperature dependence from Fig. 5.9 after subtracting the background for each temperature trace (for further details regarding the

5.1. Kondo effect in a single quantum dot

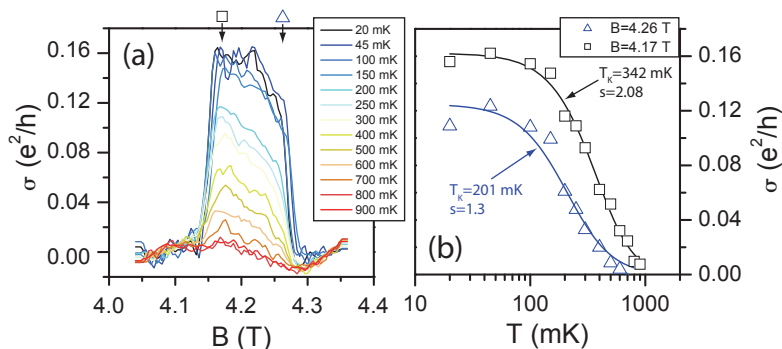


Figure 5.10.:

(a) Data from the highlighted area in Fig.5.9 with the background subtracted. (b) Data from (a) for $B=4.17$ T and 4.26 T fitted with Eq. 2.43 to extract the shape parameter s and the Kondo temperature.

procedure see also Fig. B.1 in Appendix B). In Fig. 5.10 (b) is shown the temperature dependence for two magnetic field values, 4.17 T and 2.26 T. Each set of data points have been fitted using Eq. 2.43, obtaining a $T_K = 342$ mK with $s = 2.08$ for $B=4.17$ T, and $T_K = 201$ mK with $s = 1.3$ for $B=4.26$ T the lower value being consistent with the lower conductance.

A fit for each point between 4.15 to 4.275 T using Eq. 2.43 shows that for both the Kondo temperature and the shape parameter s we obtain a roughly linear decrease with increasing magnetic field (Fig. 5.11). The explanation of this behavior lies in the orbital effects induced by perpendicular magnetic field. As mentioned before, at high perpendicular magnetic fields Kondo effect involves transport only through Landau level 0 (LL0) energy states. Since this measurement is done at fixed gate voltage, i.e. at fixed energy, as the magnetic field is increased, the ground state moves lower in energy (see e.g. Fig. 2.10) and

5. Kondo effect in Single Quantum Dots

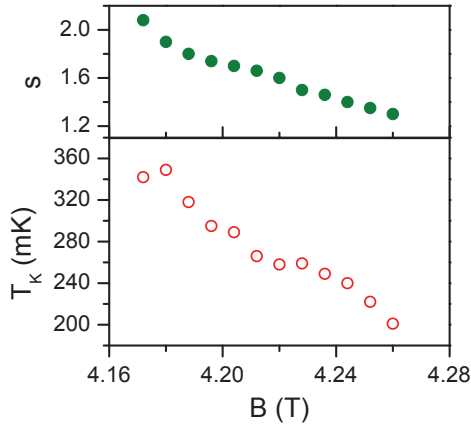


Figure 5.11.:

Kondo temperature (lower graph) and the shape parameter s (upper graph) obtained by fitting the data from Fig. 5.10 with Eq. 2.43.

the electron wavefunction is compressed. Thus the Kondo coupling is reduced, which explains the linear decrease of T_K . The shape parameter s shows a similar decrease with magnetic field, with values between 2 and 1.2, which indicate a clear departure from the 0.22 value for spin $\frac{1}{2}$ given by the Anderson model [9]. However due to the spin selection rules, it was observed that higher spin states can occur in the Kondo chessboard [82, 83], which would explain the values obtained for the shape parameter.

5.2. Summary

In this chapter we have explored the Kondo physics in single quantum dots. We have shown measurements at zero magnetic field of a Coulomb diamond exhibiting the Kondo resonance and verified its behavior with temperature as a typical fingerprint of Kondo effect. Two different methods for estimating the Kondo energy scale are compared and we establish that estimating the Kondo temperature from the resonance width gives better quantitative results. By changing the voltage of a nearby gate we can tune the Kondo coupling to the leads, as well as the coupling asymmetry of the quantum dot.

From parallel magnetic field measurement we measure the Zeeman splitting of the Kondo resonance, obtaining an electron g^* factor value close to the bulk GaAs value. The threshold value of the magnetic field at which a splitting of the Kondo resonance is visible yields a Kondo temperature in very good quantitative agreement compared with the value extracted from the low temperature resonance width. In perpendicular magnetic field we observe a flux quantum modulated Kondo chessboard up to high field values. From the temperature dependence we find that the Kondo temperature decreases with increasing magnetic field, in good agreement with the behavior of LL0 energy states in the Fock-Darwin spectrum.

5. Kondo effect in Single Quantum Dots



Chapter 6.

Kondo effect in RKKY-coupled Double Quantum Dots

In the present chapter we explore the tuning mechanisms of the RKKY exchange interaction strength in a system with two lateral QDs coupled to a central open conducting region. We study how the exchange interaction strength changes as a function of the Kondo energy scale asymmetry, and we probe the anti-ferromagnetic character of the RKKY interaction in parallel magnetic field. Applying a perpendicular magnetic field generates a chiral coupling between the quantum dots via the edge states and we probe the exchange coupling in the Kondo chessboard via temperature and bias dependent measurements.

6.1. Introduction to the Rudermann-Kittel-Kasuya-Yosida interaction

The Kondo effect alone, as other many-body phenomena, is a very interesting subject from both the theoretical, as well as experimental point of view, judging from the number of papers published on the subject these past 50 years. As it became clear that the smallest extensions to the Anderson single impurity model led to new behaviors, more exotic Kondo systems came into the focus of the scientific community. One of these extensions consisted of a system of two Kondo Impurities (2IK) coupled to the Fermi sea, while being coupled to each-other at the same time via exchange interactions, the so-called 2IK model. This type of exchange interaction allows the coupling between two spins beyond the nearest-neighbor approximation restraint, and it has been proposed as a spin entanglement method over long ranges, with possible applications to quantum computing [19].

In the late 50s it was established that magnetic impurities in bulk metal systems interact with one another via indirect exchange interactions, the so-called *Rudermann-Kittel-Kasuya-Yosida interaction* or RKKY [13–15]. Due to their non-zero nuclear magnetic moments, an exchange coupling mediated by the conduction electrons appears between two impurities located at a certain distance apart. The process is initiated as the magnetic moment of one nucleus scatters a conduction electron via the hyperfine interaction between electronic and nuclear magnetic moments. The scattered electron thus will carry some information about the magnetic moment. When the electron scatters a second time on another nuclear magnetic moment, the information from the first moment is transmitted, and the two nuclear moments "see" each-other this way.

6.1. Introduction to the Rudermann-Kittel-Kasuya-Yosida interaction

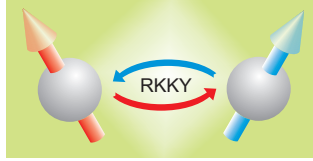


Figure 6.1.:
Two spins in the Fermi sea coupled via RKKY interaction

When two magnetic impurities are separately screened by the Fermi sea, giving rise to the Kondo effect, and at the same time the conduction electrons mediate the exchange coupling between the impurities, there is a competition between the ground states of the system. On the one hand the Kondo effect continuously flips the spin of the impurity as it was described in Chapter 2.3, while the RKKY interaction freezes the impurity spins in a singlet or a triplet state [16]. It is known that the Kondo effect modifies the thermodynamic properties of a system, like the specific heat c and the susceptibility χ , in a precise universal ratio, called the *Wilson ratio*, $R_W = (\delta\chi_{imp}/\chi)/(\delta c_{imp}/c) = 2$, which measures the relative contribution of the impurity to the total susceptibility χ , divided by the relative contribution of the impurity to the total specific heat c [49]. However in the 2IK model the Wilson ratio is no longer universal [51].

The 2IK model was first introduced in order to study the strongly correlated heavy fermion systems [17, 18, 20, 84], containing a so-called Kondo lattice, that is an impurity in each unit cell [51]. Such a system is characterized by the following Hamiltonian:

$$H = H_0 + H_{imp} \quad (6.1)$$

6. Kondo effect in RKKY-coupled Double Quantum Dots

with H_0 the conduction electrons Hamiltonian given by:

$$H_0 = \sum_{k,\sigma} \varepsilon_k c_{k\sigma}^\dagger c_{k\sigma} \quad (6.2)$$

where $c_{(S,D)k\sigma}^\dagger$ ($c_{(S,D)k\sigma}$) are the creation (annihilator) operators, and $\varepsilon_{(S,D)k}$ the energy dispersion. The impurity Hamiltonian H_{imp} has the following form:

$$H_{imp} = J_K [S_1 \cdot \sigma(r1) + S_2 \cdot \sigma(r2)] + J_{RKKY} S_1 \cdot S_2 \quad (6.3)$$

where J_K is the Kondo coupling of the impurities to the Fermi sea, assumed to be a constant for both impurities. $S_{1,2}$ are the impurity spin operators, while $\sigma(r1, r2)$ is the local spin coupled to the impurity 1(2) located at $r1(r2)$ [18]. The last term represents the RKKY exchange interaction between the impurity spins, the coupling strength J_{RKKY} having a strong dependence on the Fermi wavevector:

$$J_{RKKY} \propto \left[\frac{\sin(2k_F r)}{(k_F r)^d} \right] \quad (6.4)$$

where k_F the Fermi wavevector, r the distance separating the impurities, and $d=1,2,3$ is the dimensionality of the system [15, 17, 85]. For $J_{RKKY} < 0$ the exchange coupling is ferromagnetic (FM), while for $J_{RKKY} > 0$ we have an anti-ferromagnetic coupling [24].

The interesting features of this model arise from the case when the impurities are coupled anti-ferromagnetic. For a weak RKKY exchange coupling compared to the Kondo coupling, each impurity is screened separately by the Fermi sea, and the system behaves as two independent Kondo impurities. On the other hand for a critical value of $J_{RKKY}/k_B T_K \approx 2.5$ a quantum phase transition takes place between the Kondo state and the new RKKY state, the impurity spins

6.1. Introduction to the Rudermann-Kittel-Kasuya-Yosida interaction

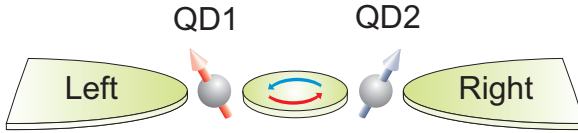


Figure 6.2.:
Schematic of two quantum dots coupled via RKKY interaction

being locked into a spin singlet, a so-called *spin-glass*. Because the total spin of the system is now 0, the Kondo screening does not take place any more [16, 24, 25, 51].

6.1.1. The exchange interaction in quantum dots

The high tunability of lateral quantum dots have made them attractive candidates for spin-based devices [5], and the rapid advancements in semiconductor nanostructure processing have only recently made possible the experimental realization of the two impurity Kondo system in semiconductor quantum dots [19, 23] (represented schematically in Fig. 6.2) or metallic quantum dots [86], previously the 2IK problem being subject only to theoretical investigations. However a conclusive understanding of the physics involved is still missing [22, 24–26, 87, 88] and more experimental data are required.

The system in Fig. 6.2 consists of two quantum dots with a well defined spin, coupled to each other via a wide open conduction region, in order to minimize the tunnel and capacitive couplings between the quantum dots. If we assume individual Kondo energy scales for each dot $T_{K1(2)}$, the system can be described by the following Hamiltonian:

$$H = H_C + J_{K1}S_1 \cdot \sigma_1 + J_{K2}S_2 \cdot \sigma_2 + J_{RKKY}S_1 \cdot S_2 \quad (6.5)$$

where H_C describes the central region between the dots, assuming a

6. Kondo effect in RKKY-coupled Double Quantum Dots

continuous density of states (DOS). Similarly to Eq. 6.2, $S_{1,2}$ are the impurity spin operators, and $\sigma(1,2)$ is the local spin in the central region coupled to QD1(2) [24]. The RKKY coupling strength J_{RKKY} has a linear dependence as a function of the Kondo couplings of the two quantum dots $J_{K1(2)}$:

$$J_{RKKY} = (v/b)J_{K1}J_{K2} \quad (6.6)$$

where v is a constant which, depending on the interference of the spin waves in the central region, can be either positive or negative, and b is the bandwidth of the central region [24].

Because the Kondo temperature is more commonly used to characterize the Kondo energy scale, it is thus more useful to have a form of the RKKY coupling as a function of the $T_{K1(2)}$. This can be obtained from Eq. 2.35 and 6.6:

$$J_{RKKY} \propto \frac{v}{b} \frac{1}{\ln(T_{K1}) \ln(T_{K2})} \quad (6.7)$$

Equation 6.7 has an asymptotic behavior for the RKKY coupling as a function of the Kondo temperatures, towards a cut-off value set by the bandwidth of the coupling region [24].

In quantum dots the RKKY-Kondo competition is manifested in the non-linear conductance, where the zero-bias anomaly disappears with increasing J_{RKKY} , and two smaller peaks will appear, at $eV_{SD} = \pm J_{RKKY}/2$, corresponding to the singlet-triplet states of the localized spins on the quantum dots [24, 25, 87, 88].

We already established that the RKKY coupling has a strong dependence on the Kondo energy scale, and in the previous chapter it was demonstrated that a nearby gate can tune the Kondo temperature of a dot (see. Fig. 5.4). Hence, by tuning the tunnel coupling between the quantum dot and the leads, the Kondo coupling J_K is also tuned,

6.1. Introduction to the Rudermann-Kittel-Kasuya-Yosida interaction

and with it the strength of the exchange interaction. Thus, we can study how the exchange interaction strength J changes as a function of the Kondo energy scale asymmetry. Since the RKKY ground state is expected to be a singlet, an in-plane magnetic field will compete with the RKKY anti-ferromagnetic coupling and could restore the Kondo resonance [24]. Furthermore, a perpendicular magnetic field induces Landau levels and edge states, and we already saw in the previous chapter that at high fields the edge states in the leads remain partially spin unpolarized, so Kondo effect can still be observed in transport [79–82]. Therefore tuning the quantum dots in the Kondo chessboard will allow the study of the exchange interaction via the edge states.

6.2. The RKKY interaction at zero magnetic field

In this chapter we present measurements on sample D040330A, represented in Fig. 6.3. As already described in Chap. 3.1.4 the device was produced by local anodic oxidation (LAO) with an AFM [66, 69, 70]. For the measurement we have used the electrical setup described in Fig. 3.14. The differential conductances $\sigma_1 = dI_1/dV_{ac}$ and $\sigma_2 = dI_2/dV_{ac}$ have been obtained using the standard lock-in technique, by applying an ac excitation of $V_{ac} = 10 \mu\text{V}$ with a frequency of 83.333 Hz at the Source and measuring the currents from the two drains. However due to the fact that the 1D constriction between the Source and the central region has a finite resistance (we estimate at least two conducting channels, corresponding to resistance of $\approx 6.5 \text{ k}\Omega$), the Source voltage is divided. The sample can be regarded as two quan-

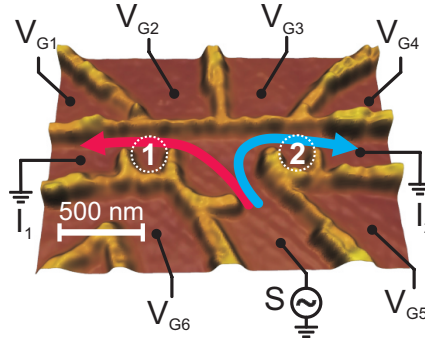


Figure 6.3.:

AFM image of sample D040330A defined by oxide lines (bright/yellow). Quantum dots, 1 and 2, are connected to a common Source S, and each to individual drains. Six in-plane gates, G1 to G6, control the potentials of the dots and coupling to the leads. The arrows mark the measured transport paths.

6.2. The RKKY interaction at zero magnetic field

tum dots connected in a parallel circuit, and in order to precisely extract the differential conductances of the dots, the voltage drop across the 1D constriction needs to be known. However the 1D constriction cannot be individually characterized, therefore the actual voltage applied to the central region will be smaller than $10 \mu\text{V}$, and for this reason the measured conductances are slightly underestimated. The serial resistance of the 1D channel also limits the maximum current, which will lead to a correlation between the two currents measured. In other words an increase in e.g. I_1 will result in a slight decrease in I_2 . The measurements were performed in a $^3\text{He}/^4\text{He}$ dilution refrigerator at a base temperature of $\approx 20\text{mK}$. From temperature dependent measurement we estimate an electron temperature of $\sim 80\text{mK}$.

6.2.1. Asymmetric Kondo coupling

The main goal of the measurements is to obtain evidence of the RKKY interaction in quantum dots, at a relatively large distance. Towards this goal, we will be using the known competition between the Kondo effect and the RKKY interaction, as it was described in the Introduction. The two quantum dots on the sample can be individually tuned using applied voltages on the in-plane gates G1 to G6. On such small length scales a voltage applied on any gate affects the quantum dots energy levels and potentials, even if the gate is not nearby. In these measurements we vary the voltages on gates G2 and G3 to control the coupling of the two dots to the central region, while G5 and G6 are used as plunger gates. The voltages on gate G1 and G4 are kept fixed. In Fig. 6.4 are shown the Kondo resonances exhibited by QD1 (a)-(c), respectively QD2 (b)-(d) in the non-linear dependence. We have made sure in this case that when measuring the Kondo resonance of one dot, the other to be tuned to the next non-Kondo valley. The quantum dots are strongly coupled to the leads, seen from Fig. 6.4 (a) and (b)

6. Kondo effect in RKKY-coupled Double Quantum Dots

where the Coulomb diamond lines are very broad. We extract a charging energy of ≈ 0.25 meV for QD1, ≈ 0.3 meV for QD2. Fitting the Kondo resonance from Fig. 6.4 (c) and (d) to obtain the HWHM, reveals highly asymmetric Kondo energy scales, with $T_{K1} \simeq 720$ mK and $T_{K2} \simeq 280$ mK. The temperature dependent measurements (shown in the insets of Fig. 6.4 (c) and (d)) show the logarithmic conductance decrease, identified as the Kondo effect fingerprint.

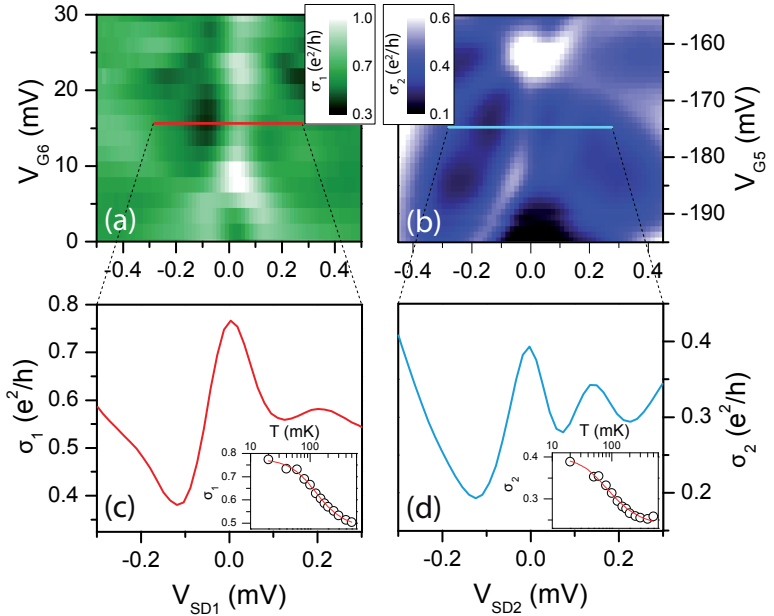


Figure 6.4.:

(a) Differential conductance σ_1 and (b) σ_2 showing the zero-bias anomaly through QD1, respectively QD2. (c) Cut along the solid red line in (a) showing the QD1 ZBA and its temperature dependence (inset). (d) Cut along the solid blue line in (b) showing the QD2 ZBA and its temperature dependence (inset).

6.2. The RKKY interaction at zero magnetic field

When we tune both quantum dots in the middle of the Kondo valley, we observe in QD1 a suppression of the Kondo resonance (solid line in Fig. 6.5 (a)) compared to the non-interacting case. In QD2 a more dramatic change is obtained (Fig. 6.5 (b)): while the initial Kondo resonance (dashed line) is no longer visible, we can clearly distinguish two shoulders located symmetrically around $\pm 100 \mu\text{eV}$. We interpret the appearance of the shoulders as a result of the competition between the RKKY interaction with the Kondo effect in the two quantum dots. The difference between the maximum conductance of each shoulder is due to the tunnel barrier asymmetry between the Source and Drain 2 contacts.

The color plot of the differential conductance σ_2 through QD2 as a function of bias voltage and gate $G5$ (Fig. 6.6) shows the behavior of the QD2 ZBA when QD1 is tuned in the middle of the Kondo valley

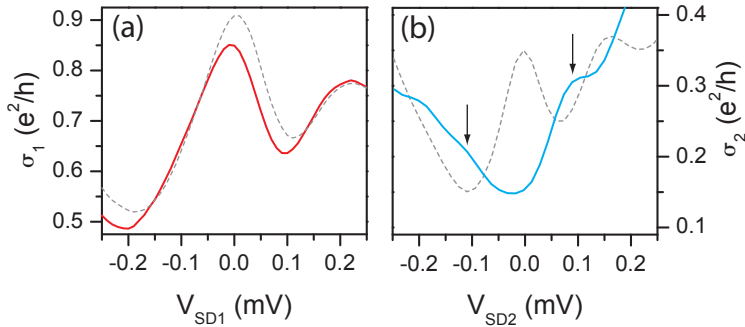


Figure 6.5.:

Kondo resonances with exchange interaction. Full lines correspond to QDs tuned in the middle of the Kondo valley at the same time, while dashed lines mark the non-interacting situation. (a) A slightly suppressed QD1 ZBA (full line). (b) Corresponding situation in QD2 - splitting of ZBA. The arrows mark the position of the split Kondo resonance.

6. Kondo effect in RKKY-coupled Double Quantum Dots

for $V_{G2} = -54$ mV. From $V_{G5} \cong -175$ mV the ZBA starts to deviate to the right along with a decrease in conductance, which suggests the beginning of a splitting. The smooth change in the maximum conductance of the peak is consistent with the expected cross-over between the Kondo and the RKKY ground states. At $V_{G5} \simeq -167$ mV beside the main peak located now at $\sim +75 \mu\text{V}$ bias, a shoulder emerges at $\sim -70 \mu\text{V}$ (their positions are marked in Fig. 6.6 by two dots and arrows). The deviation of the main Kondo peak toward positive bias, followed by the emergence of a secondary bias-symmetric peak is interpreted in terms of tunnel coupling asymmetry, QD2 being stronger coupled to the central region. Since the RKKY interaction has an effect similar to a local magnetic field [24], the ZBA behavior in Fig. 6.6 is analog to that of the Kondo resonance in parallel magnetic field. In e.g. Fig. 5.5 due to a similar tunnel coupling asymmetry the split Kondo resonance is visible only for fields higher than 1.5 T ($E_B \approx 40 \mu\text{eV}$).

By adjusting V_{G2} between -42 mV to -56 mV the coupling of QD1 to the central region is tuned, resulting in a different Kondo coupling, i.e. a different Kondo temperature (Fig. 6.7 (a)). A measurement of the corresponding situation in QD2 (Fig. 6.7 (b)) allows us to extract the magnitude of the splitting as a function of T_{K1} (Fig. 6.7 (d)). The splitting of the Kondo resonance gives direct access to the exchange interaction strength J_{RKKY} using the relation $eV_{SD} = \pm J_{RKKY}/2$ (black arrows in Fig. 6.5 (b)) [24, 87, 88] and the obtained values range from about 200 to 130 μeV . The analytical relation of the RKKY exchange coupling as a function of the Kondo temperature (Eq. 6.7) has an asymptotic behavior, and the data in Fig. 6.7 (c) is fitted to $J = a + b/\ln(T_{K1})$ (line in Fig. 6.7 (c)). The obtained fit parameters are $a \sim 1.2$ meV and $b \sim -6.5$ meV, where a is extracted as the maximum bandwidth of the central region [24], while b contains information about the density of states in the leads. The zero-bias conductance of QD2 has a similar behavior and can be fitted with a

6.2. The RKKY interaction at zero magnetic field

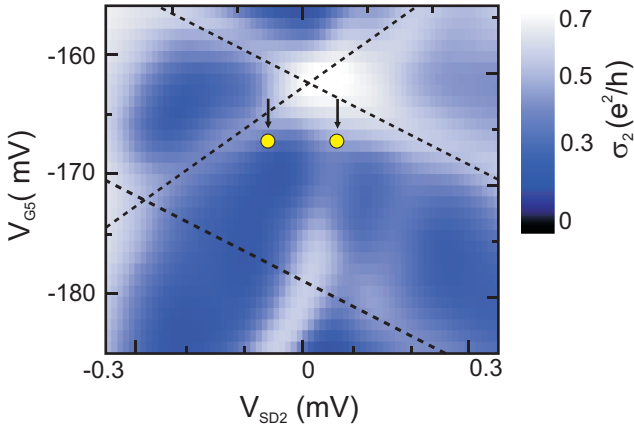


Figure 6.6.:

Color scale plot of the QD2 differential conductance σ_2 as a function of gate G5 and bias voltage, showing the splitting of the QD2 ZBA. (Dot+arrow mark the splitting).

$c + d \ln(T_{K1})$ function, analog to the change in the splitting magnitude, with $c = 1.86$ and $d = -0.26$ (Fig. 6.7 (d)).

However the splitting of the Kondo resonance is observed only in QD2, while in QD1 we see just a suppression of the Kondo resonance. As it was discussed in the introduction, the transition from the Kondo state to the RKKY bound state happens through a quantum phase transition at zero temperature, or a cross-over region at finite temperatures. This type of transition describes a change in the ground state of the entire many-body system due to quantum fluctuations [89]. Thus the RKKY coupling effect should be observed in both quantum dots with the same magnitude, since it now describes the new ground state of the coupled quantum dots system. At e.g. $V_{G2} = -42$ mV we measure a $J_{RKKY} \simeq 200 \mu\text{eV}$ in the splitting of the QD2 ZBA, for a

6. Kondo effect in RKKY-coupled Double Quantum Dots

$T_{K1} \simeq 720$ mK, or $\approx 60 \mu\text{eV}$, so the RKKY interaction should be large enough to induce a splitting of the QD1 ZBA as well. The decrease of the QD1 Kondo resonance (as seen in Fig. 6.6 (a)) indeed indicates that there is a competing interaction taking place, although on a much lower scale than expected.

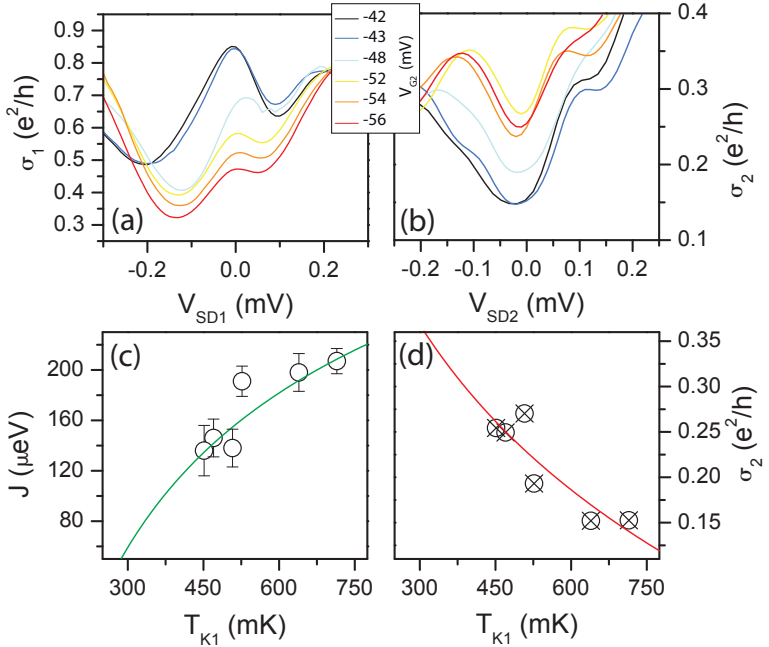


Figure 6.7.:

(a) Conductance σ_1 through QD1 showing a zero-bias anomaly for different voltages on G2. (b) The split QD2 ZBA corresponding to the traces in (a). (c) Exchange interaction strength J_{RKKY} as a function of T_{K1} , fitted to $1/\ln(x)$. (d) Zero-bias QD2 conductance σ_2 (taken from (b)) as a function of T_{K1} , with a $\ln(x)$ fit. (line).

6.2. The RKKY interaction at zero magnetic field

In a similar setup [19] the splitting of the Kondo resonance has been also explained in terms of a Fano antiresonance [26]. Fano resonances are the result of interference between a resonant scattering channel and a non-resonant contribution. In the case of a quantum dot, this happens when the wave function of incident electrons is split into two parts when tunneling into the dot, one for each transport channel. The two channels will interfere at the exit of the quantum dot, so the scattered wave function is the result of a two-channel transmission [77]. Depending on the phase shift between the two channels, the interference can be either constructive, resulting in a Fano resonance, or destructive resulting in an anti-resonance. The Fano regime is characterized by strong coupling to the leads, as is the case for our measurements. However, while the description of the ZBA splitting in terms of a Fano antiresonance is suitable for high interdot hopping and the explanation in terms of RKKY is more appropriate in the limit of strongly localized electrons, in between the two effects can coexist [90]. Therefore, because our measurements suggests the presence of both effects, we could attribute the QD1 ZBA decrease and QD2 ZBA splitting to an RKKY coupling, while the magnitude of the QD2 ZBA splitting is enhanced by a Fano antiresonance.

6.2.2. Symmetric Kondo coupling

In a different cooling cycle the previous section, the situation is quite different when the Kondo energy scales of the quantum dots are tuned in a more symmetric state. In Fig. 6.8 are shown the Kondo resonances of the two quantum dots. The measurements have been performed in a different cooling cycle than the ones presented in the previous section. The gate voltages applied to the sample in this case are: $V_{G1} = -150$ mV, $V_{G2} = -140$ mV, $V_{G3} = -100$ mV, $V_{G4} = 0$ mV which are kept fixed throughout the measurements. Only V_{G6} and V_{G5}

6. Kondo effect in RKKY-coupled Double Quantum Dots

are used as plunger gates to change the electron number in the two dots. We extract the Kondo temperatures again using the Eq. 2.42 with the following values $T_{K1} \simeq 300$ mK and $T_{K2} \simeq 260$ mK obtained in the middle of the Kondo valleys (Fig. 6.8 (c) and (d)).

In this case we do not observe a splitting of the Kondo resonances in either of the quantum dots. To better understand what happens we perform the following type of measurement: while keeping one quan-

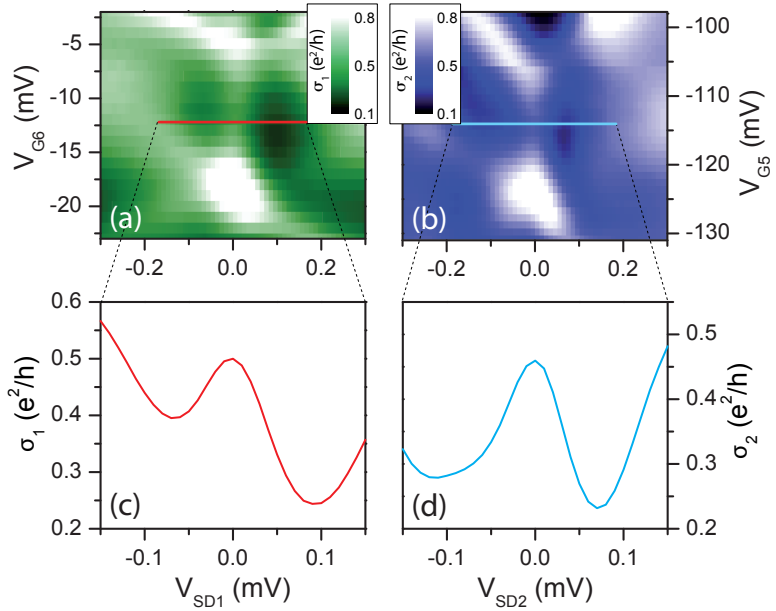


Figure 6.8.:

(a) Differential conductance σ_1 and (b) σ_2 showing the zero-bias anomaly through QD1, respectively QD2. (c) Cut along the solid red line in (a) showing the QD1 ZBA. (d) Cut along the solid blue line in (b) showing the QD2 ZBA.

6.2. The RKKY interaction at zero magnetic field

tum dot fixed in the middle of its Kondo valley, we sweep the plunger gate voltage on the other dot in order to tune it from a non-Kondo to a Kondo valley and vice-versa. In Fig. 6.9 it is shown such a measurement, of the QD1 ZBA from Fig. 6.8 (c) as a function of QD2 plunger gate. In Fig. 6.9 (a) we've plotted the differential conductance of QD1 as a function of the bias voltage V_{SD1} on the vertical scale, and the QD2 plunger gate V_{G5} on the horizontal scale. In Fig. 6.9 (b) is shown, on the one hand, the conductance through QD2 with two Coulomb peaks visible (blue dashed line), marking the transition from $M-1$ to M to $M+1$ electrons, with the Kondo valley highlighted in grey. On the other hand there is the QD1 Kondo resonance peak conductance taken along the zero-bias line in the upper plot. The only noticeable characteristic of the measurement is the expected smooth change in the QD1 Kondo peak conductance, correlated up to a certain degree with the conductance through the other dot, the current through the quantum dots being limited by the 1D constriction.

A similar measurement is performed on QD2, shown in Fig. 6.10. The figure layout is analog to the one in Fig. 6.9, that is in the upper part (Fig. 6.10 (a)) we've plotted the differential conductance σ_2 , showing the QD2 ZBA from Fig. 6.8 (d), as a function of the bias voltage V_{SD2} on the vertical scale, and the QD1 plunger gate V_{G6} on the horizontal scale. The lower plot (Fig. 6.10 (b)) contains the QD2 Kondo peak conductance (blue solid line) along with the QD1 conductance showing the electron number transition (red dashed line) from $N-1$ to N to $N+1$. Unlike the QD1 situation, here we observe a remarkable feature in the QD2 conductance. While QD1 is in the Kondo valley (greyed area in Fig. 6.10 (b)) an abrupt increase in the QD2 peak Kondo conductance happens for $V_{G6} \simeq 13$ mV. Up to $V_{G6} \simeq 7$ mV the conductance remains roughly constant, then it suddenly drops. This feature is visible even in the conductance intensity plot in Fig. 6.10 (a) in the same gate voltage range.

6. Kondo effect in RKKY-coupled Double Quantum Dots

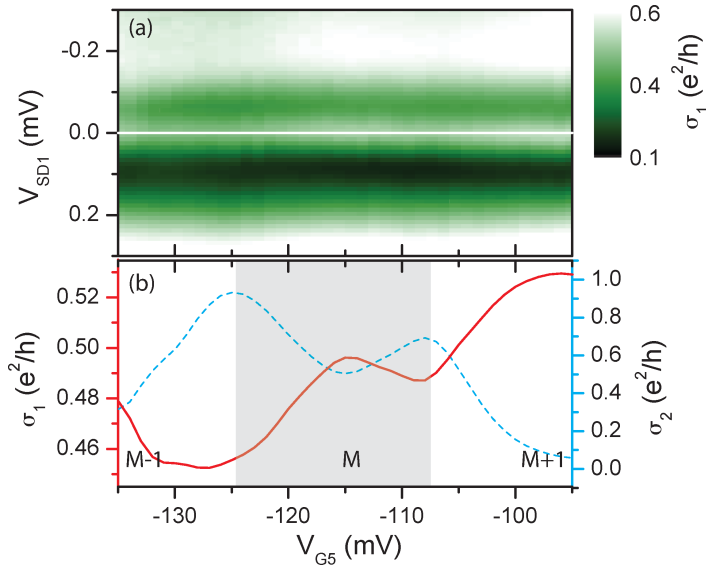


Figure 6.9.:

QD1 Kondo resonance as a function of QD2 electron number. (a) Intensity color plot of σ_1 showing the QD1 ZBA at $V_{G6} \simeq -12$ mV, as a function of V_{SD1} and the plunger gate of QD2, V_{G5} . (b) (solid line) QD1 Kondo peak conductance taken along the zero-bias line in (a). Dashed line shows the electron number changes from M-1 to M+1 in QD2, marked by the Coulomb peaks, with the Kondo valley highlighted in grey.

To better understand the exchange interaction in the aforementioned cases we analyze the Kondo resonance of both dots in a situation when a Kondo-RKKY competition is expected, i.e. both dots in the Kondo valley, and compare it with the situation when only one dot exhibits a Kondo resonance. For QD1 we compare the Kondo reso-

6.2. The RKKY interaction at zero magnetic field

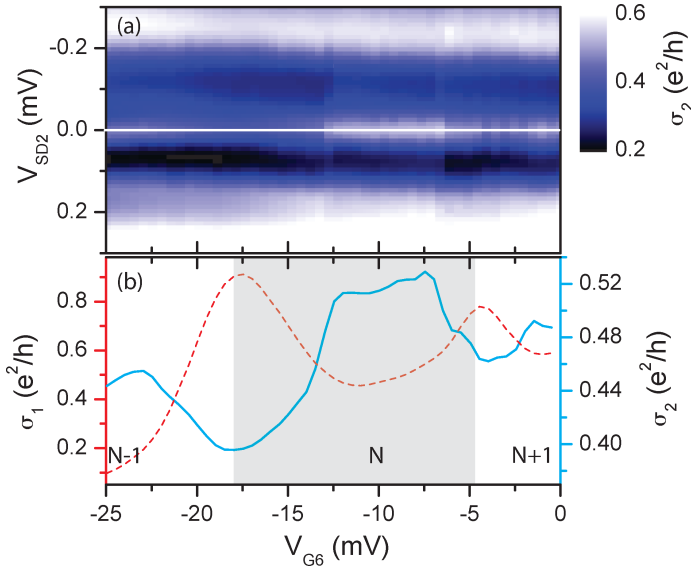


Figure 6.10.:

QD2 Kondo resonance as a function of QD1 plunger gate. (a) Intensity color plot of σ_2 showing the QD2 ZBA at $V_{G5} \simeq -115$ mV, as a function of V_{SD2} and the QD1 plunger gate V_{G6} . (b) Kondo peak conductance taken along the zero-bias line in (a). Dashed line shows the electron number changes from $N-1$ to $N+1$ in QD1, marked by the Coulomb peaks, with the Kondo valley highlighted in grey.

nance width (Fig. 6.11 (a)) and temperature dependence (Fig. 6.11 (c)) for $V_{G5} = -90$ mV (QD2 electron number is $M+1$) and for $V_{G5} = -115$ mV (QD2 electron number is M =Kondo state)¹. The Kondo temperatures extracted from the resonance widths are $T_{K1} = 270$ mK for $V_{G5} = -90$ mV and $T_{K1}^* = 250$ mK for $V_{G5} = -115$ mV. In the

¹Gate voltages correspond to Fig. 6.9

6. Kondo effect in RKKY-coupled Double Quantum Dots

temperature dependence the difference is almost not visible, but it qualitatively supports the lower Kondo temperature for $V_{G5} = -115$ mV obtained from the HWHM.

In the case of QD2 we compare similarly the Kondo resonance width (Fig. 6.11 (b)) and temperature dependence (Fig. 6.11 (d)) for $V_{G6} = -25$ mV (QD1 electron number is N-1) and for $V_{G6} =$

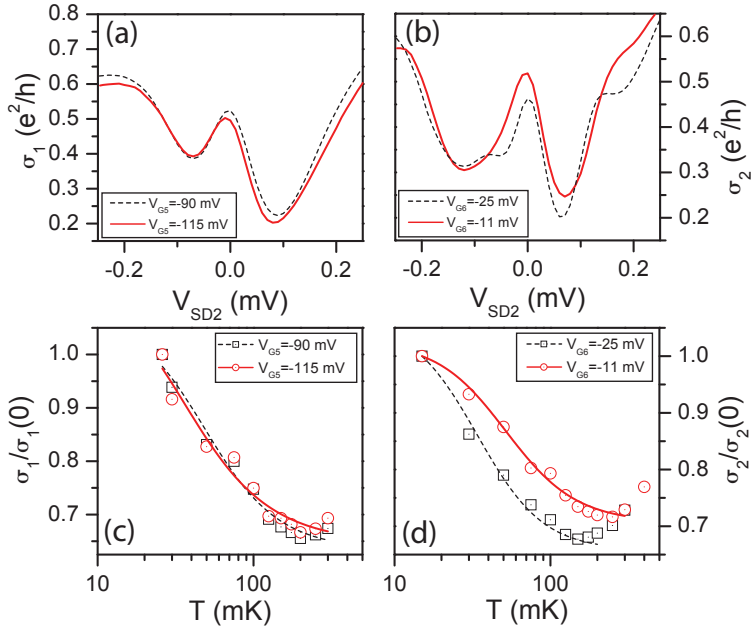


Figure 6.11.:

(a) QD1 ZBA when QD2 is tuned in the Kondo valley (solid) or non-Kondo valley (dashed). (b) QD2 ZBA when QD1 is tuned in the Kondo valley (solid) or non-Kondo valley (dashed). (c) Normalized temperature dependence of QD1 for the corresponding situations in (a). (d) Normalized temperature dependence of QD2 for the corresponding situations in (b).

6.2. The RKKY interaction at zero magnetic field

-11 mV (QD2 electron number is $N=Kondo$ state)². We extract a $T_{K2} = 180$ mK for $V_{G6} = -25$ mV and $T_{K2}^* = 280$ mK for $V_{G6} = -11$ mV, difference visible also in the normalized temperature dependence in Fig. 6.11 (d).

While the results obtained for QD1 are consistent with our expectations in the case of a very weak RKKY coupling - which would decrease the Kondo energy scale -, the jump and drop in the Kondo conductance of QD2 is altogether atypical. Generally it is expected that confinement effects could influence the RKKY coupling [91]. In a hypothetical picture, in samples with a rough potential, as for example the ones created by AFM lithography, the RKKY coupling function could present additional features induced by the potential landscape in the coupling region. Since gate G6 is coupled to the central region and controls to a certain extent the electron density, a dip in the RKKY density of states could be accessed by varying the gate voltage, which would locally decrease the exchange interaction strength allowing an increase in the Kondo conductance. The fact that the Kondo conductance drops sharply again at a lower voltage on G6 fits with this hypothetical picture. In the following section the investigations are further extended by applying an in-plane magnetic field.

²Gate voltages correspond to Fig. 6.10

6.3. Exchange interaction in parallel magnetic field

The split ZBA behavior in magnetic field depends on the sign of the RKKY coupling, and it is an important tool to determine whether J_{RKKY} is anti-ferromagnetic (AF) or ferromagnetic (FM). It was predicted by Simon *et al.* [24] that in the case of an AF RKKY coupling ($J_{RKKY} > 0$), i.e. singlet ground state, an in-plane magnetic field will align the spins of the two impurities into a triplet state, thus destroying the RKKY coupling and restoring the Kondo ground state in each quantum dot at $g^* \mu_B B = J_{RKKY}$ (see the cartoon in Fig. 6.12). In the following we present measurements in a magnetic field applied parallel to the 2DEG, with the quantum dots in the same state as in Section 6.2.2.

In Fig. 6.13 the contour plots of the differential conductances of QD1 and QD2 are shown, when only one dot shows a Kondo resonance (Fig. 6.13 (a) and (c)), thus no competing interaction is ex-

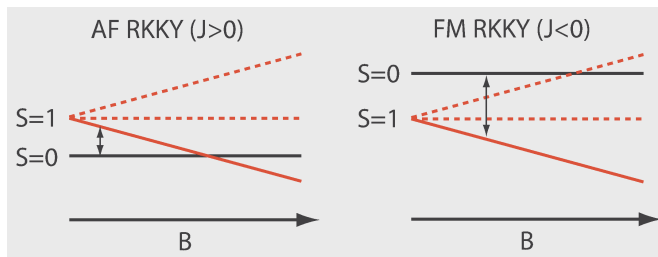


Figure 6.12.:

Magnetic field dependence of the split Kondo resonance. For an anti-ferromagnetic (AF) RKKY interaction the singlet-triplet transition energy (marked by an arrow) decreases, while for a ferromagnetic (FM) interaction it increases with magnetic field.

6.3. Exchange interaction in parallel magnetic field

pected, as well as when both dots are tuned in the Kondo valley at the same time (Fig. 6.13 (b) and (d)). To better observe and compare the behavior in both interacting and non-interacting cases, the conductance matrices are normalized to the $B = 0$ T/ $V_{SD} = 0$ mV value. Quantum Dot 1 (Fig. 6.13 (a) and (b)) shows roughly the same behavior in both cases, with the parallel field induced ZBA splitting observable only from 1.8 T. Quantum Dot 2 in the non-interacting case (Fig. 6.13 (c)) shows the expected behavior, with a Zeeman split zero-bias anomaly clearly visible in the trace cuts in Fig. 6.13 (e). On the other hand, in the interacting case (Fig. 6.13 (d)) we can see a slight increase, evidenced in the color intensity, followed by a Zeeman splitting of the Kondo resonance. A comparison between the trace cuts at $B=2$ T in Fig. 6.13 (e) and (f) shows a smaller splitting for $V_{G6} = -11$ mV, when both dots are tuned in Kondo regime. That is $\Delta E_Z \approx 62 \mu\text{eV}$ for $V_{G6} = -25$ mV (Fig. 6.13 (e)) and $\Delta E_Z^* \approx 56 \mu\text{eV}$ for $V_{G6} = -11$ mV (Fig. 6.13 (f)). In the trace cut at $B=1$ T, although here the secondary Kondo peak is not yet visible, it can be seen a larger deviation of the Kondo peak towards negative bias for $V_{G6} = -25$ mV, consistent with the different splitting values at 2 T.

One can also compare the zero-bias traces for both the interacting and non-interacting cases, taken from the measurements presented in Fig. 6.13. In Fig. 6.14 (a) we have plotted the zero-bias conductance of QD1 as a function of magnetic field when QD2 is tuned in a non-Kondo state (black line - $V_{G5} = -90$ mV), along with the situation when QD2 is in a Kondo state (red-line - $V_{G5} = -115$ mV). Although both traces show a monotonic decrease with magnetic field, the trace for $V_{G5} = -115$ mV, corresponding to the interacting case, has a slightly lower field dependence. This already indicates a difference in the ground state, as predicted by theory [24, 25, 87, 88], from a singlet to a triplet state. However a clear transition point cannot be extracted

6. Kondo effect in RKKY-coupled Double Quantum Dots

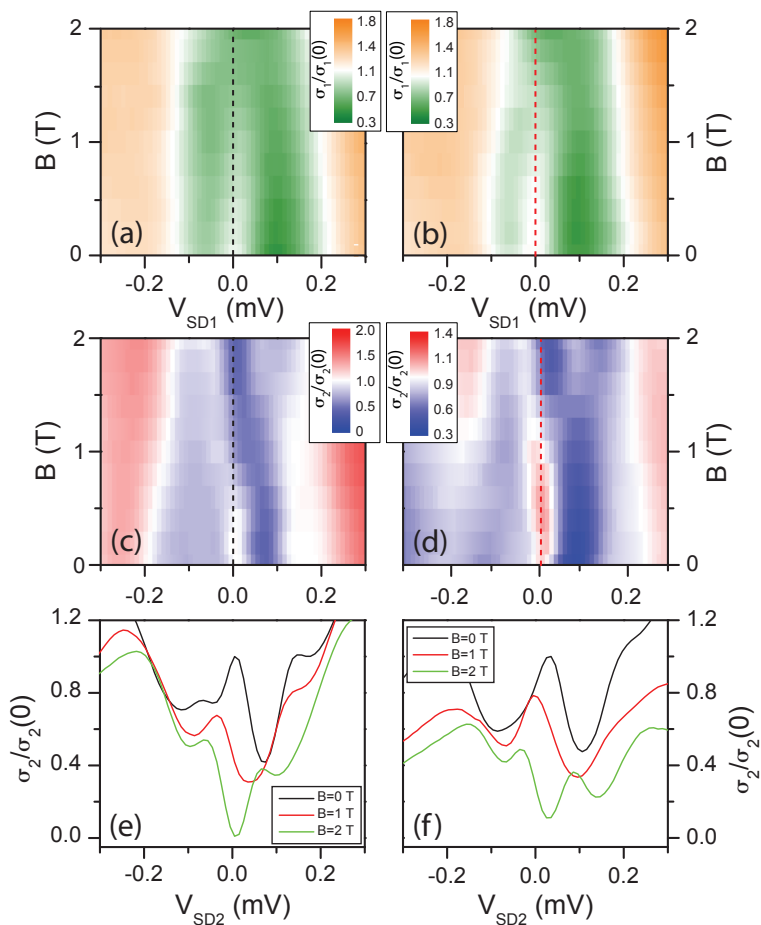


Figure 6.13.:

(a)-(b) QD1 normalized conductance as a function of V_{SD1} and in-plane magnetic field for (a) $V_{G5} = -90$ mV and (c) $V_{G5} = -115$ mV. (c)-(d) QD2 normalized conductance as a function of V_{SD2} and in-plane magnetic field for (b) $V_{G6} = -25$ mV and (d) $V_{G6} = -11$ mV. (e)-(f) QD2 trace cuts for $B=0, 1, 2$ T in (c), and (d) respectively. The traces are offset for clarity with $0.2 \sigma_2/\sigma_2(0)$.

6.3. Exchange interaction in parallel magnetic field

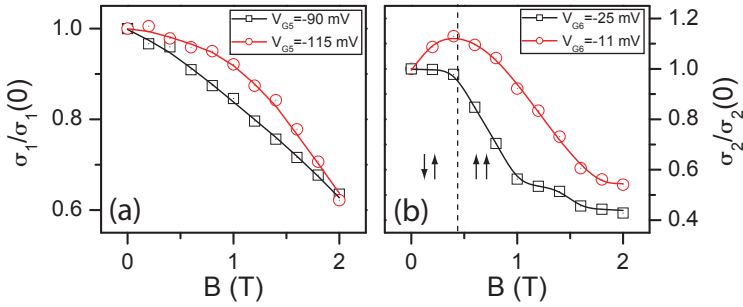


Figure 6.14.:

(a) Normalized differential conductance σ_1 as a function of in-plane magnetic field for $V_{G5} = -90$ mV (QD2 not in Kondo regime) and $V_{G5} = -115$ mV (QD2 in Kondo regime), corresponding to traces in Fig. 6.13 (a) and (c). (b) Normalized differential conductance σ_2 as a function of in-plane magnetic field for $V_{G6} = -25$ mV (QD1 not in Kondo regime) and $V_{G6} = -11$ mV (QD1 in Kondo regime), corresponding to traces in Fig. 6.13 (b) and (d).

from this data.

The situation is more straight forward to interpret when looking at the data from QD2 (Fig. 6.14 (b)). While the trace cut for $V_{G6} = -25$ mV (black line) shows a monotonic decrease from $B \approx 0.3$ T upwards³, in the interacting case ($V_{G6} = -11$ mV - red line) there is a clear increase with magnetic field up to $B \approx 0.45$ T, followed by a monotonic decrease.

The peak in the QD2 conductance marks the Singlet-Triplet transition point, and from its value $B \approx 0.45$ T we estimate a RKKY exchange coupling $J_{RKKY} = g^* \mu_B B = 12 \mu\text{eV}$, with the bulk GaAs value for the electron Landé factor $g^* = 0.44$. In temperature units the value is very similar to, although smaller than, the Kondo temper-

³see Chapter 5.1.2 for a better description

6. Kondo effect in RKKY-coupled Double Quantum Dots

atures, i.e. $J_{RKKY}/k_B \approx 140$ mK, suggesting that the quantum dots are tuned very close to the critical point of the quantum phase transition. This critical point is given by $(J_{RKKY}/E_K^*)_c = 8/\pi \simeq 2.54$ assuming the same Kondo energy scale for both dots, i.e. $T_{K1} = T_{K2} = E_K^*/k_B$, while for different Kondo scales it can be calculated using the following relation [24]:

$$(J_{RKKY})_c = \frac{4}{\pi} (T_{K1} + T_{K2}) k_B \quad (6.8)$$

Using the Kondo temperature values extracted earlier, that is $T_{K1} \approx 270$ mK and $T_{K1} \approx 180$ mK we obtain a critical transition value $(J_{RKKY})_c \approx 48 \mu\text{eV}$ or 560 mK, a factor of 3.4 larger than the value extracted from the parallel field dependence of QD2 (Fig. 6.14 (b)). However this relation does not take into account the distance between the magnetic moments, and in a two dimensional system the RKKY interaction strength has a $1/k_F r^2$ dependence.

6.4. The RKKY interaction in perpendicular magnetic field

We have seen in Chapter 5.1.3 that in perpendicular magnetic field, due to the formation of Landau levels and the charge polarization inside the quantum dot, Kondo effect is exhibited in a very regular pattern of high-low differential conductance, generally referred to as the Kondo chessboard [79–83].

In Fig. 6.15 (a) there is shown the expected Kondo chessboard pattern exhibited by QD1, with alternating regions of high (bright) and low (dark) differential conductance as a function of the voltage applied on G6 and magnetic field. In contrast, QD2 exhibits a more complicated pattern for the same magnetic field polarity (Fig. 6.15 (b)). By changing the direction of the magnetic field the situation is reversed. Now we observe a regular chessboard pattern in the transport through QD2 (Fig. 6.15 (d)) - gate G6 being the plunger gate of QD1, and further away, it has a much smaller lever arm on QD2, therefore here the total electron number remains unchanged, and one sees only a modulation of the conductance by the magnetic field. At the same time QD1 (Fig. 6.15 (c)) exhibits a pattern similar to the one in Fig. 6.15 (b). The data presented in Fig. 6.15 (a) and (b), respectively (c) and (d), are acquired in parallel, in the same range of V_{G6} and B-field, so the differences arise only from changing the polarity of the perpendicular magnetic field. The magnetic field does in fact change the direction of electron transport in the edge states formed in the central region between the dots. An analysis of the Kondo tile periodicity using Eq. 5.2 (as described in the Chapter 5.1.3) yields between 10 to 20 electrons contained in QD1, estimated from Fig. 6.15 (a), while for QD2 between 15 and 25 electrons are estimated from Fig. 6.15 (d).

In the first case (Fig. 6.15 (a) and (b)), the edge state picture corresponds to the one depicted in Fig. 6.15 (e), that is the edge state trans-

6. Kondo effect in RKKY-coupled Double Quantum Dots

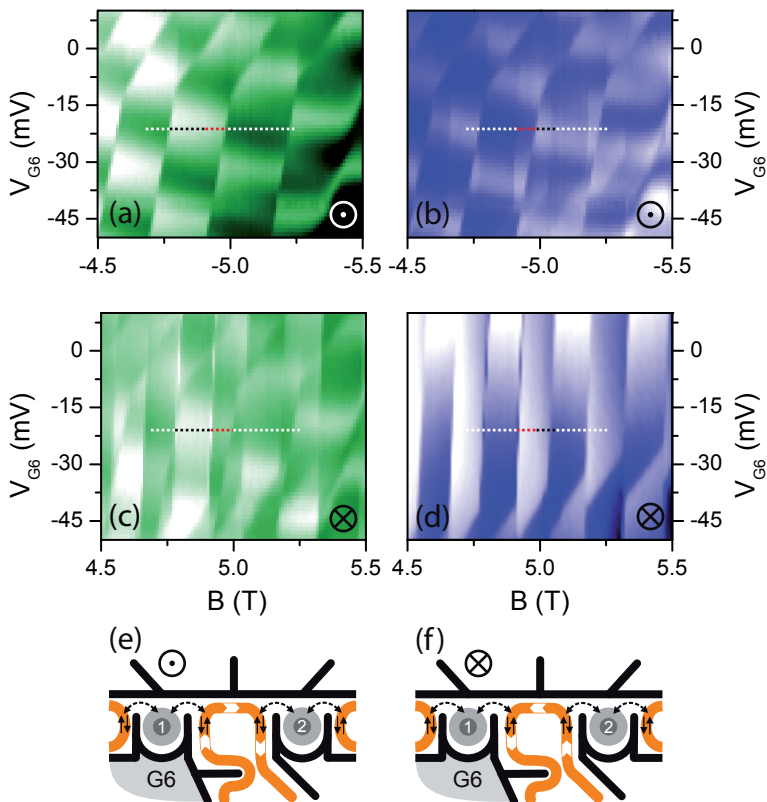


Figure 6.15.:

Differential conductance σ_1 through QD1 as a function of V_{G6} and magnetic field, for negative (a) and positive (c) magnetic field polarity. Differential conductance σ_2 through QD2 as a function of V_{G6} and B measured for negative (b), and positive (d) magnetic field polarity, measured simultaneously with (a), and (c) respectively. (e)-(f) Schematic diagram of the sample in magnetic field: with black - AFM oxide lines, orange - edge states. Landau Level 1 (dark grey) and Landau level 0 (light grey) are marked in the QDs.

6.4. The RKKY interaction in perpendicular magnetic field

port direction is clockwise in the central region, therefore transport through QD2 will be sensitive to potential changes in the edge states generated by electron transport through QD1, i.e. the sample will behave as a current divider. As a consequence QD2 will exhibit a combination of its own chessboard pattern and a negative of the QD1 pattern (Fig. 6.15 (b)). In the second situation (Fig. 6.15 (c) and (d)) the edge state transport direction is reversed - as depicted in Fig. 6.15 (f), i.e. the electrons move counter-clockwise in the edge states in the central region. Hence, now QD1 will exhibit a combination of both chessboard patterns (Fig. 6.15 (d)).

These measurements in Fig. 6.15(a)-(d) demonstrate a chiral coupling between the quantum dots via the edge states formed in the central region. Using these conductance plots one can identify the regions where only one or both quantum dots exhibit transport through a Kondo state and compare the two situations.

Along the dashed lines in Fig. 6.15 (a) and (c) is marked such a situation for the transport through QD1. Between ± 4.77 T and ± 4.97 T (black+red part on the dashed line in Fig. 6.15 (a) and (c)) QD1 exhibits transport through a Kondo state. In the ± 4.92 T to ± 5.05 T interval QD2 also exhibits Kondo transport, visible in Fig. 6.15 (d), therefore from ± 4.92 T to ± 4.97 T both quantum dots are in the Kondo regime (red part on the dashed lines). A similar situation is identified in the case of QD2 for the same gate voltage, indicated by the dashed lines in Fig. 6.15 (b) and (d). As previously mentioned, in the ± 4.92 T to ± 5.05 T interval QD2 also exhibits Kondo transport (black+red part on the dashed line in Fig. 6.15 (b) and (d)), which overlaps with the ± 4.77 T to ± 4.97 T interval, in which QD1 is in a Kondo state, between ± 4.92 T to ± 4.97 T (marked as the red part on the dashed lines).

6.4.1. Temperature dependence

We first probe the exchange interaction between the two quantum dots in perpendicular magnetic field by analyzing the temperature dependence of both quantum dots, taken along the dashed lines in Fig. 6.15. In Fig. 6.16 (a) the sharp steps in the differential conductance at -4.77 and -4.97 T mark the onset of Kondo effect in QD1. It can be observed that the monotonous decrease in the Kondo conductance changes around -4.9 T, suggesting the presence of a second energy scale. This feature becomes more obvious as the temperature is increased. For the opposite polarity (Fig. 6.16 (b)), due to the change in the edge state chirality, an extra step in the conductance of QD1 marks the onset of Kondo effect in QD2 at ~ 4.9 T.

In Fig. 6.16 (c) and (d) are shown two data sets taken from 6.16 (a), and (b) respectively. For a better comparison, the conductance is normalized to the lowest temperature value. The magnetic field positions for each case corresponds to the region when only QD1 is in Kondo regime (± 4.85 T), as well as for the overlapping with the Kondo region in QD2 (± 4.96 T). One can observe that the two data sets for ± 4.85 T and ± 4.96 T have a different temperature behavior, which qualitatively is not affected by the change in the chirality of the edge states. The data is fitted using Eq. 2.43 and the obtained fit parameters are shown in the figures along with the calculated fit functions (solid lines in Fig. 6.16 (c) and (d)). Although for the opposite magnetic field directions we obtain different fit values, in both cases there is a clear enhancement of the Kondo temperature found for the case when the Kondo regions of both quantum dots are overlapping (i.e. ± 4.96 T).

Performing the same fit procedure using the Eq. 2.43 for each data set within the ± 4.77 T to ± 4.97 T interval, yields the change in T_{K1} with magnetic field (Fig. 6.16 (e) and 6.16 (f)). From ± 4.7 T up to

6.4. The RKKY interaction in perpendicular magnetic field

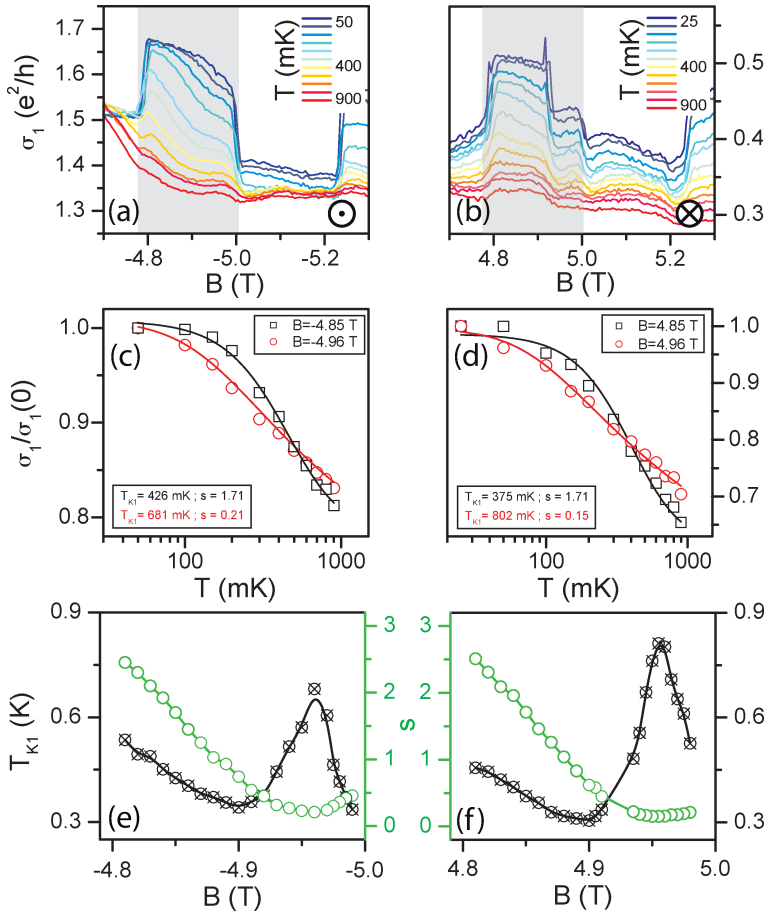


Figure 6.16.:

Temperature dependence of QD1 for negative (a) and positive (b) magnetic field polarity, taken along the white dashed lines in Fig. 6.15 (a), and 6.15 (c) respectively. (c)-(d) Normalized conductance and fit for ± 4.85 T when only QD1 exhibits Kondo effect, and ± 4.96 T for QD1-QD2 overlapping Kondo regions. T_{K1} (\otimes) versus magnetic field for negative (c), and positive (d) polarity; with green(\circ) the s fitting parameter.

6. Kondo effect in RKKY-coupled Double Quantum Dots

approximately ± 4.9 T, T_{K1} shows a monotonic decrease, which is followed by an increase up to $\sim \pm 4.95$ T, then it decreases rapidly. The position where T_{K1} starts to increase coincides with the onset of Kondo effect in QD2. As before, the fitting procedure is done with the s parameter left free and the obtained values are shown along with T_{K1} in Fig. 6.16 (e) and (f).

We perform a similar analysis for the temperature dependence of QD2. In Fig. 6.17 (b) the sharp steps in the differential conductance at 4.92 T and 5.05 T mark the onset of Kondo effect in QD2. For the opposite polarity (Fig. 6.17 (a)), due to the change in the edge state chirality, an extra conductance step at -4.97 T corresponds to the onset of Kondo effect in QD1. In both cases the background shows a strong temperature dependence. While for the data in Fig. 6.17 (b), the background is subtracted as discussed in Chapter 5.1.3 (see also Fig. C.3 in Appendix C), for the negative magnetic field polarity (Fig. 6.17 (a)) the background cannot be well estimated due to its highly non-monotonic behavior. However, by passing the data through a convolution filter we can extract the height of the conductance steps with respect to the background at the onset of Kondo in QD2, i.e. at -4.92 T and -5.05 T (marked by dashed lines in Fig. 6.17 (a)). By performing this operation for each temperature trace, we obtain the temperature dependence at the aforementioned conductance steps that mark the onset of Kondo effect in QD2, shown here in Fig. 6.17 (c) normalized to the low temperature value. While the temperature dependence at -5.05 T exhibits the expected logarithmic decrease with temperature, the data at -4.92 T first increases with temperature, then it decreases. The obvious qualitative difference between the temperature behavior of the two conductance steps, again indicates that when the Kondo regions in both dots are overlapping the system is characterized by a different ground state. In Fig. 6.17 (d) are shown the temperature dependence of the normalized conductance along with fits for 4.95 and 5.01 T for comparison.

6.4. The RKKY interaction in perpendicular magnetic field

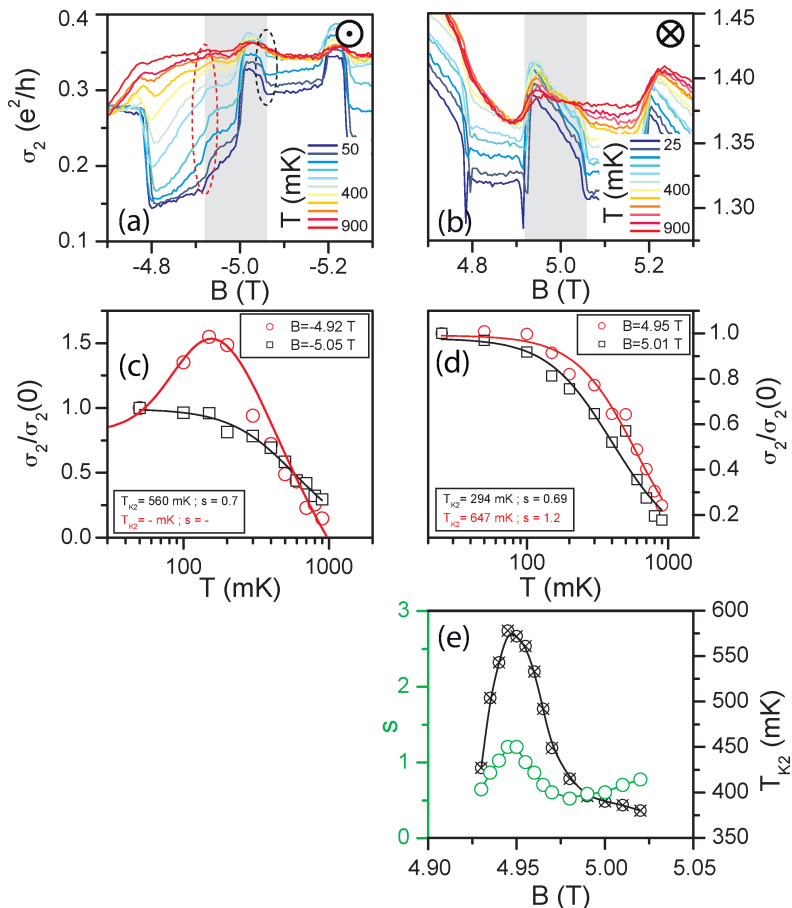


Figure 6.17.:

Temperature dependence of QD2 for negative (a) and positive (b) magnetic field polarity, taken along the white dashed lines in Fig. 6.15 (b), and 6.15 (d) respectively. (c-d) Normalized conductance with respect to the background for the case when only QD2 exhibits Kondo effect (black) and for QD1-QD2 overlapping Kondo regions (red). (e) T_{K2} (⊗) versus magnetic field for positive polarity, along with the s fitting parameter (○).

6. Kondo effect in RKKY-coupled Double Quantum Dots

While for $B=5.01$ T the data shows the logarithmic decrease with temperature, although yielding a lower Kondo temperature (see insets in Fig. 6.17 (c) and (d)), for the overlapping Kondo regions, i.e. 4.95 T, the non-monotonic behavior with temperature is no longer present. This observation could be interpreted as an influence of the edge state chirality but the quality of the data does not allow an unequivocal conclusion in this respect.

On the data in Fig. 6.17 (b) after the background subtraction, a fit procedure with Eq. 2.43 is performed, and the Kondo temperature is obtained for the 4.92 T to 5.02 T interval. T_{K2} exhibits a similar behavior as in QD1, that is an increase-decrease in the QD1-QD2 Kondo overlapping region, from 4.92 to 4.97 T, followed by a roughly linear decrease. The shape parameter s in this case yields an increase-decrease from 4.92 to 4.97 T, related to the changes in T_{K2} , while for higher filed values it shows a linear increase.

As already discussed in Chapter 5.1.3, at high perpendicular magnetic fields Kondo effect involves transport only through energy states that belong to Landau Level 0 (LL0) [79], and due to their downward trend in energy with increasing magnetic field, the Kondo coupling is reduced. Therefore the Kondo temperature shows a roughly linear decrease at fixed gate voltage, with increasing magnetic field. On the other hand, the increase and decrease of T_{K1} , and T_{K2} , around $\sim \pm 4.95$ T, which is correlated with the presence of Kondo effect in the both quantum dots, cannot be explained by single dot physics. Therefore non-local exchange interaction has to be considered. In magnetic field the Kondo resonance is split by the Zeeman term, thus in the Kondo chessboard we measure only the zero-bias conductance, while to access the full Kondo conductance a bias is necessary (see Fig. 2.22).

It was discussed in Chapter 2.3.3 that the zero-bias temperature dependence of a split ZBA follows that of the zero magnetic field Kondo resonance at high temperatures (Fig. 2.23) [91, 92]. Hence a change in

6.4. The RKKY interaction in perpendicular magnetic field

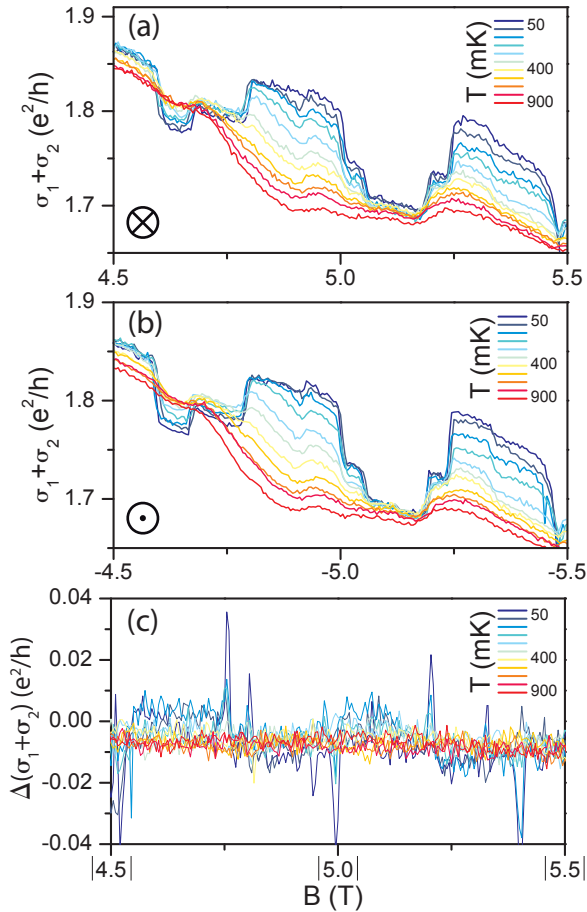


Figure 6.18.:

Temperature dependence of the total conductance for (a) positive and (b) negative magnetic field polarity, taken along the dashed lines (i.e. $V_{G6} = -20$ mV) in Fig. 6.15. (c) Difference between the total conductances at negative and positive field polarity with temperature.

6. Kondo effect in RKKY-coupled Double Quantum Dots

the ZBA splitting will appear as a change in the Kondo temperature, if the data for the full temperature range is not present. As we previously saw, the RKKY interaction main signature is a splitting of the Kondo resonance, which can be compensated by a magnetic field [24], so one can view the effect of the exchange interaction as similar to a local magnetic field. Therefore the T_{K1} and T_{K2} peaks seen in Fig. 6.16, and in Fig. 6.17 respectively, can be attributed to a change in ZBA splitting in the presence of the exchange interaction between the spins of the dots, not due to an actual increase in Kondo coupling. An alternative explanation would be that, when the impurity spins are locked by the RKKY interaction, the ground state shows a much weaker temperature dependence [93], which also results in an apparent increase of the Kondo temperature. Furthermore, even though by reversing the magnetic field direction the electron transport direction is changed, the general behavior of the Kondo temperature is very similar for both magnetic field directions, questioning whether the chirality of the edge states influences also the exchange interaction between the spins of the dots.

An important question regarding our measurements is whether the Onsager symmetry relations [94] - which require that a two-terminal measurement does not change with the magnetic field polarity - are still valid. Although here we are using a three-terminal device, the sums of the differential conductances as a function of temperature for both polarities show a very similar behavior (see Fig. 6.18 (a) and (b)). A quantitative comparison is shown in Fig. 6.18 (c), where the difference between the conductance sums at positive and negative field is presented. Although it should be a flat line, the result yields on the one hand a series of negative and positive peaks correlated with the position of the conductance jumps, due to an offset between the traces. On the other hand, there are small deviations from the expected flat line, for example in the 4.5 to 4.7 T interval, or between 5.0 T to 5.01 T.

6.4. The RKKY interaction in perpendicular magnetic field

However, these deviations are not large enough - <5% from the signal value, in the same range as the measurement noise - to be considered a break of the Onsager symmetry relations [95, 96].

6.4.2. Bias dependence

The bias dependence of the two quantum dots confirms the expected change in ZBA splitting due to the exchange interaction. In Fig. 6.19 we show the bias dependence of (a) QD1 for negative magnetic field, taken along the dashed line in Fig. 6.15 (a), and the bias dependence of (b) QD2, taken along the dashed line in Fig. 6.15 (d). The two have been chosen because in these measurements the conductance is not affected by the chirality of the edge states. As discussed earlier in this Section, the conductance through the dot "downstream" is affected in by the transmission of the dot "upstream" of the edge state. The resulted pattern as a function of magnetic field and bias would therefore increase the difficulty in identifying the effects of the exchange interaction.

In the case of QD1, in the interval -4.77 to -4.97 T, we observe a change in the ZBA splitting (marked by dashed line in Fig. 6.19 (a)), namely with increasing magnetic field the splitting decreases, together with a suppression of the conductance - visible especially at high bias. In QD2 a similar effect can be observed, although apparently with a much steeper slope (dashed line in Fig. 6.19 (b)). If we associate an effective g-factor to the change in the splitting, QD1 yields a $g_{QD1}^* \cong -30$, while in QD2 we obtain a value of $g_{QD2}^* \cong 170$. The regions where we see the rapid changes in the splitting coincide with the ones where the enhancement of the Kondo temperature is observed in Fig. 6.17 (e) and Fig. 6.18 (e).

It can also be seen in the trace cuts in Fig. 6.19 (c) and (d) that for high-bias the changes are more dramatic. In Fig. 6.19 (c) for the

6. Kondo effect in RKKY-coupled Double Quantum Dots

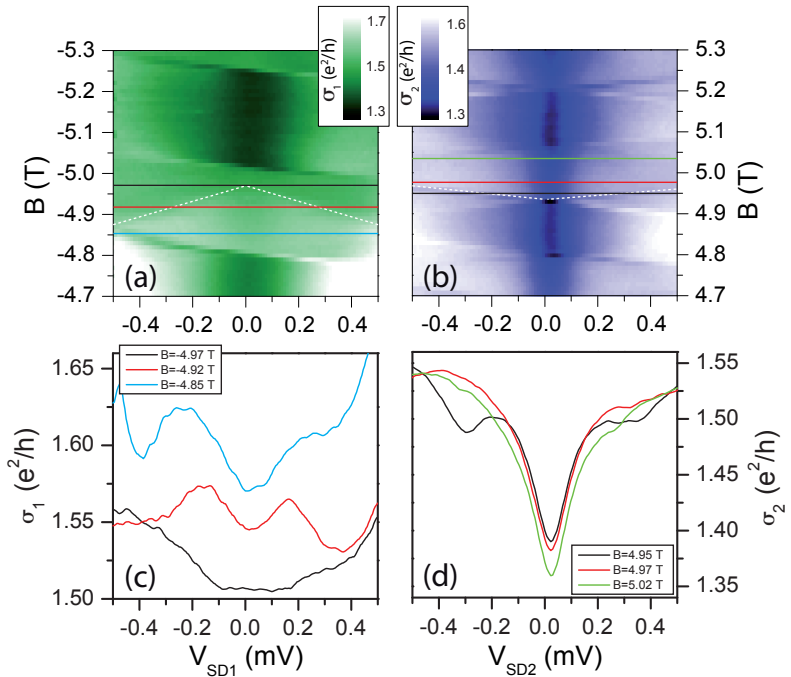


Figure 6.19.:

Bias dependence in perpendicular magnetic field for (a) QD1 and (b) QD2 for $V_{G6} = -20$ mV. White dashed lines highlight a change in the splitting of the Kondo resonance. (c)-(d) Trace cuts along the corresponding lines in (a), and (b) respectively.

-4.85 T trace two peaks at roughly ± 0.24 mV are clearly visible in the conductance through QD1. At -4.92 T the location of the two peaks is already ± 0.16 mV, while at -4.97 T are no longer visible. The trace cuts for the QD2 conductance (Fig. 6.19 (d)) show two visible peaks at roughly ± 0.2 mV for the 4.95 T trace, but in the 4.97 T and

5.02 T traces, the peaks are seen as shoulders in the conductance, and their position cannot be clearly identified. It must be mentioned that for a magnetic field value around 5 T, the Zeeman splitting expected from Eq. 2.44 is about $130 \mu\text{eV}$, a factor of 2 smaller than the measured splitting at -4.85 T for QD1 (Fig. 6.19 (c)), or 5.02 T for QD2 (Fig. 6.19 (d)), this feature being presently not understood. The more prominent features visible at higher bias could indicate that the RKKY interaction increases with the bias voltage.

6.5. Summary

In this chapter we have reviewed the basic properties of the RKKY exchange interaction and its application to quantum dots, in the frame of the 2 Impurity Kondo (2IK) model. We have shown evidence of the RKKY coupling at zero magnetic field as a function of the Kondo energy scales of the two quantum dots. We are able to tune the RKKY interaction strength by tuning the Kondo coupling in a highly asymmetric state and we find the expected $\sim 1/\ln(T_K)$ dependence of the RKKY interaction strength J_{RKKY} on the Kondo temperature.

In parallel magnetic field we probe the anti-ferromagnetic nature of the exchange interaction and extract the values of the RKKY interaction strength. A perpendicular magnetic field induces a striking chiral coupling between the quantum dots in the Kondo regime and we probe the presence of the RKKY exchange interaction by extracting the Kondo energy scale from temperature dependent measurements. The presence of the exchange interaction seems to enhance the Kondo temperature of both quantum dots, providing evidence of a Kondo to spin-glass transition. Non-linear measurements indicate that the RKKY exchange coupling increases at high bias.

6. Kondo effect in RKKY-coupled Double Quantum Dots

7

Chapter 7.

Summary and conclusions

This thesis covers the experimental realization and characterization of a two impurity Kondo system, consisting of two lateral quantum dots coupled via an open conducting reservoir. We have presented ample proof that long range interaction effects in solid state systems can play an important role in spin entanglement techniques, with possible application to quantum computing.

The samples used in this work were fabricated by a combination of optical lithography and atomic force nanolithography from GaAs/AlGaAs heterostructures, containing a shallow two dimensional electron gas. A complex oxide line pattern created with the AFM locally depletes the electron gas, thus defining at the same time the quantum dots. The quantum dot energy levels, electron number and tunnel coupling to the leads are controlled by nearby in-plane gates. With the samples placed in a dilution refrigerator, electronic transport measurements were performed in a nearly noise-free electrical setup that allows reaching electronic temperatures well under 100 mK.

7. Summary and conclusions

The quantum dots are characterized individually in a high coupling regime through Coulomb blockade measurements, combined with elastic and inelastic cotunneling spectroscopy. We investigate the inelastic cotunneling onset in a few electron quantum dot, corresponding to the first and second excited states. Non-linear measurements as a function of perpendicular magnetic field allow the direct observation of orbital effects on the excited states and the cotunneling energy gap. Several energy state crossings are observed between excited states and the ground state in a magnetic field, and we find corresponding steps in the zero bias conductance through the dot.

The zero-bias anomaly induced by Kondo effect is observed inside a Coulomb blocked area. A consistent comparison between different methods of determining the Kondo energy scale is performed. While the logarithmic temperature decay of the Kondo conductance provides evidence for what is usually considered the typical fingerprint of Kondo effect, we find that the most reliable method of obtaining the Kondo temperature is from the resonance width at low temperatures. We demonstrate that a voltage on a nearby in-plane gate allows also the tuning of the Kondo temperature, by tuning the tunnel coupling to the leads.

The electron Landé factor is extracted from the splitting of the Kondo resonance induced by an in-plane magnetic field, with a value close to the one of bulk GaAs. Because the splitting of the Kondo resonance is visible only from a magnetic field threshold value, which normally is correlated with the Kondo energy, a quantitative comparison with the values extracted from the resonance width yields good agreement. In perpendicular magnetic field we observe a flux quantum modulated Kondo chessboard up to high field values. In a novel analysis approach for the temperature dependence of the Kondo conductance in perpendicular magnetic field, we find that the Kondo temperature decreases linearly with increasing magnetic field, in good agreement with

the behavior of LL0 energy states in the Fock-Darwin spectrum.

The last chapter reviews the basic properties of the RKKY exchange interaction and its application to quantum dots. From zero field data interpreted in the frame of the two impurity Kondo (2IK) model we provide evidence of the RKKY coupling as a function of the Kondo energy scales of the two quantum dots. An interesting outcome is the ability to tune the RKKY interaction strength by tuning the Kondo coupling in a highly asymmetric state, with an expected $\sim 1/\ln(T_K)$ dependence of the RKKY interaction strength J_{RKKY} . A very relevant result proving the importance of long-range spin-spin exchange interactions.

In a state with almost symmetric Kondo couplings of the quantum dots, we find evidence of an anti-ferromagnetic RKKY interaction ground state, as well as possible influences of the confining potential of the coupling region on the RKKY interaction strength. An in-plane magnetic field induces a singlet-triplet transition, and from its energy we extract a value of 14 μV or 160 mK for the exchange interaction strength.

A perpendicular magnetic field induces a striking chiral coupling between the quantum dots in the Kondo regime and we probe the presence of the RKKY exchange interaction by temperature and bias dependent measurements. The presence of the exchange interaction seems to enhance the Kondo temperature of both quantum dots, providing evidence of a Kondo to RKKY cross-over transition. Analysis of non-linear measurement data suggests that the RKKY exchange coupling is increased at high bias.

7. Summary and conclusions



Appendix A.

**Additional data on sample
C021227B**

Interaction effects in inelastic cotunneling measurements

In the following are presented additional measurement results in sample C02122B obtained from a different cooling cycle than the one in which the results presented in Chapter 4 were obtained. In this case the electrical setup is the one shown in Fig. A.1 (a), with both dots in transport. In Fig. A.1 (b) there is non-linear measurement of QD1, as a function of the voltage applied on G1 and bias voltage V_{SD} . Two cotunneling peaks are visible inside the Coulomb diamond, located at roughly $V_{SD} \approx 0.4$ mV and $V_{SD} \approx 0.9$ mV. For negative bias, although there is a finite cotunneling current, the expected symmetric cotunneling peaks are not visible. The other gate voltage applied to the sample are: $V_{G2} = -65$ mV, $V_{G3} = 300$ mV and $V_{G4} = 60$ mV. Increasing the voltage on G3 to $V_{G3} = 400$ mV increases the electron number in QD2 by one, that is from N to $N+1$. In Fig. A.1 (c) is shown the same measurement as in (b) but for $V_{G3} = 400$ mV, i.e. $N+1$ electron in QD2. It can be seen that the cotunneling peak at $V_{SD} \approx 0.4$ mV is no longer visible. In the trace cuts in Fig. A.1 (d) taken in the middle of the Coulomb diamond, is better visible that the peak $V_{SD} \approx 0.4$ mV is missing.

Lowering the voltage in G3 and increasing the voltage in G4, on the one hand decreases the coupling of QD2 to the central region, while on the other hand increases the coupling to the second drain D2. In Fig. A.2 is shown a comparison between the initial situation discussed in the previous paragraph for $V_{G3} = 300$ mV and $V_{G3} = 400$ mV (Fig. A.2 (a)), and a situation where QD2 has a lower coupling to the central region for the same electron numbers (Fig. A.2 (b)). The voltages applied to the sample in the low coupling case are $V_{G3} = 100$ mV for N electrons in QD2, and $V_{G3} = 175$ mV for $N+1$ electrons, with $V_{G4} = 200$ mV. It can be observed that when the QD2 has a low cou-

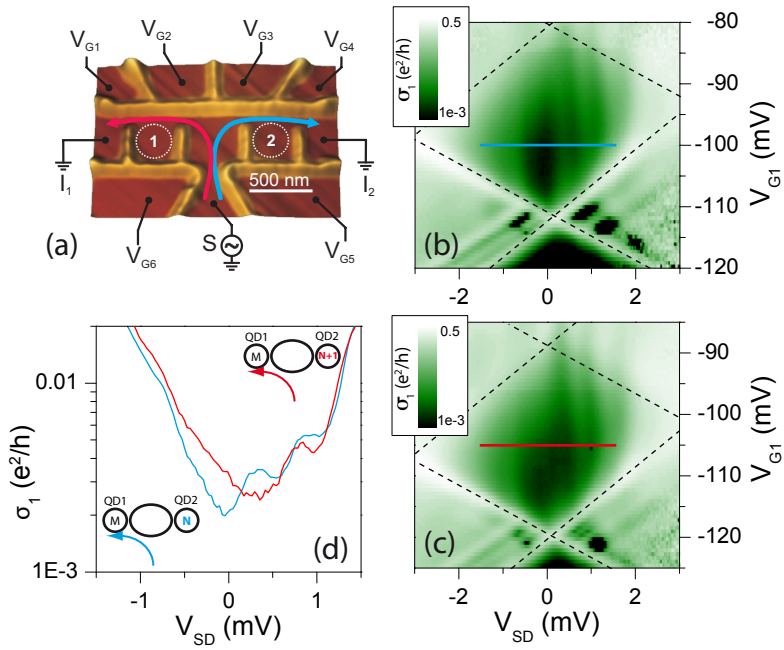


Figure A.1.:

(a) AFM picture of sample C021227B with the electrical contacts of the leads schematically represented. (b) Non-linear measurement on QD1. Two cotunneling peaks are visible inside the Coulomb diamond, and several excited states. Dashed lines mark the Coulomb diamond edges. (c) Same measurement as in (b) after increasing the electron number in QD2 by one. (d) Trace cuts taken along the corresponding lines in (b), and (c) respectively.

pling towards the central region, changing the electron number from N to N+1 in QD2 has little influence over the cotunneling peaks in QD1. Both cotunneling peaks remain visible in the non-linear transport for

A. Additional data on sample C021227B

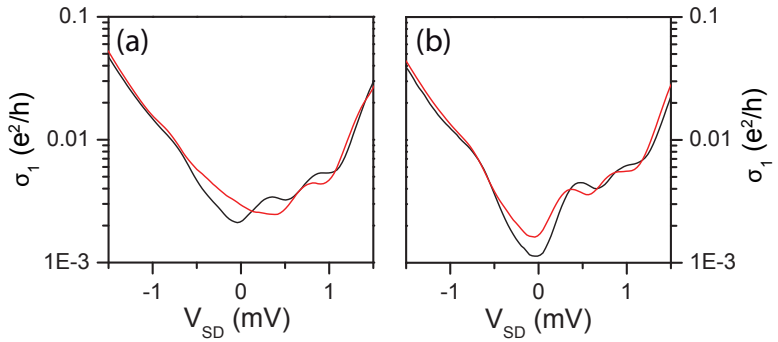


Figure A.2.:

Non-linear conductance of QD1 as a function of electron number in QD2. (a) Trace cuts for $V_{G3} = 300$ mV (black, N electrons), and $V_{G3} = 400$ mV (red, N+1 electron) respectively. (b) Trace cuts for $V_{G3} = 100$ mV (black, N electrons), and $V_{G3} = 175$ mV (red, N+1 electron) respectively.

both situations.



Appendix B.

**Additional data on sample
D080330A**

Kondo conductance background subtraction

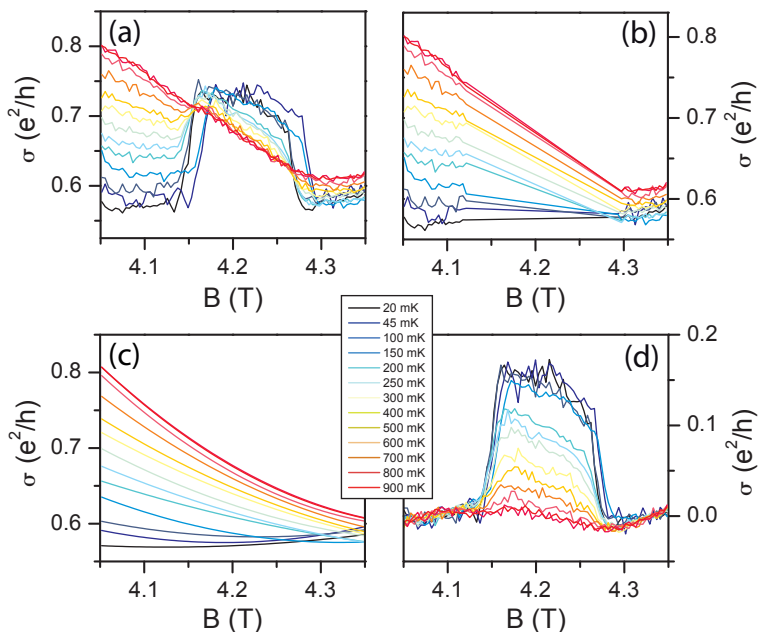


Figure B.1.:

Background subtraction for sample D080220A in the Kondo chessboard. (a) Original data showing the temperature dependence of a Kondo region in perpendicular magnetic field. (b) Original background conductance after removing the Kondo region. (c) Second order polynomial fit of the background conductance in (b). (d) Kondo conductance after subtracting the background from the original data in (a).



Appendix C.

Additional data on sample D040330A

Magnetic field conductance features

In the present Appendix we focus on the additional peaks in the conductance visible at the onset of Kondo transport through both QD1 and QD2, shown here in Fig. C.1. The traces in Fig. C.1 (a) and (b) are taken along the dashed lines in Fig. 6.15 (c), respectively (d) for positive magnetic field polarity. In Fig. C.1 (a) the sharp steps in the conductance at 4.79 T and 4.92 T mark the onset of Kondo transport in QD1 (greyed area). Exactly at the Kondo onset there are two very sharp peaks present, highlighted in Fig. C.2 (a). Corresponding to the peaks in the QD1 conductance, in transport through QD2 two very sharp dips in the conductance are visible at the same magnetic field values (see Fig. C.2 (b)). These features are not only present at the lowest temperature, but are visible up to 150 mK, showing a logarithmic decrease with temperature (Fig. C.2 (c) and (d)).

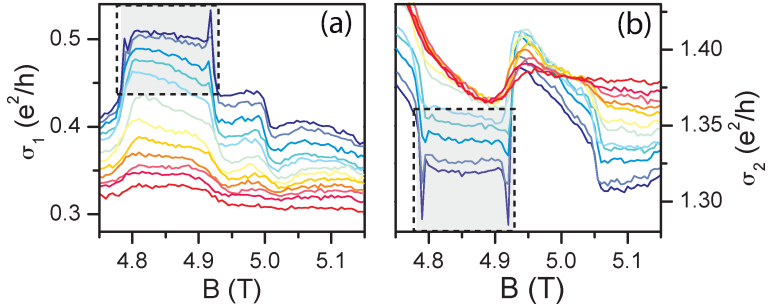


Figure C.1.:

(a) Temperature dependence of the QD1 conductance taken along the dashed line in Fig. 6.15 (c). (b) Temperature dependence of the QD2 conductance taken along the dashed line in Fig. 6.15 (d).

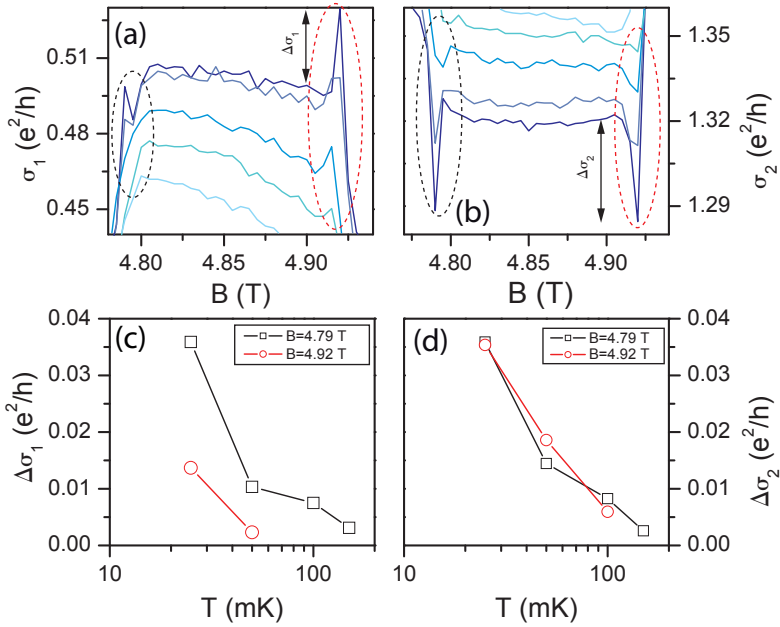


Figure C.2.:

(a) Temperature dependence of the QD1 conductance in the highlighted area in Fig. C.1 (a). (b) Temperature dependence of the QD2 conductance in the highlighted area in Fig. C.1 (a). (c)-(f) Temperature dependence of the conductance peaks in (a), and (b) respectively.

Kondo conductance background subtraction

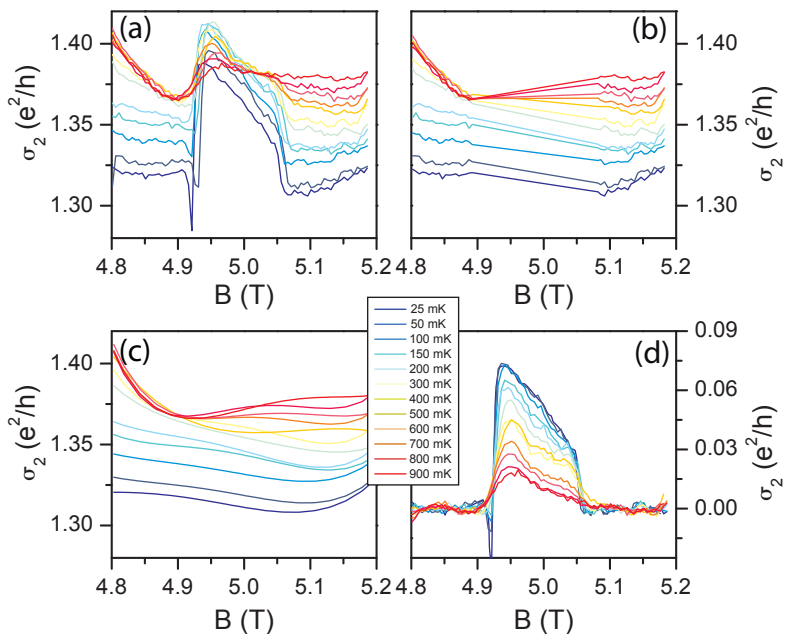


Figure C.3.:

Kondo conductance background subtraction for sample D040330A. (a) Original data showing the temperature dependence of a Kondo region in perpendicular magnetic field. (b) Original background conductance after removing the Kondo region. (c) Fifth order polynomial fit of the background conductance in (b). (d) Kondo conductance after subtracting the background from the original data in (a).



Appendix D.

Signal and grounding electrical setup

Signal and grounding electrical setup

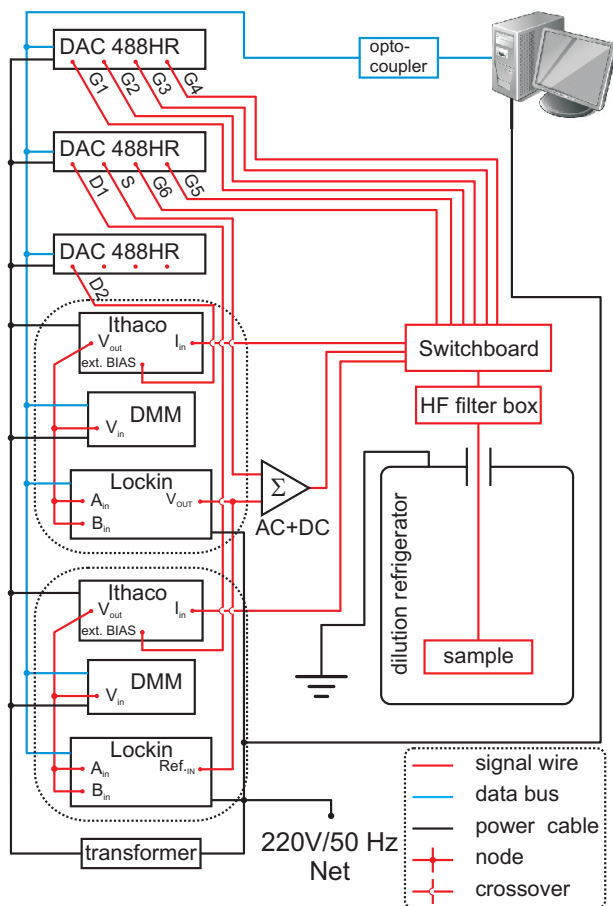


Figure D.1.:
Grounding diagram of the measurement setup

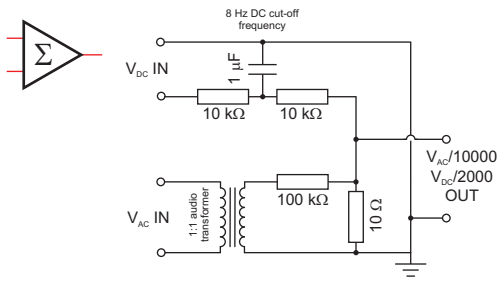


Figure D.2.:
AC-DC adder and divider

D. Signal and grounding electrical setup

Bibliography

- [1] M. A. Kastner, *The single-electron transistor*, Rev. Mod. Phys. **64**, 849 (1992). 21, 30, 38
- [2] *Mesoscopic Electron Transport*, Herausgeber: L. L. Sohn, L. P. Kouwenhoven und G. Schön (NATO Series, Kluwer, Dordrecht, 1997). 39
- [3] S. T. L.P. Kouwenhoven, D.G. Austing, *Few-electron quantum dots*, Rev. Prog. Phys. **64**, 701 (2001). 30, 38
- [4] R. Hanson, L. P. Kouwenhoven, J. R. Petta, S. Tarucha und L. M. K. Vandersypen, *Spins in few-electron quantum dots*, Rev. Mod. Phys. **79**, 1217 (2007). 21
- [5] D. Loss und D. P. DiVincenzo, *Quantum computation with quantum dots*, Phys. Rev. A **57**, 120 (1998). 21, 123
- [6] M. D. Blumenthal, B. Kaestner, L. Li, S. Giblin, T. J. B. M. Janssen, M. Pepper, D. Anderson, G. Jones und D. A. Ritchie, *Gigahertz quantized charge pumping*, Nat Phys **3**, 343 (2007). 21
- [7] Z. Yuan, B. E. Kardynal, R. M. Stevenson, A. J. Shields, C. J. Lobo, K. Cooper, N. S. Beattie, D. A. Ritchie und M. Pepper, *Electrically Driven Single-Photon Source*, Science **295**, 102 (2002). 21

Bibliography

- [8] D. Goldhaber-Gordon, H. Shtrikman, D. Mahalu, D. Abusch-Magder, U. Meirav und M. A. Kastner, *Kondo effect in a single-electron transistor*, Nature **391**, 156 (1998). 21, 55, 66
- [9] D. Goldhaber-Gordon, J. Göres, M. A. Kastner, H. Shtrikman, D. Mahalu und U. Meirav, *From the Kondo Regime to the Mixed-Valence Regime in a Single-Electron Transistor*, Phys. Rev. Lett. **81**, 5225 (1998). 64, 104, 106, 116
- [10] S. M. Cronenwett, T. H. Oosterkamp und L. P. Kouwenhoven, *A Tunable Kondo Effect in Quantum Dots*, Science **281**, 540 (1998). 21, 66
- [11] J. Kondo, *Resistance minimum in dilute magnetic alloys*, Prog. Theor. Phys. **32**, 37 (1964). 22, 56
- [12] L. I. Glazman und M. Raikh, *Resonant Kondo transparency of a barrier with quasilocal impurity states*, JETP **47**, 452 (1988). 22, 58, 61
- [13] M. A. Ruderman und C. Kittel, *Indirect Exchange Coupling of Nuclear Magnetic Moments by Conduction Electrons*, Phys. Rev. **96**, 99 (1954). 22, 120
- [14] T. Kasuya, *A Theory of Metallic Ferro- and Antiferromagnetism on Zener's Model*, Progress of Theoretical Physics **16**, 45 (1956).
- [15] K. Yosida, *Magnetic Properties of Cu-Mn Alloys*, Phys. Rev. **106**, 893 (1957). 22, 120, 122
- [16] A. C. Hewson, *The Kondo Problem to Heavy Fermions* (Cambridge University Press, 1993). 22, 57, 63, 121, 123

-
- [17] C. Jayaprakash, H. R. Krishna-murthy und J. W. Wilkins, *Two-Impurity Kondo Problem*, Phys. Rev. Lett. **47**, 737 (1981). 22, 121, 122
- [18] B. A. Jones und C. M. Varma, *Study of two magnetic impurities in a Fermi gas*, Phys. Rev. Lett. **58**, 843 (1987). 22, 121, 122
- [19] N. J. Craig, J. M. Taylor, E. A. Lester, C. M. Marcus, M. P. Hanson und A. C. Gossard, *Tunable Nonlocal Spin Control in a Coupled-Quantum Dot System*, Science **304**, 565 (2004). 22, 23, 120, 123, 133
- [20] B. A. Jones, C. M. Varma und J. W. Wilkins, *Low-Temperature Properties of the Two-Impurity Kondo Hamiltonian*, Phys. Rev. Lett. **61**, 125 (1988). 23, 121
- [21] B. A. Jones, B. G. Kotliar und A. J. Millis, *Mean-field analysis of two antiferromagnetically coupled Anderson impurities*, Phys. Rev. B **39**, 3415 (1989). 23
- [22] M. Lee, M.-S. Choi, R. López, R. Aguado, J. Martinek und R. Žitko, *Two-impurity Anderson model revisited: Competition between Kondo effect and reservoir-mediated superexchange in double quantum dots*, Phys. Rev. B **81**, 121311 (2010). 23, 123
- [23] S. Sasaki, S. Kang, K. Kitagawa, M. Yamaguchi, S. Miyashita, T. Maruyama, H. Tamura, T. Akazaki, Y. Hirayama und H. Takayanagi, *Nonlocal control of the Kondo effect in a double quantum dot-quantum wire coupled system*, Phys. Rev. B **73**, 161303 (2006). 23, 123
- [24] P. Simon, R. López und Y. Oreg, *Ruderman-Kittel-Kasuya-Yosida and Magnetic-Field Interactions in Coupled Kondo Quantum Dots*,

Bibliography

- Phys. Rev. Lett. **94**, 086602 (2005). 23, 122, 123, 124, 125, 130, 140, 141, 144, 154
- [25] M. G. Vavilov und L. I. Glazman, *Transport Spectroscopy of Kondo Quantum Dots Coupled by RKKY Interaction*, Phys. Rev. Lett. **94**, 086805 (2005). 123, 124, 141
- [26] G. B. Martins, C. A. Büsser, K. A. Al-Hassanieh, E. V. Anda, A. Moreo und E. Dagotto, *Transport Properties of Strongly Correlated Electrons in Quantum Dots Studied with a Simple Circuit Model*, Phys. Rev. Lett. **96**, 066802 (2006). 23, 123, 133
- [27] T. Ando, A. B. Fowler und F. Stern, *Electronic properties of two-dimensional systems*, Rev. Mod. Phys. **54**, 437 (1982). 26, 27
- [28] S. M. Sze, *Semiconductor Devices* (Wiley-VCH Verlag GmbH, 1985). 26, 70
- [29] S. J. Tans, M. H. Devoret, H. Dai, A. Thess, R. E. Smalley, L. J. Geerligs und C. Dekker, *Individual single-wall carbon nanotubes as quantum wires*, Nature **386**, 474 (1997). 28
- [30] B. J. van Wees, H. van Houten, C. W. J. Beenakker, J. G. Williamson, L. P. Kouwenhoven, D. van der Marel und C. T. Foxon, *Quantized conductance of point contacts in a two-dimensional electron gas*, Phys. Rev. Lett. **60**, 848 (1988). 28
- [31] M. Büttiker, *Quantized transmission of a saddle-point constriction*, Phys. Rev. B **41**, 7906 (1990). 28
- [32] H. Ibach und H. Lüth, *Solid-State Physics*, 3rd (Springer-Verlag, 2003). 30, 35
- [33] C. Kittel, *Introduction to Solid State Physics* (Wiley-VCH Verlag GmbH, 2004). 32

- [34] *The Quantum Hall Effect*, Herausgeber: R. E. Prange und S. M. Girvin (Springer-Verlag, 1990). 32
- [35] K. v. Klitzing, G. Dorda und M. Pepper, *New Method for High-Accuracy Determination of the Fine-Structure Constant Based on Quantized Hall Resistance*, Phys. Rev. Lett. **45**, 494 (1980). 32
- [36] L. Shubnikov und W. de Haas, *A New Phenomenon in the Change of Resistance in a Magnetic Field of Single Crystals of Bismuth*, Nature **126**, 500 (1930). 33
- [37] D. B. Chklovskii, B. I. Shklovskii und L. I. Glazman, *Electrostatics of edge channels*, Phys. Rev. B **46**, 4026 (1992). 34
- [38] M. Büttiker, *Absence of backscattering in the quantum Hall effect in multiprobe conductors*, Phys. Rev. B **38**, 9375 (1988). 35
- [39] F. Schwabl, *Quantenmechanik* (Springer-Verlag, 1998). 36
- [40] T. Heinzel, *Mesoscopic Electronics in Solid State Nanostructures* (Wiley-VCH Verlag GmbH, 2008). 41, 45, 71, 80, 84, 85
- [41] V. Fock, Z. Phys. **47**, 446 (1928). 43
- [42] C. Darwin, Math. Proc. Cambridge Philos. Soc. **27**, 86 (1930). 43
- [43] A. Fuhrer, A. Dorn, S. Lüscher, T. Heinzel, K. Ensslin, W. Wegscheider und M. Bichler, *Invited Review Electronic properties of nanostructures defined in Ga[Al]As heterostructures by local oxidation*, Superlattices and Microstructures **31**, 19 (2002). 45, 78
- [44] P. L. McEuen, E. B. Foxman, J. Kinaret, U. Meirav, M. A. Kastner, N. S. Wingreen und S. J. Wind, *Self-consistent addition spectrum of a Coulomb island in the quantum Hall regime*, Phys. Rev. B **45**, 11419 (1992). 46

Bibliography

- [45] S. Datta, *Electronic Transport in Mesoscopic Systems* (Cambridge University Press, 1995). 48, 51
- [46] M. D. Franck J.P., Manchester F.D., Proc. Roy. Soc. **A263**, 494 (1961). 55
- [47] P. W. Anderson, *Localized Magnetic States in Metals*, Phys. Rev. **124**, 41 (1961). 55
- [48] P. W. Anderson und G. Yuval, *Exact Results in the Kondo Problem: Equivalence to a Classical One-Dimensional Coulomb Gas*, Phys. Rev. Lett. **23**, 89 (1969). 57
- [49] K. G. Wilson, *The renormalization group: Critical phenomena and the Kondo problem*, Rev. Mod. Phys. **47**, 773 (1975). 57, 121
- [50] G. L. Kouwenhoven, L.P., *Revival of the Kondo Effect*, Physics World 33 (2001). 58, 61
- [51] A. M. Chang und J. C. Chen, *The Kondo effect in coupled-quantum dots*, Rep. Prog. Phys. **72**, 096501 (2009). 60, 121, 123
- [52] F. D. M. Haldane, *Scaling Theory of the Asymmetric Anderson Model*, Phys. Rev. Lett. **40**, 416 (1978). 61
- [53] G. Bergmann, *Quantitative calculation of the spatial extension of the Kondo cloud*, Phys. Rev. B **77**, 104401 (2008). 61
- [54] W. G. van der Wiel, S. D. Franceschi, T. Fujisawa, J. M. Elzerman, S. Tarucha und L. P. Kouwenhoven, *The Kondo Effect in the Unitary Limit*, Science **289**, 2105 (2000). 62
- [55] Y. Meir, N. S. Wingreen und P. A. Lee, *Low-temperature transport through a quantum dot: The Anderson model out of equilibrium*, Phys. Rev. Lett. **70**, 2601 (1993). 63

- [56] T. A. Costi, A. C. Hewson und Z. V., *Transport coefficients of the Anderson model via the numerical renormalization group*, J. Phys. Condens. Matter **6**, 2519 (1994). 64
- [57] R. Zitko, private communication (unpublished). 65, 66
- [58] C. W. J. Beenakker, *Theory of Coulomb-blockade oscillations in the conductance of a quantum dot*, Phys. Rev. B **44**, 1646 (1991). 64, 105
- [59] R. Zitko und T. Pruschke, *Energy resolution and discretization artifacts in the numerical renormalization group*, Phys. Rev. B **79**, 085106 (2009). 64
- [60] W. Wegscheider, in *Optics of Semiconductor Quantum Wires and Dots*, Herausgeber: G. Bryant (Gordon and Breach Science Publishing, 1998). 70
- [61] G. Binnig, C. F. Quate und C. Gerber, *Atomic Force Microscope*, Phys. Rev. Lett. **56**, 930 (1986). 77
- [62] G. Binnig und H. Rohrer, Helv. Phys. Acta **55**, 726 (1982). 77
- [63] H. J. Mamin, P. H. Guethner und D. Rugar, *Atomic emission from a gold scanning-tunneling-microscope tip*, Phys. Rev. Lett. **65**, 2418 (1990). 78
- [64] H. W. Schumacher, U. F. Keyser, U. Zeitler, R. J. Haug und K. Eberl, *Nanomachining of mesoscopic electronic devices using an atomic force microscope*, Applied Physics Letters **75**, 1107 (1999). 78
- [65] J. Regul, U. F. Keyser, M. Paesler, F. Hohls, U. Zeitler, R. J. Haug, A. Malavé, E. Oesterschulze, D. Reuter und A. D. Wieck,

Bibliography

- Fabrication of quantum point contacts by engraving GaAs/AlGaAs heterostructures with a diamond tip*, Applied Physics Letters **81**, 2023 (2002). 78
- [66] M. Ishii und K. Matsumoto, *Control of Current in 2DEG Channel by Oxide Wire Formed Using AFM*, Japanese Journal of Applied Physics **34**, 1329 (1995). 78, 80, 126
- [67] K. Matsumoto, S. Takahashi, M. Ishii, M. Hoshi, A. Kurokawa, S. Ichimura und A. Ando, *Application of STM Nanometer-Size Oxidation Process to Planar-Type MIM Diode*, Japanese Journal of Applied Physics **34**, 1387 (1995). 80
- [68] R. Held, T. Heinzel, P. Studerus, K. Ensslin und M. Holland, *Semiconductor quantum point contact fabricated by lithography with an atomic force microscope*, Applied Physics Letters **71**, 2689 (1997).
- [69] R. Held, T. Vancura, T. Heinzel, K. Ensslin, M. Holland und W. Wegscheider, *In-plane gates and nanostructures fabricated by direct oxidation of semiconductor heterostructures with an atomic force microscope*, Applied Physics Letters **73**, 262 (1998). 81, 126
- [70] U. F. Keyser, H. W. Schumacher, U. Zeitler, R. J. Haug und K. Eberl, *Fabrication of a single-electron transistor by current-controlled local oxidation of a two-dimensional electron system*, Applied Physics Letters **76**, 457 (2000). 78, 81, 126
- [71] S. K. Ghandhi, *VLSI Fabrication Principles* (J. Wiley and Sons Inc, 1994). 79
- [72] S. De Franceschi, S. Sasaki, J. M. Elzerman, W. G. van der Wiel, S. Tarucha und L. P. Kouwenhoven, *Electron Cotunneling in a*

- Semiconductor Quantum Dot*, Phys. Rev. Lett. **86**, 878 (2001). 91, 92, 96
- [73] R. Schleser, T. Ihn, E. Ruh, K. Ensslin, M. Tews, D. Pfannkuche, D. C. Driscoll und A. C. Gossard, *Cotunneling-Mediated Transport through Excited States in the Coulomb-Blockade Regime*, Phys. Rev. Lett. **94**, 206805 (2005). 91
- [74] T. Fujisawa, T. H. Oosterkamp, W. G. van der Wiel, B. W. Broer, R. Aguado, S. Tarucha und L. P. Kouwenhoven, *Spontaneous Emission Spectrum in Double Quantum Dot Devices*, Science **282**, 932 (1998). 93
- [75] D. M. Zumbühl, C. M. Marcus, M. P. Hanson und A. C. Gossard, *Cotunneling Spectroscopy in Few-Electron Quantum Dots*, Phys. Rev. Lett. **93**, 256801 (2004). 95, 96, 110
- [76] S. Tarucha, D. G. Austing, T. Honda, R. J. van der Hage und L. P. Kouwenhoven, *Shell Filling and Spin Effects in a Few Electron Quantum Dot*, Phys. Rev. Lett. **77**, 3613 (1996). 98
- [77] C. Fuehner, *Magneto-Transport Investigations on Multi-Electron Quantum Dots: Coulomb Blockade, Kondo Effect, and Fano Regime*, Dissertation, Universitaet Hannover, 2002. 103, 113, 133
- [78] D. E. Logan und N. L. Dickens, *Field-dependent dynamics of the Anderson impurity model*, Journal of Physics: Condensed Matter **13**, 9713 (2001). 109
- [79] C. Fuehner, U. F. Keyser, R. J. Haug, D. Reuter und A. D. Wieck, *Flux-quantum-modulated Kondo conductance in a multi-electron quantum dot*, Phys. Rev. B **66**, 161305 (2002). 112, 125, 145, 152

Bibliography

- [80] M. Keller, U. Wilhelm, J. Schmid, J. Weis, K. v. Klitzing und K. Eberl, *Quantum dot in high magnetic fields: Correlated tunneling of electrons probes the spin configuration at the edge of the dot*, Phys. Rev. B **64**, 033302 (2001).
- [81] M. Stopa, W. G. van der Wiel, S. D. Franceschi, S. Tarucha und L. P. Kouwenhoven, *Magnetically Induced Chessboard Pattern in the Conductance of a Kondo Quantum Dot*, Phys. Rev. Lett. **91**, 046601 (2003).
- [82] D. Kupidura, M. C. Rogge, M. Reinwald, W. Wegscheider und R. J. Haug, *Probing a Kondo-Correlated Quantum Dot with Spin Spectroscopy*, Phys. Rev. Lett. **96**, 046802 (2006). 116, 125
- [83] M. C. Rogge, C. Fühner und R. J. Haug, *Multiple Transitions of the Spin Configuration in Quantum Dots*, Phys. Rev. Lett. **97**, 176801 (2006). 112, 116, 145
- [84] B. A. Jones und C. M. Varma, *Critical point in the solution of the two magnetic impurity problem*, Phys. Rev. B **40**, 324 (1989). 121
- [85] M. T. Béal-Monod, *Ruderman-Kittel-Kasuya-Yosida indirect interaction in two dimensions*, Phys. Rev. B **36**, 8835 (1987). 122
- [86] H. B. Heersche, Z. de Groot, J. A. Folk, L. P. Kouwenhoven, H. S. J. van der Zant, A. A. Houck, J. Labaziewicz und I. L. Chuang, *Kondo Effect in the Presence of Magnetic Impurities*, Phys. Rev. Lett. **96**, 017205 (2006). 123
- [87] R. Lopez, R. Aguado und G. Platero, *Nonequilibrium Transport through Double Quantum Dots: Kondo Effect versus Antiferromagnetic Coupling*, Phys. Rev. Lett. **89**, 136802 (2002). 123, 124, 130, 141

- [88] R. Aguado und D. C. Langreth, *Out-of-Equilibrium Kondo Effect in Double Quantum Dots*, Phys. Rev. Lett. **85**, 1946 (2000). 123, 124, 130, 141
- [89] P. Gegenwart, Q. Si und F. Steglich, *Quantum criticality in heavy-fermion metals*, Nat Phys **4**, 186 (2008). 131
- [90] R. Zitko, *Fano-Kondo effect in side-coupled double quantum dots at finite temperatures and the importance of two-stage Kondo screening*, Phys. Rev. B **81**, 115316 (2010). 133
- [91] R. Zitko und J. Martinek, private communication (unpublished). 139, 152
- [92] T. A. Costi, *Kondo Effect in a Magnetic Field and the Magnetoresistivity of Kondo Alloys*, Phys. Rev. Lett. **85**, 1504 (2000). 152
- [93] R. Lopez, private communication (unpublished). 154
- [94] L. Onsager, *Reciprocal Relations in Irreversible Processes. I.*, Phys. Rev. **37**, 405 (1931). 154
- [95] D. Sánchez und M. Büttiker, *Magnetic-Field Asymmetry of Non-linear Mesoscopic Transport*, Phys. Rev. Lett. **93**, 106802 (2004). 155
- [96] D. Sánchez und K. Kang, *Validity and Breakdown of Onsager Symmetry in Mesoscopic Conductors Interacting with Environments*, Phys. Rev. Lett. **100**, 036806 (2008). 155

Acknowledgements

There are many people to whom I would like to thank, who supported and helped me, or that in one way or another contributed to this work.

First and foremost I wish to thank my supervisor Prof. Dr. Rolf J. Haug for giving me the opportunity to work in his group, for his careful guidance, encouragement and supervision that made possible the existence of this thesis. I thank also Prof. Dr. Gertrud Zwicknagl for taking an interest in this work and accepting the role of the second referee.

Being an experimental work, this thesis is the result of a collaborative effort on many levels in a group, and over the years I have learned a great deal from those I have worked with. I would like to thank PD Dr. Frank Hohls for patiently putting up with all my questions, and for his invaluable advice throughout my thesis. I enjoyed a lot working with Dr. Christian Fricke and Niels Ubbelohde, and special thanks go to them for many interesting and valuable discussions about the measurement setup or various physics problems. This work would probably turned out a bit different if not for the theoretical calculations and support from the "Palma" group: Rok Zitko, Jan Martinek and Rosa Lopez-Gonzalo. I am very much indebted to Prof. Dr. Werner Wegscheider, Dr. Dieter Schuh and Martin Reinwald for supplying the heterostructure materials that were used for our measurements.

To Yvonne Griep and Finja Hansen, Klara Wernecke, Ronny Hüther, Harmut Lehmann and Manfred Marquardt I would like to show my appreciation for their help in various organizational and technical matters throughout the preparation of this thesis.

I am also very grateful to Dr. Niels Maire, Alexander Heine and Henrik Schmidt for the care with which they reviewed this manuscript and for many useful suggestions on how to improve it; to my present office mates Dr. Niels Maire, Dr. Maximillian Rogge and Alexan-

der Heine, or former - Dr. Annelene Dethlefsen, Adriana Hadzibrahi-movic, Tammo Böntgen and Theo Ridder - I thank for creating a won-derful working atmosphere and always being fun to be around.

I'd like to thank also the students I worked with and supervised: Bogdan Popescu, Cay Kalmbach, Johannes Bayer and Thomas Jost. A direct contribution to this thesis came from Bogdan who pro-duced sample D040330A, and Cay for the measurements on sample D08022A.

Life as a graduate student would probably have been a lot harder if not for my friends Liviu and Ema, Sebastian, Lucian, Cristina, Nor-mann, Rabea and Jörg.

I wish to express my gratitude to my parents, Stela and Du-mitru Tutuc for their constant encouragement and support, and to my brother Emanuel Tutuc, who has always been a source of inspiration for me.

Finally, this thesis is dedicated to my ever loving wife Mihaela, with-out whom none of this would have been possible.

Lebenslauf

Name: Daniel Tutuc
Geburtsdatum: 20. April 1981
Geburtsort: Slatina

1996–2000 Colegiul National "Radu Greceanu"
Slatina, Rumänien

Juni 2000 Abschluss: Abitur

2000–2005 Studium der Physik an der Universität Bukarest
Diplomarbeit: „Quantum dots produced by
nanolithography with an Atomic Force
Microscope“

seit September 2005 Vorbereitung der Dissertation
am Institut für Festkörperphysik der
Gottfried Wilhelm Leibniz Universität Hannover
bei Prof. Dr. Rolf J. Haug

Publications

- *Tunable non-local coupling between Kondo impurities*, D. Tutuc, B. Popescu, D. Schuh, W. Wegscheider, and R. J. Haug, Phys. Rev. B **83**, 241308(R), (2011)
- *Mesoporous GaAs double layers for layer transfer processes*, E. Garalaga Rojas, B. Terheiden, H. Plagwitz, C. Hempe, D. Tutuc, R. J. Haug, and R. Brendel Phys. Status Solidi A **206**, 2872-2875, (2009)